Spring 1-30-2019

APPLICATION OF MACHINE LEARNING TO CHF MODELLING

Mingfu He Mr
nuclear enginering

Mingfu He
Candidate

Nuclear Engineering
Department

This thesis is approved, and it is acceptable in quality and form for publication:

Approved by the Thesis Committee:

Dr. Youho Lee, Chairperson

Dr. Sang Lee

Dr. Amir Ali

APPLICATION OF MACHINE LEARNING TO CHF MODELLING

BY

MINGFU HE

B.S., Nuclear Engineering, Chengdu University of Technology, Chengdu, 2016

THESIS

Submitted in Partial Fulfillment of the
Requirements for the Degree of

Master of Science

Nuclear Engineering

The University of New Mexico
Albuquerque, New Mexico

May 2019

ACKNOWLEDGMENTS

At this time, I feel like grabbing this opportunity to express my sincere gratitude for the help and advice that I have received in the performance and the completion of this thesis. First and foremost, I gratefully thank my advisor, Prof. Youho Lee, for giving me the opportunity to explore the world of boiling heat transfer of thermal hydraulics systems. I would also like to express my sincere appreciation to my advisor for his patience, encouragement and trust. It has always been a privilege to learn from Prof. Youho Lee's vast experience in the field of heat transfer.

Special thanks are extended to my colleagues who shared the happiness and sorrows in studies and researches with me these years, including Dr.Seung Gu Kim, Dr. Maolong Liu, Mr. Soon Lee, Mr Dongjune Chang, and Mr. David Wetzel.

Last but not the least, I would like to thank my adorable daughter, Yangyang for your lovely smiles. Without your unwavering understanding; this project would not have been completed.

Application of Machine Learning to CHF Modelling

By

Mingfu He

B.S., Nuclear Engineering, Chengdu University of Technology, 2016

M.S., Nuclear Engineering, University of Technology, 2019

ABSTRACT

Accurate prediction of CHF is still a challenging issue in the study of boiling heat transfer. Many factors contribute to the occurrence of CHF and the various trigger mechanisms are proposed to unravel physical phenomena behind CHF. However, those mechanisms cannot cover the multiple primary factors simultaneously and even some of them still remain controversially unresolved. In light of the complexity and difficulty of CHF modelling, hereby an ensemble-learning based framework is proposed to model and predict CHF based on the databank of CHF. Some prior trials have been done for three primary aspects of dominant factors, that is, surface morphology, geometrical dimension and operation condition. These three primary constituents are respectively analyzed though three different sub-models of the ensemble framework in Chapter 3, 4 and 5.

In Chapter Three, relevant experiments about micro-pillar enhanced CHF are reviewed and the corresponding databank of microstructure enhanced CHF is compiled based on those CHF experiments from published papers. Although the impacts of micro-pillars on CHF are still not clear, through qualitative analyses, the parametrical trends of CHF with respect to geometrical parameters of pillar array can be roughly foreseen. Meanwhile, this study also evaluates performance of prediction accuracy among four current physical models of microstructure-enhanced CHF. Comparative results show that two capillary wicking

models have higher prediction accuracy. Particularly, a special terminology, zero-infinity convergence, is introduced to discuss the parametrical trends of CHF and qualitatively assess veracity of two capillary wicking models. Given the drawbacks of current physical models, the DBN is proposed to more accurately predict CHF and study parametric trends of CHF based on the microstructure enhanced CHF databank. Different from the training process of other regression modelling problems, constrained CHF points, which are artificially derived from the training data datasets, are required to be coupled with the raw training datasets for achieving the zero-infinity convergence of the DBN based CHF model, exhibiting accurate parametric trends of CHF and improving the prediction accuracy. This new training technique provides a new reliable solution to the similar constrained machine learning problems. Numerical results demonstrate that DBN can achieve the best performance of CHF prediction in terms of prediction accuracy. Through studying parametrical trends of CHF reveals that micro pillar arrays with the same parameters on heat transfer substrates with different dimensional sizes presents different CHF enhancement profiles. The presented methodology provides new insights for CHF modelling in pool boiling enhanced by other surface modification techniques, including porous layer coating, nanoparticle deposition, textured roughen, and nanowire fabrication. The effects of dimensions and materials of boiling surfaces on CHF are correlated and studied through the GRNN modelling in Chapter Four. Instead of inputting all parameters that indicate the thermal properties of materials into the trained model, the aggregated parameters from the primitive parameters of thermal properties, thermal activity and thermal diffusivity, are utilized as the input parameters of the trained model. This technique not only could capture the effects of thermal properties of materials on CHF effectively but

also helps reduce the computational loads. The trained model shows the similar parametric trends of CHF to that of the traditional empirical correlation with respect to the thermal activity. If the thermal activity of heat transfer substrate is beyond a certain value, the corresponding effect of thermal activity will be absent, which somehow implies that the thickness of heat transfer substrate will not impact CHF after the asymptomatic thickness is reached. On the other hand, thermal diffusivity still affects CHF occurrence even if the effect of thermal activity is negligible. When coming to the effect of dimension size on CHF, it was found that when the side length of square heat transfer substrate is 5 times greater than the capillary length of working fluid, the CHF will be independent on the side length. Otherwise, CHF will be affected by the side length, and the influence of side length on CHF reaches ultimate if the side length of square boiling surface is exactly equal to the Raleigh-Plateau instability wavelength. This instability wavelength is only dependent on the thermal properties of working fluids, meaning that the optimal side length for CHF optimization is only related to the thermal properties of working fluid, namely, the surface tension, and the liquid and vapor densities of working fluid.

In Chapter Five of this study, ν-support vector machine is adopted to explore and study experimental strategies for the data-driven approaches of CHF look-up table construction, on the basis of sparingly-distributed experimental CHF data points. In the virtue of the CHF look-up table of Groeneveld et al (2007), those CHF data was used as the reference data of this research. In this data collection, CHF data of the subcooled flow boiling ($Xe < 0$) is chosen to concentrate on the PWR steady-state condition because the in the normal operation of PWR, the system is under the subcooled flow boiling. The numerical results have demonstrated that ν-SVM trained by well sparsely-distributed training data in the

parameter region of interest (pressure and mass flux) can yield a fairly acceptable degree of CHF prediction accuracy. Procuring training data points that can imply the parametric behaviors of CHF with respect to pressure and mass flux for support vector machine is the essential key of machine learning to achieving a high level of CHF prediction accuracy. For capturing the pressure-variant CHF behavior, training data that are in the proximity of the CHF inflection point significantly contribute to the improvement of prediction accuracy. Hence, training data preparation physics-informed with knowledge of CHF inflection points definitely augments the prediction accuracy of CHF. How the parametrical trends of CHF with respect to pressure and mass flux are close to the linear trends determines the level of prediction accuracy when lacking of a good spread of training data points. Besides, it is found that CHF extrapolation to a higher pressure with many data points collected at different low pressures can be effectively achieved by SVM if a few CHF data points are available under the high pressure, especially for PWR pressure of 15.5 MPa. This announces a possibility of strategic integration experiments between high pressure and low pressure, reducing experimental costs associated with the high pressure testing in terms of efforts and money. The proposed methodologies provides engineers and experimentalists with useful strategies to construct the look-up table tabulation of advanced cladding materials of ATFs.

It is found out that there are multiple sub-problems that could be divided for CHF prediction and each sub-problem has its individual suitable machine learning model. Those prior work done by this study proves that the data-driven CHF modelling by sub-models can provide accurate CHF prediction under various scenarios and correct parametrical trends with respect to separate variables.

Last but not least, another contribution of this thesis to the field of boiling heat transfer is that two databanks of experimental CHF data are compiled for the CHF enhancement by microstructures. The compiled databanks provide useful information and guidelines to the future design of surface structures that will possibly be applied to heat exchanger and nuclear fuel rod.

NOMENCLATURES

CHF critical heat flux

BHT boiling heat transfer

ONB onset of nucleate boiling

HTC heat transfer coefficient

LWR light water reactor

PWR pressurized water reactor

BWR boiling water reactor

ANN artificial neural network

GRNN general regression neural network

DBN deep belief network

SVM support vector machine

DNBR departure from nucleate boiling ratio

RBMs Restricted Boltzmann Machines

BPNN back propagation neural network

RBFNN radial basis function neural network

TABLE OF CONTENTS

1 INTRODUCTION

1.1 Boiling Heat Transfer

Boiling heat transfer is a ubiquitous application from the daily lives to industrial fields. Besides, all modes of boiling heat transfer, no matter from pool boiling to flow boiling, seem to physically present complex and dynamical behaviors that are very hard to elaborate based on the very first principle. However, meticulous and methodical investigations have been conducted to explicate the difficult and ambiguous parts of boiling heat transfer and to understand physical phenomena observed in experiments. “What does the engineering field know about boiling heat transfer?” is essentially posed in a review presented by Lienhard and Dhir(J. H. Lienhard & Dhir, 1973a). Yes still, up to now, this is a formidable question to the field of heat transfer. Most of the primary and experiential knowledge in boiling heat transfer we enjoy nowadays is a comprehensive collection of the pioneered theoretical and experimental works conducted over the last serval decades. In the recent developments and advancements, the field focuses of boiling heat transfer have already stepped into the subfield of micro and nano-scale heat transport (Cahill et al., 2003). Boiling heat transfer is an essential and complicated part of thermal nuclear reactor systems. A complete understanding through all aspects of boiling heat transfer is important to management of thermal systems at various scales.

An inherent primary explanation of the boiling heat transfer needs basic principles analyses from the nano-scale to the macro-scale. Many efforts have been put into the understanding of boiling. For the perspective of macro-scale, continuum mechanics based boiling models are completely able to provide an empirical understanding of most of macro-scale

phenomena. However, it is very doubtful that the results from macro scale models could be applied to micro and nano scales to which it is doubtful to apply the continuum mechanics. Fang et al.(Jaeseon Lee & Mudawar, 2009) demonstrated that at micro and nano scale, thermal transport would be a different story. Understanding boiling heat transfer from molecular level is a better resolution to the complicated phenomena. Mukherjee et al (Mukherjee, Datta, & Kumar Das, 2018) the molecular vibration of working fluids increases, further repelling the neighbors molecules of less vibration to run away and finally forming vapor bubbles.

Although numerous theoretical and experimental observations have been performed, boiling heat transfer is a kind of the category of physical phenomena that are incompletely understood or still remains controversial since the incipience of boiling researches. This is a result out of two common difficulties that are prohibiting the development of physical analytical model. The first hindrance is scarce of a complete understanding to interaction between the solid-liquid interfaces. Surface structure and nucleation site heterogeneity are two essential characteristics of the heat transfer surface that has impact on the wetting dynamical behaviors of resupplying liquids at the solid-liquid interface. The wetting dynamical kinetics of liquids plays a vital role of the entire boiling stage from boiling incipience to film boiling at the interface between solid and the liquid. But, it is an understatement to boiling heat transfer that barely stating that wetting is a governing factor. Besides, the surface features of wettability can vary a lot from hyper hydrophobic to hydrophobic to hydrophilic to super hydrophilic. Both of wetting extremes can exhibit remarkably different behaviors in four different stages of boiling heat transfer. Both

nucleation site heterogeneity and surface structure further make it more complicate to physically depict the wetting dynamics behaviors of resupplying liquids. Surface structures, depending on their sizes and patterns, can significantly change wettability and two-phase flow dynamics. Besides altering the wettability and site heterogeneity of boiling surface modify the distribution pattern of local temperature fields if the local adjacent regions vary significantly in terms of thermal mechanics properties. The aforementioned discussion is a bare glance of the total complexities involved in accurate descriptions of the liquid-solid interaction when boiling heat transfer occurs. Secondly, it is the lack of understanding the molecular dynamics of phase change that hinders the precise explanation of boiling heat transfer based on the very first principle. It can be determined that the temperature at which boiling is about to occur, the temperature of the heat transfer surface that is necessary to boiling inception can be much greater than the boiling point.

1.2 Boiling Curve Enhancement

The boiling curve, as seen in Fig 1-1, is a typical standard graphical method to characterize boiling stages. Boiling processing is categorized into four different regimes that are typified by the characteristics of the bubble formation: natural convection, nucleate boiling, transition boiling and film boiling. If the boiling system works with a saturated liquid, and the temperature of heated surface is slightly greater than the saturation temperature of working fluids, then no bubble forms on the surface and heat is transferred with method of the natural convection of superheated liquid, which is driven via buoyancy forces. This is the regime of natural convection from the origin point to Point A.

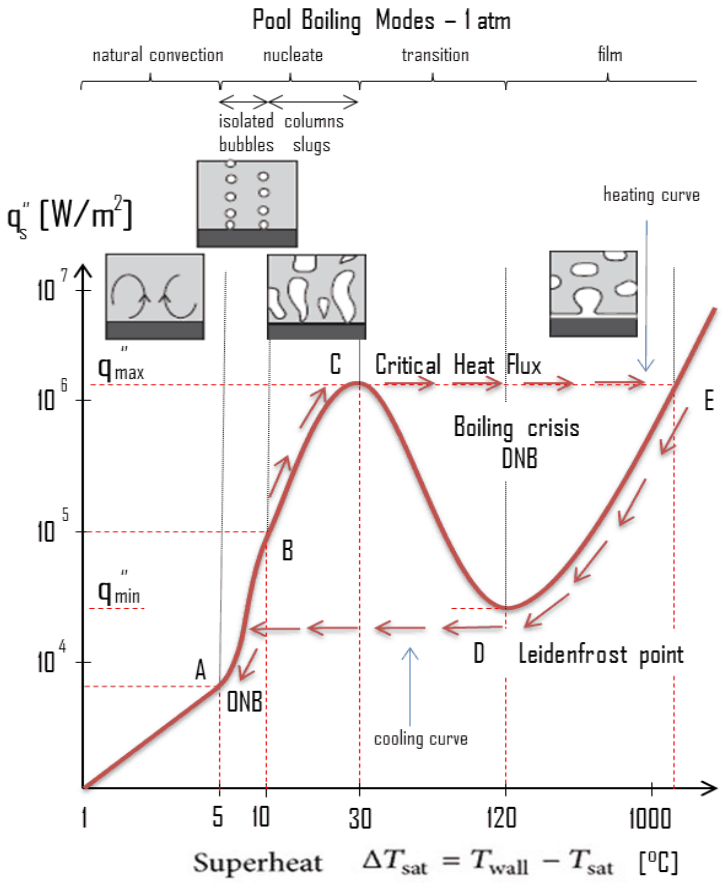

Fig.1-1 Typical Boiling Curve (Leong, Ho, & Wong, 2017)

Nucleate boiling is initiated when the temperature of the heated surface is greater than the saturation temperature and the heat surface begins to generate bubbles, which detach from the heat transfer surface and float upward to the free surface of working fluid, marking the onset of nucleate boiling (ONB) by point A. Nucleate boiling is often characterized by a sharp increase in slope of the boiling curve, that is, a sudden incremental of HTC. As bubble becomes more regularly and densely growing, bubbles start to coalesce vertically and horizontally and merge into slugs or columns, which reduces heat transfer coefficient due to the formation of vapor layer upon the surface. As the heat flux is further applied, the maximum heat flux is reached for nucleate boiling, point C that is typically referred to as the critical heat flux (CHF).

Care and caution must be taken if the heat flux of thermal system is close to the CHF of that system. The surface temperature suddenly "jumps" to temperatures in the order of thousands of degrees (point E) where film boiling occurs for maintaining equilibrium, if the heat flux is further increased due to some uncertain factors. This is known as the burnout crisis since the temperature overshoot could allow the surface temperature to reach the melting point of surface material.

Up to now, the extensive researches have been conducted to enhance the boiling curves, including CHF enhancement, the improvement of heat transfer coefficient (HTC), and the reduction to ONB, that is, to shift the boiling curve leftwards and upwards. In Fig.1-2, the multiple boiling curves present enhanced heat transfer features, such as ONB, CHF and HTC. Therefore, it is essential for the design of thermal systems to maximize the efficient heat removal region and determine the resulting CHF and HTC enhancements. To enhance CHF and HTC ultimately, surface modification technologies have been widely applied in various experimental conditions. The CHF and HTC enhancement mechanisms by using deposition of nano or micro particles on heating surfaces were attributed to surface area enlargement (You, Kim, & Kim, 2003), surface wettability enhancement (H. Kim & Kim, 2009), formation of porous structure (S. D. Park & Bang, 2014), and wavelength modulation (H. Seo, Chu, Kwon, & Bang, 2015). Hydrophilic surfaces achieved by nanoparticle deposition can delay CHF via rewetting processes but this did not improve the HTC significantly (H. Seo et al., 2015). The surface characteristics and properties affecting CHF and HTC can be controlled by applying traditional mechanical methods.

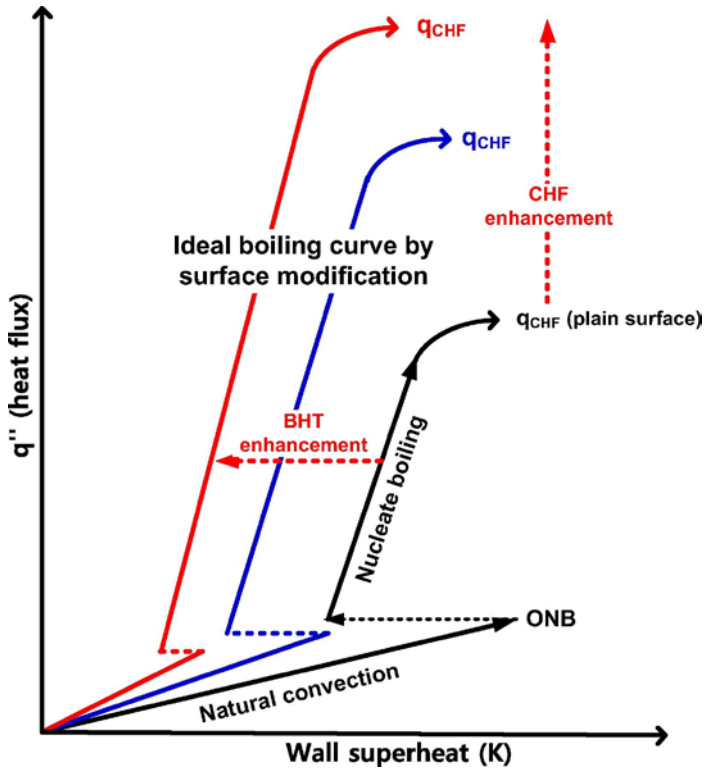

Fig.1-2 Schematic of Ideal Enhanced Boiling Curves(H. Seo, Lim, Shin, & Bang, 2018)

1.3 Critical Heat Flux

During boiling process, boiling heat transfer is governed by the nucleation, growth, and departure of bubbles from a surface, characterizing much tremendous heat being removed by the latent heat of phase change. CHF will occur if the vapor generation cannot be adequately balanced by the liquid rewetting to the local hot spots of surface. When CHF occurs the local hot spots will develop to dry-out spots, where vapor blankets isolate the solid surface from the liquid contact, further leading to an overshoot of surface temperature and incurs catastrophic consequences, including failures of boiling surface or the surface meltdown. Hence, the thermal systems are supposed to be operated at a heat flux whose value is fairly much below CHF of that system. Because of the addressing importance of

CHF to the design and operation of thermal systems, numerical researches about CHF modelling have been conducted over the last 50 years and different physical mechanisms are proposed to explain the occurrence of CHF in the past decades.

It is widely accepted that CHF is determined by various factors such as, operation conditions (Misale, Guglielmini, & Priarone, 2009), thermal properties of working fluids and boiling surface materials (Arik & Bar-cohen, 2006), surface morphologies (Ferjančič & Golobič, 2002), geometrical configurations (Kandlikar, 2002), and the surface oxidation of boiling surfaces (Kang, Kim, Lee, Kim, & Park, 2018). The graph of factor tree demonstrates relationships between CHF and various components as shown in Fig.1-3. As shown in Fig.1-3, CHF occurrence is dominated by multiple various factors. It is impossible to give the analytical CHF model based on physical basis. Because multiple mechanisms are coupled and even some of them still remain controversial. Besides it is rather tough to account for the effects of multiple factors on CHF in single individual models.

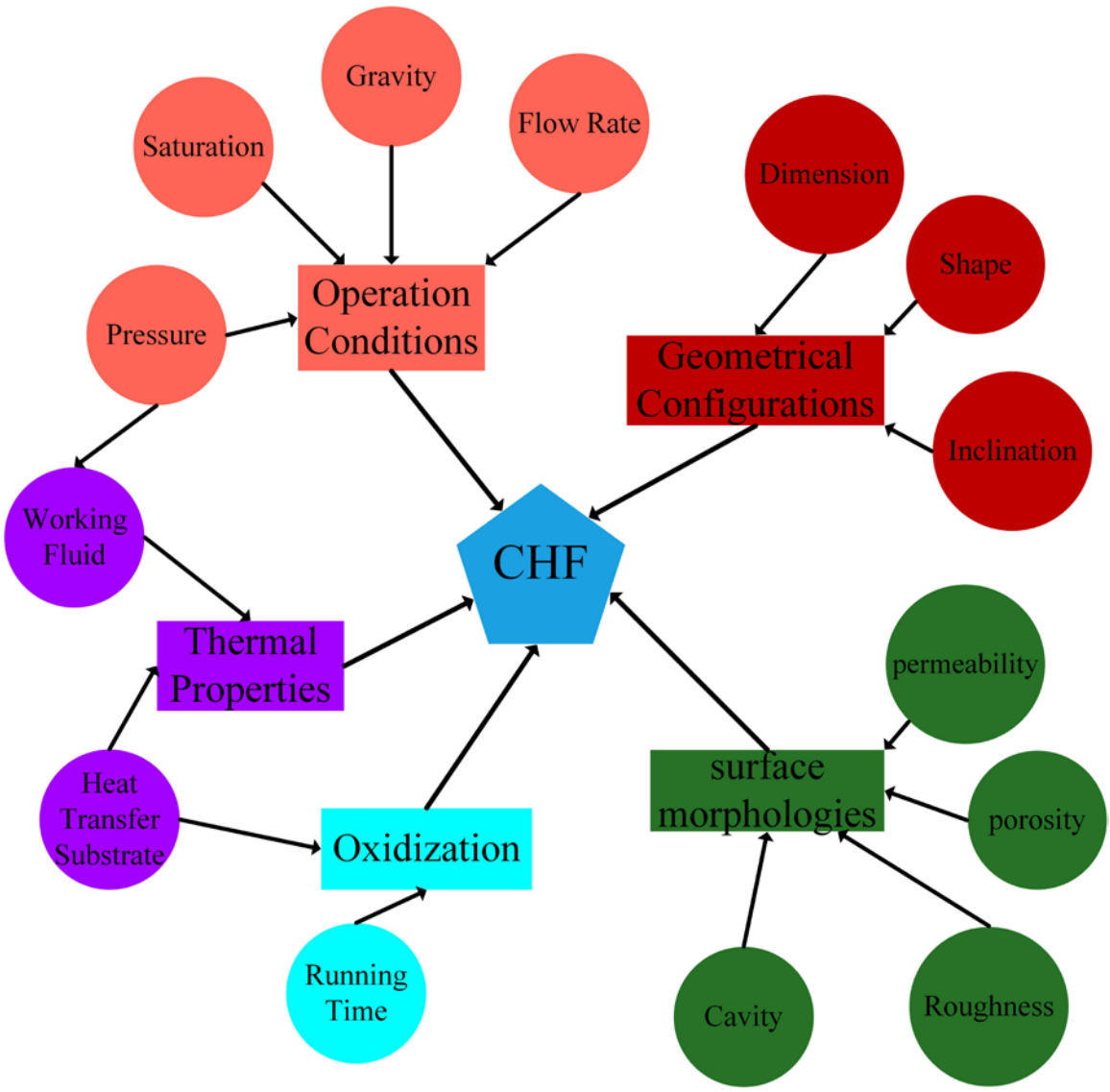

Fig.1-3 the graph of factor tree: five primary constituents affecting CHF

Machine learning is a data-driven statistical method that only replies on the training datasets, unlike physical models, the assumptions don't need the physics basis but the assumptions should be held true for the requirement of training datasets, for example, the training sets are supposed to be unbiased in terms of feature distributions, meaning that the size of training data for each feature understanding should be uniformly distributed in the total amount of training dataset. A typical example is like this, if a behavior descriptor framework of semantic role labelling and multi-label object classifying is trained by only

a tiny amount of pictures in which men cook in the kitchen and a tremendous amount of pictures that show women prepare food in the kitchen, this trained framework will misidentify a man in a kitchen from a given picture as a women because of the gender bias distribution in the training datasets (Zhao, Wang, Yatskar, Ordonez, & Chang, 2017). However, practically speaking, each modelling problem has its own predictive model based on individual machine learning framework. For example, multiple-layer forward feed neural network gives best modelling for CHF enhanced by nanofluids (Esfe, Rejvani, Karimpour, & Abbasian Arani, 2017) and HTC could be modelled by adaptive neuro fuzzy inference system for nanofluids pool boiling (Salehi, Zeinali-Heris, Esfandyari, & Koolivand, 2013). While for the CHF modelling with regard to nuclear fuel rods of light water reactor, the support vector machine seems best modelling framework (Jiejin Cai, 2012a, 2012b). In order to adapt to the applicability of various models to different CHF triggering mechanisms discussed above, the ensemble learning framework is adopted to predict CHF under different circumstances. An ensemble-based learning system is obtained by combing diverse models (henceforth regression), which yields better predictive performance than could be obtained from any of constituent learning frameworks alone (Krawczyk, Minku, Gama, Stefanowski, & Woźniak, 2017). In the CHF study of Lee (M. Lee, 2000), a set of seven correction factors is proposed to extend the applicability of the CHF lookup table to flow between rod bundles of square array in light water reactors including the hydraulic diameter factor, the bundle factor, the heated length factor and et al. These correction factors are multiplied together to correlate the induced effects on CHF. As a matter of fact, the correction approach proposed by Lee (M. Lee, 2000) is a kind of ensemble method based on physical and empirical corrections. A

pioneered trial of ensemble learning in nuclear engineering was that Baralidi et al, (Baraldi, Razavi-Far, & Zio, 2011) proposed an approach of ensemble learning for incrementally learning transients of different operational BWR conditions based on bagging and majority voting strategies under the framework of several supervised fuzzy C-means classifier. Ayodeji and Liu (Ayodeji & Liu, 2018) adopted the ensemble approach of multi-class support vector machines separately trained by simulated transient accidents of PWR to identify the most likely accidental causes. In light of the modelling complexity and difficulty of CHF prediction, this study proposes a framework of ensemble learning to predict CHF under different scenarios and improve the adaptability of the proposed CHF prediction model. The schematic illustration about the proposed framework is shown in Fig. 1-4, noting that *K* is a CHF correction factor based on learning-schemes, defined as the ratio of experimental CHF to the CHF predicted by Zuber's model.

1.4 Objectives of this Study and Thesis Structure

Many efforts have been put into investigating the effects of thermal properties of working fluids, operating conditions and surface modification on CHF. This study is a prior work to the data-driven CHF prediction based on the ensemble learning framework. However, the effects of surface materials and dimensional sizes on CHF are not extensively explored. Based on various collected CHF experimental datasets, how surface materials and dimensional sizes have influence on CHF are analyzed by the data-driven machine learning frameworks, which partially belongs to the regression model of (D_2, K_2). Besides, pin fin array, one of primary techniques in boiling heat transfer, are studied for their parametrical trends of CHF with respect to geometrical parameters through data-driven machine

learning frameworks. This micropillar CHF enhancement could be modelled by the regression model of (D_3, K_3). The CHF Lookup table is strategically reconstructed by the machine learning model falls on the sub-framework of (D_1, K_1).

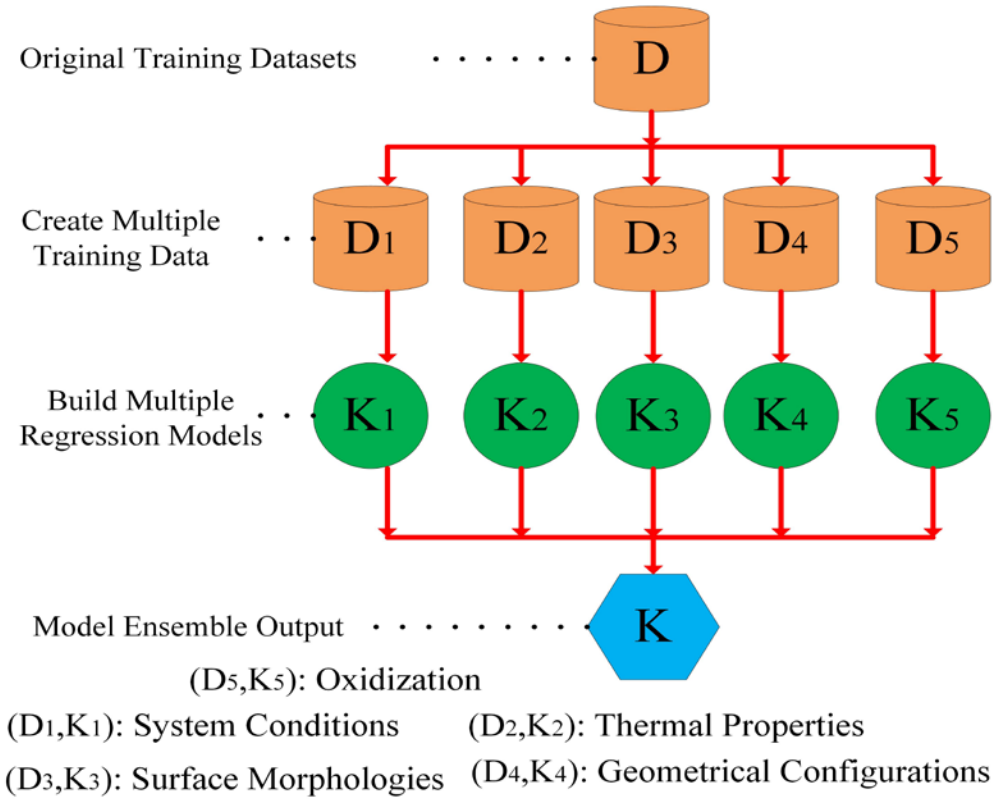

Fig.1-4 the schematic graph of the ensemble learning based framework for CHF prediction

The thesis contents are scheduled as follows: Chapter 2 gives a comprehensive review about which factors are dominant in CHF triggering mechanisms, elaborates what CHF enhancement techniques are focused now and analyzes the enhancement mechanisms behind those useful techniques; in Chapter 3, the deep belief network based model is proposed to regress the relation between CHF and pin fin array parameters and the enhancement mechanisms are explored in a more detailed manner; In Chapter 4, the effects of dimensions and materials of boiling surfaces are studied and analyzed by GRNN modelling based on experimental results; Chapter 5 discusses how support vector machine

can assist thermal hydraulics experimentalists to design CHF experiments with less experimental efforts for pressurized water reactor; the concluding summaries and remarks are made in Chapter 6.

1.5 Summaries of Chapter 1

Chapter 1 addresses the importance of boiling heat transfer, elaborates the enhancement details of boiling curves, describes the occurrence of CHF, and reviews the primary influential aspects of CHF dominant mechanisms. In light of complicated triggering mechanisms behind CHF occurrence, the framework of ensemble learning was proposed to predict CHF regardless of pool or flow boiling no matter what enhancement techniques are present on boiling surfaces. However, in this study, a prior work was done for studying and analyzing how the operation conditions of system, the dimensional sizes and materials of boiling surfaces and the surface structures affect CHF in the sub-regression models of the proposed ensemble approach.

2 EFFECTS OF DIFFERENT FACTORS ON CHF

2.1 Dominant Factors

The prediction of CHF over a heated surface is one of the hottest study aspects of pool boiling heat transfer. When the heat transfer surface is covered by a vapor layer, CHF occurs and represents the upper limit of efficient boiling. For a plain heated surface, multiple factors that affect the CHF have been identified including thermal mechanical properties of working liquids and heat transfer substrate, interfacial properties and system conditions.

2.1.1 Thermal physical properties of working liquids

Boiling curves for different fluids are very different because of their own thermal properties including the latent heat of vaporization, the liquid and vapor densities, and the surface tension. The boiling heat transfer that is an effective method for dissipating heat with high thermal power, involves the phase change of liquid and utilizes the latent heat of vaporization. In that regard, the liquid with higher latent heat of vaporization can promote the higher heat absorption during the phase change, thus indicating the higher CHF. Fluidic bulk accessibility to the local hot spot is controlled by the surface tension of the working fluid, which measures the elastic tendency of the fluid acquiring the least surface area as much as possible. However, the buoyancy force induced by bubble formation is in conflict with the surface tension force of the liquid. That means the higher surface tension of the liquid can mitigate the formation of vapor film on the surface, therefore resulting in higher CHF. The higher liquid density of the working fluid needs more heat before vaporization and delays the occurrence of CHF. On the other hand, vapor and liquid densities of fluids act together on the formation of vapor layer because of the phase change.

By increasing or decreasing the pressure of boiling system, the thermal physical properties of the working liquids are subjected to change with pressures, thus resulting in the shift of the boiling curves and various CHF points.

Drastic changes of the pressure can significantly influence the removal capacity of the heat transfer. Pressure increasing raises the saturated temperature and reduces the latent heat of vaporization, and reinforces the density difference between liquid and vapor states. However, the increased pressure also results in smaller bubble size due to the compressibility of the vapor. As a result of the smaller bubble size, there is a higher density of nucleating bubbles on the surface as well as a higher departure frequency(Mukherjee et al., 2018). In light of the competing mechanisms induced by pressure variation, there exists an optimal inflection point of pressure where CHF peaks. Motivated by Kutateladze's prior CHF work, Zuber made use of hydrodynamic instability theory and developed an analytical CHF model for saturated pool boiling on an horizontally-placed infinite flat surface, only accounting for thermal physical properties of the working fluids as follows

$$q''_{CHF} = 0.131 h_{fg} \sqrt[4]{\sigma g \rho_g^2 (\rho_l - \rho_g)} \tag{2-1}$$

where σ is the surface tension, ρ_l and ρ_g are the liquid and vapor density, h_{fg} is latent heat of vaporization and g is the gravitational acceleration constant, respectively.

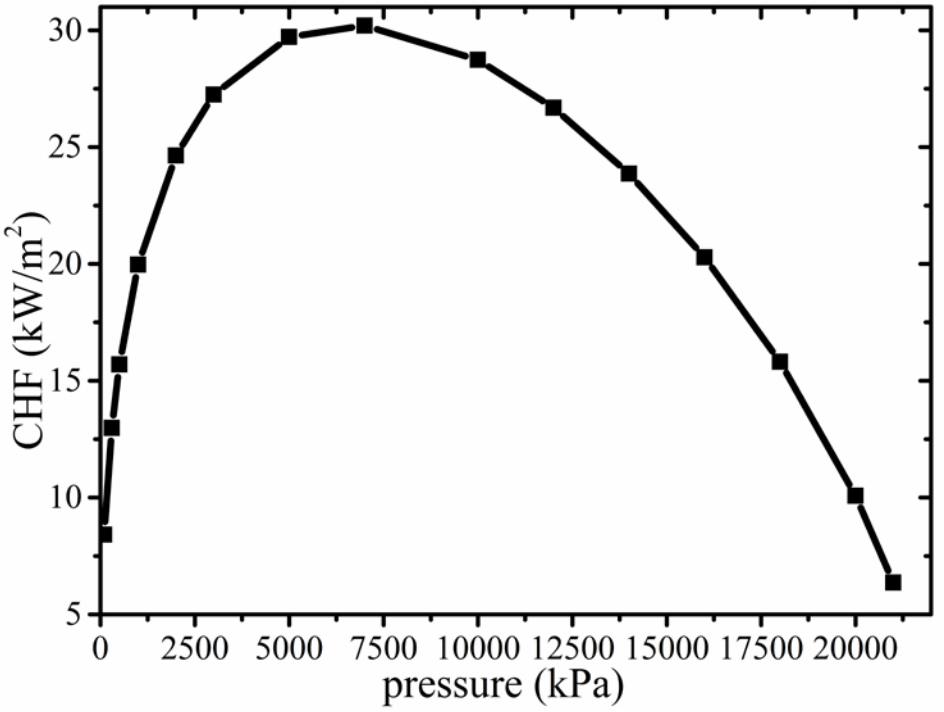

Fig. 2-1 Zuber's CHF Profile with Respect to Pressure

2.1.2 Subcooling and Surface Inclination

An increase in subcooling is believed to provide the beneficial effect on heat transfer rates during the rewetting process because the fluid bulk temperature is less than the saturation temperature. Previous experimental investigations have demonstrated that subcooling increasing decreases the departure bubble size, forces departing bubbles to rapidly collapse and finally liquefies again. Also increasing the subcooling of the bulk liquid promotes the natural convection. The departure bubbles are less likely to develop to local dry spots. CHF delay with respect to subcooling increases have been observed experimentally and this delay occurrence is due to the reduced rewetting liquid flow resistance to the local dry spots. Bubbles that immediately detach from the heat surface begin to collapse and condense into liquid states because of the subcooled liquid. This in turn allows more fluid to reach the surface. The CHF correlation between subcooled and saturated states is well established and presented as follows:

$$q''_{CHF,sub} = q''_{CHF,sat}(1 + \mathrm{C}(\frac{\rho_g}{\rho_l})^n \Delta T_{sub}) \qquad (2\text{-}2)$$

where C and n are fitting factors determined by properties of working fluid and ΔT_{sub} is the subcooled temperature. Due to the various configuration requirements, the plate heat transfer substrates cannot always be placed upward-facing horizontally. For example, the nuclear fuel rods are placed vertically in the reactor cores. How the surface orientation has impacts on CHF are experimentally investigated and empirically correlated by empirical relations but theoretical analyses associated with orientation effects are limited. Based on Howard and Mudawar's experimental investigations (Howard & Mudawar, 1999), three categories of surface orientations were suggested to be divided: upward-facing (0-60°), near-vertical (60-165°), and downward-facing (165-180°). Each category is linked to a unique CHF trigger mechanism. For the upward-facing region, the buoyancy forces remove the bubbles vertically off the heater surface. The near-vertical region is characterized by a wave-like liquid–vapor contact interface, along which bubbles sweep. In the downward-facing region, bubbles repeatedly stratify on the heater surface, thus which allows vapor layers to be more easily formed, greatly decreasing CHF. At least ten empirical formula are proposed to correlate the relation between surface orientation angles and CHF on horizontally-placed surfaces(Howard & Mudawar, 1999; Liang & Mudawar, 2018a; Mei, Shao, Gong, Zhu, & Gu, 2018a). Besides, the effects of surface inclination on HTC are different from that of CHF (Sasaki & Ashiwake, 2002).

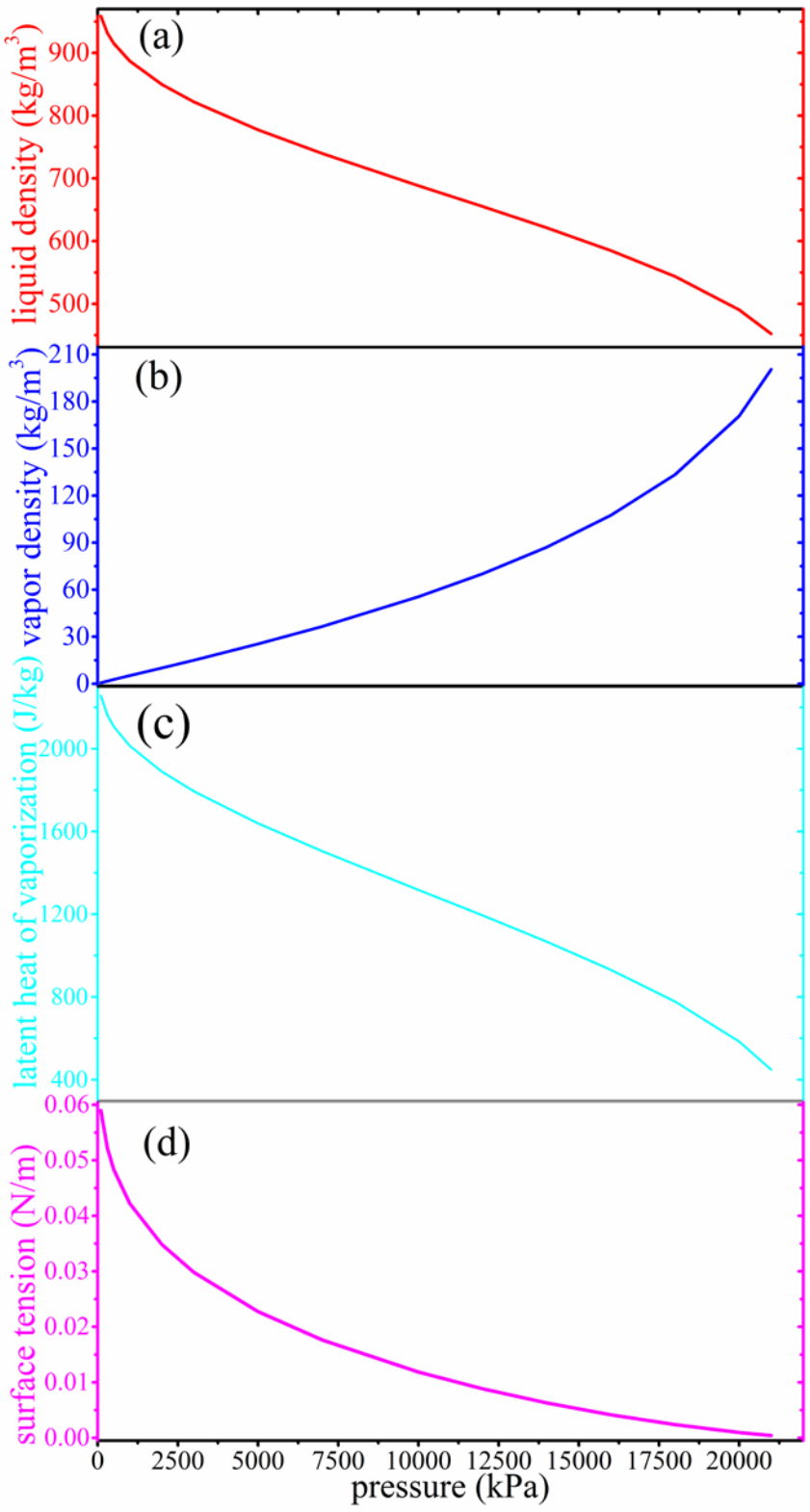

Fig.2-2 changes of water thermal properties over increasing pressure: (a) liquid density, (b) vapor density, (c) latent heat of vaporization and (d) surface tension

When coming to intermediate levels of heat fluxes, the inclination was experimentally observed to have no obvious effects on HTC. In the high heat flux region, close to CHF, the increasing of the inclination angle had negative impacts on HTC because of the accumulation influence of previously-formed vapors on later-formed vapors. As for those correlations that account for the effect of surface inclination angle, Liang and Mudawar summarized those correlations in terms of working fluids, inclination ranges and system pressures (Liang & Mudawar, 2018a). In their findings, numerical experimental results demonstrated that the best surface inclination correlation was proposed by Chang and You (Chang & You, 1996).

2.1.3 The Effects of Oxidation

There is mounting evidence that CHF depends strongly on the morphology and composition of the boiling surface. In particular, CHF can be markedly enhanced on surfaces that are very hydrophilic and capable of significant capillary wicking. This is in contrast with the classical CHF model based on the Kelvin-Helmholtz hydrodynamic instability, which completely ignores surface effects. When working fluids become oxygen-free active at high temperature, such as water, the metal heated surfaces are likely pick up oxygen-atoms and become oxidized. Accordingly, the CHF on oxidized surfaces are different from that of fresh surfaces. Although in many CHF experiments, the effects of oxidation layer on CHF have been observed, the further analyses about mechanisms are still not clear. Due to continuous heating and cooling of the chip during and after pool boiling test, the morphology of the test surface underwent various changes. It was observed that the contact angle and wickability of the surface changed in the experiments performed by Rishi, Gupta and Kandlikar (Rishi, Gupta, & Kandlikar, 2018). The effects of oxidization on

CHF present different stories due to different surface materials. In pool boiling CHF experiments of stainless steel and reactor pressure vessel prototype material (Juno Lee & Chang, 2012; Mei et al., 2018a). The oxidation effect on the CHF could be contributed by two distinct mechanisms. On the one hand, the formation of metallic oxide layer deteriorates the CHF because it has low thermal effusivity and enhances the heat resistance; on the other hand, the porous structure of metallic oxide layer helps augment the surface wettability and increase the nucleation density, which enhance the CHF(Mei et al., 2018a). Unlike ironic surface materials, the oxidization layers on copper surfaces degrade the overall thermal diffusivity of heat transfer substrates, further decreasing CHF(I. Golobič & Ferjančič, 2000).

2.1.4 Materials and Dimensional Sizes of Heat Transfer Substrate

While the role of the liquid properties, surface morphology and operating conditions on CHF in pool boiling is well investigated, the effects of the properties of the heater material are not well understood including thermal conductivity, mass density and specific heat. Previous studies indicate that the heater thickness plays an important role on the CHF phenomenon. However, beyond a certain thickness, called the asymptotic thickness, the local temperature fluctuations on the heater surface caused by the periodic bubble ebullition cycle are evened out and the CHF is not influenced by further increasing the thickness. In previous studies, the thermal activity is defined by the product of heater thickness and the square root of thermal effusivity to analyze the effects of thermal properties of heat surface on CHF.

Bemath (Bernath, 1960) firstly investigated how thermal properties and thickness of the heated surface had impacts on the CHF by noticing that thicker heaters produced higher CHF than thinner structures. Later on, his research on vertically oriented cylindrical heaters in water was extended to both solid and hollow cylinders. Experimental results revealed that the solid cylinders had about 43% higher CHF than hollow structures. A study employing zirconium ribbon heaters immersed in toluene was performed by Cole and Shulman (Cole & Shulman, 1966) . Experimental results were similar to previously published studies, with 42% higher CHF for the thickest heater. These early studies kept the attention of many researchers during the following years. Then, it was proposed that the product of thickness and thermal conductivity was a good correlation indicator of the effect of the heater.

Tachibana (Tachibana, Akiyama, & Kawamura, 1967) performed a series of experiments with a variety of materials and thicknesses in water. A theory on the transient effect of the heater was proposed based on vapor shrouding of the surface, preventing resupplying liquid from wetting the surface. This effect could be correlated with the product of the volumetric heat capacity and the heater thickness. An experimental investigation was conducted under saturated pool boiling of water at the atmospheric pressure on thin, horizontally oriented, cylindrical walls of different metals and thicknesses (Magrini & Nannei, 1975). The heated walls, ranging in thickness from 5 to 250 pm, were obtained by plating copper, silver, zinc, nickel and tin on non-metallic rods. They observed that the smaller the thermal conductivity of the metal layer, the higher the influence of the thickness. Guglielmini and Nanei (Guglielmini & Nannei, 1976) performed an experimental study with different cylindrical heaters formed with an electroplating technique. Lower CHF values on thin

heaters were observed. The heater thermal parameter depended on a constant value, C. The thickness required to achieve 90% of the CHF thermal activity of the metal was given by $\delta_{90\%} = C(\rho c_p k)^{-1.63}$. CHF was reported to be increasing asymptotically until the thickness of 350 pm. Based on a comprehensive review on the heater property effects on CHF, Saylor (Saylor, 1989) proposed the following parameter, $S = \delta\sqrt{\rho c_p k}$. Golobič and Bergles (Iztok Golobič & Bergles, 1997) performed an extensive study on the thermal property effect and they agreed that *S* is the best correlating parameter. The experimental studies showed that the thick copper blocks created higher CHF. But the Zuber relationship was found to under predict CHF by as much as 50 percent. An experimental study was carried out by Bar-Cohen and McNeil (Bar-Cohen & McNeil, 1992) with sputtered platinum and silicon heaters in dielectric liquids. They found silicon heaters had CHF about 80% higher than thin film heaters. The total effect of the heater on CHF was found to be correlated as $S/(S + 0.8)$. This relationship gives the 90 percent of CHF when S is equal to 8 while the asymptotic value is approached around S>25. However, there were no experimental results cited to confirm the asymptotic approach for S>25. Later on, a comprehensive literature review was done by Watwe and Bar-Cohen (Watwe, Bar-Cohen, & McNeil, 1996) to better understand the combined effects of the pressure, subcooling, and heater properties on the CHF. It was complemented by solving the energy equation numerically for both transient and steady state cases. They improved their previous correlation that under-predicted CHF for very thin heat surface by modifying the constant from 0.8 to 0.1.

2.2 CHF Enhancement Techniques

2.2.1 Nanofluids Applications

By altering the thermal properties of the fluid, the performance of boiling could be greatly enhanced. In recent years, it has been extensively observed that the by adding micro/nano scale thermally conductive particles into the boiling fluid can largely enhance CHF (M. S. Kamel, Lezsovits, Hussein, Mahian, & Wongwises, 2018). These particles suspended in the base fluids could be metallic (Cu, Au, and Ag), metal oxides (Fe_3O_4, Al_2O_3, and TiO_2), silicon compounds (SiO_2, SiC and SiN) and carbon materials (diamond, nanotubes and graphite particles) (Barber, J.; Brutin, D.; Tadrist, 2011). Until so far, there have been considerable significant researches about the CHF enhancements of nucleate boiling by application of nanofluids for pool boiling systems. Under convective flow conditions, research on CHF enhancements by nanofluids have been experimentally performed. It is also noteworthy that most of the experimental data given in the literatures are to study enhancement effects of nanoparticles on CHF. The effects of nanofluids on HTC still remain controversial and ambiguous since some experimental results have demonstrated that that nanofluids provide an enhancement (Abdollahi & Reza Salimpour, 2016) on the HTC, others a deterioration (Bang & Chang, 2005) and some others no change at all (Vassallo, Kumar, & D'Amico, 2004). A remarkable benefit of application of nanofluids to boiling heat transfer systems is the freedom to change their properties based on the demands of thermal systems. That is, it is very easy and plausible to adjust the thermal conductivity and surface wettability by varying the nanoparticle concentration, choosing materials of nanoparticles and modifying the average diameter of nanoparticles. But it is also important to address that adding nanoparticles to base fluid also changes the dynamic

viscosity, fluid density and even the specific heat capacity; thus having unpredictable effects on CHF and HTC (M. Kamel & Lezsovits, 2017). Nanofluids experiments show that the smaller nanoparticles can delay the occurrence of CHF a lot under the same materials and concentrations because it is less likely to let particles agglomerate together (Kumar, Urkude, Sonawane, & Sonawane, 2018). Also, there exists an optimal concentration of nanofluid achieving the ultimate CHF, and the optimal concentration is determined by the nanofluid type and average diameter of nanoparticles (Rostamian & Etesami, 2018).

2.2.2 Nanowire and Nanotube Fabrication

Nanowires array coated surface was experimentally justified by Chen et al to drastically promote boiling heat transfer performance in terms of CHF and HTC (R. Chen et al., 2009). There are four widely-recognized contributors behind the enhancements of HTC and CHF by nanowire array; first, a surface coated with nanowires could be thought superhydrophilic because nanowire array coated surface may have efficient wickingability, and the small pores between nanowires provide a very large capillary force (J. Yuan et al., 2008); second, nanowire arrays contain much more cavities and pores compared to any other processed surface by microfabrication or micromachining, which effectively mounts up the magnitudes of nucleation site density and surface roughness (R. Chen et al., 2009); finally, due to the thermal fin effect, the effective heat transfer area of nanowires may be dramatically higher than that of microstructured surfaces such as those with micro silicon pin fin array (Im, Joshi, Dietz, & Lee, 2010). Chen et al (R. Chen et al., 2009) fabricated nanowire arrays of silicon and copper on plain silicon surfaces and found that Cu nanowire

array coated surface could allow CHF of saturated water pool boiling to reach beyond 2000 kW/m^2. In CHF experiments by nanowire arrays (Shi, Wang, & Chen, 2015; Yao, Lu, & Kandlikar, 2011), the surface with the tallest nanowire yields the highest CHF among others. It is observed that during the stage of nucleation boiling, more bubbles were generated at the nanowire surface than the plain surface at a given heat flux and the density and size of surface cavity increase as the nanowire height increases (Yao et al., 2011). However, Kim et al (B. S. Kim, Shin, et al., 2014) pointed out that the coated surfaces with higher ratio of height to diameter of nanowire that result in larger and more cavity-like structures would further improve boiling heat transfer performance accompanying advanced ONB and extended CHF with higher HTC.

Nanotubes of carbon and silicon with ultrahigh thermal conductivity have been suggested for boiling heat transfer enhancement including CHF and HTC. Meanwhile fully coating the heat transfer substrate with nanotubes was greatly effective at reducing the incipience superheat and advancing ONB (Ujereh, Fisher, & Mudawar, 2007). In the paper (Ahn et al., 2006), the effects of nanotube height were investigated for boiling performance in nucleate and film boiling regimes, and also the experiments demonstrated the nanotube coated surfaces can ultimately yield 57% higher heat flux at Leidenfrost point. Besides, Ahn et al (Ahn et al., 2006) proposed another four mechanisms behind boiling performance augmentation apart from the ultrahigh thermal conductivity of nanotubes, i.e., (1) larger sized code spots, (2) vapor film collapse and fragmentation by nanotubes, (3) enhanced liquid-solid contacts resulting in transient surface quenching and (4) enhanced heat removal surfaces areas. Chen et al (Y. Chen, Mo, Zhao, Ding, & Lu, 2009) investigated

the bubble behaviors on TiO_2 nanotube array coated surfaces that the bubbles departed from the coated surface at smaller diameters and in higher frequencies than the pure Ti metal surface. However, nanotube enhancement for subcooled pool boiling of dielectric liquids presents a different story. In CHF experiments of PF-5060 performed by Sathyamurthi et al (Sathyamurthi, Ahn, Banerjee, & Lau, 2009), CHF enhancement percentage decreased with the increasing liquid subcooling, potentially due to condensation effect during the bubble departure process over an increasing of subcooling. McHale et al (McHale, Garimella, Fisher, & Powell, 2011) compared pool boiling CHF enhancement on smooth and sintered copper surfaces with and without carbon nanotubes for liquids with different wetting ability (HFE-7300 and deionized water). In those experiments, the increased capillary effect of liquids on nanotube coated surface was, however, attributed to enhance both CHF and HTC. Instead of coating nanotubes on heated surfaces, adding nanotubes in working fluids seems a better manner to enhance CHF by utilizing ultrahigh thermal conductivity of nanotubes (Kathiravan, Kumar, Gupta, Chandra, & Jain, 2011; K. J. Park, Jung, & Shim, 2009). It is widely accepted that through modifying thermal properties of working fluids and surface structures only gives limited enhancement to boiling heat transfer performances. Moreover the optimal modification is determined by various factors (Kathiravan et al., 2011). Sarafraz and Hormozi (Sarafraz & Hormozi, 2016) experimentally investigated HTC, CHF and the bubble formation rate for carbon nanotube mixed water boiling on micro-finned surfaces and demonstrated the CHF of nanotubed water on structured surface are greater than the sum of CHF enhanced by two individual techniques. Nevertheless, using nanotube to enhance flow boiling heat transfer is not cases that are observed in pool boiling. In the flow boiling of nanotube mixed water

(Khanikar, Mudawar, & Fisher, 2009), CHF is degraded by nanotubes when the mass flux of flow is 86 kg/m^{2}s. As for this experimental phenomenon, physics explanations are not still covered yet.

2.2.3 Porous Layer Coating and Deposition

Considerable experiments have shown that porous surfaces were potent valid at decreasing incipience of nucleate boiling and enhancing nucleate boiling heat transfer by improving large number of active nucleation sites, although aforementioned enhancement techniques were explored a lot. Numerous mechanisms for boiling through porous surfaces have been suggested and analyzed in various experiments. The first possible mechanism was proposed by Bergles and Chyu (Bergles & Chyu, 1982) that a stable vapor formation kept occurring inside the porous media unlike the ebullition cycle of bubble formation on plain surfaces. Vapors escape channels in the porous medium surrounded by a network of channels supplying liquid and low wall superheat results from a higher surface area offered by porous surface.

The porous network has many cavities that act as active nucleation sites (X. S. Wang, Wang, & Chen, 2010). In their assumptions, when the bigger bubbles detach from the surface, the smaller nucleation cores become active, producing bubbles over and over again. Sintering is a method of producing metal components from powdered metal particles by fusing particles upon the treated surface. Hanlon and Ma (Hanlon & Ma, 2003) fabricated a porous medium from 149 μm average diameter pure particles sintered for 45 minutes most. They investigated how the particle size, the porosity, and the wick structure thickness had impacts on the enhancement of boiling heat transfer. By decreasing the average particle

diameter, HTC can be enhanced. Furthermore, there exists an optimum thickness of porous layer for CHF augmentation. More importantly, the maximum allowable superheat for the film evaporation at the sintered surface is presented to be greatly dependent on wick porosity while weakly determined by the particle radius and the layer thickness. Electrodeposition is the simplest way of fabricating micro and/or nanostructures, involving simple electrochemical process of ion reduction at the cathode by passing direct current through the solution or holding the substrate that is used as cathode at a potential field. El-Genk and Ali (El-Genk & Ali, 2010) utilized a solution mixed with 0.8 mol/L $CuSO_4$ and 1.5 mol/L H_2SO_4 and applied the two-stage direct current technique to deposit porous copper layers on plain copper surfaces. When verifying boiling heat transfer of PF-5060 on those porous layered surfaces, it was observed that 171-μm-thick layer yielded the best boiling heat transfer performances in terms of CHF, HTC and the wall superheat of CHF occurrence. Besides the existence of the optimal thickness, they concluded that an optimal porosity could optimize CHF, HTC and wall superheat.

2.2.4 Acoustic Enhancement of Boiling Process

Instead of modifying surface structures and altering thermal physical properties of fluids and heat surfaces, it is a plausible method to extrinsically excite the motions of bubbles and liquid bulks through applying ultrasounds for boiling heat removal performances (Legay, Gondrexon, Le Person, Boldo, & Bontemps, 2011).

The acoustic field was utilized to induce capillary waves on the bubble surface. The waves oscillated largely enough to result in detachment of the bubble from the heated surface. Once bubbles detached from the surface, the acoustic forces can more easily let the bubbles collapse into the bulk liquid to allow for cooler liquid to take its place and improve the heat

transfer from the boiling surface, resulting in increased CHF due to the acoustic enhancement (Jeong & Kwon, 2006). Douglas et al (Douglas, Smith, & Glezer, 2007) reported that the acoustic field generated by a low-power acoustic driver of could increase CHF during pool boiling by as much as 107% and proposed two primary enhancement mechanisms behind the acoustic field: first, the acoustic wave induces capillary waves on the bubble surface, which forces the contact line to shrink, and allows bubbles detach from the surface in a higher frequency; second, the acoustic field provokes radiation forces, as known as Bjerknes forces, that help facilitate the bubble detachment process and suppress the transition to film boiling. Apart from intensification to HTC and CHF, Cai et al (Jun Cai, Huai, Liang, & Li, 2010) conducted the experimental study to investigate the effects of acoustic cavitation on natural convective heat transfer and found that the augmentation at low heat flux was better than that in the case of high heat flux because bubble formation rates have mitigation effects on the acoustic field. Boziuk et al (Boziuk, Smith, & Glezer, 2017) thought that low-power ultrasonic acoustic forces could control the formation and evolution of the vapor bubbles, and inhibits the instability that leads to film boiling at CHF, Although the acoustic actuation can delay the occurrence of CHF and promote HTC of nucleate boiling, the wall superheat also increases owing to the suppression of boiling at most nucleation sites and the removal of small vapor bubbles from active nucleation sites before they can grow significantly. Their experiments showed that the boiling suppression is diminished and wall superheat reduction is achieved when heat surfaces have protrusions, such as ridges, pin fins and porous layers.

2.3 Summaries of Chapter 2

Chapter 2 reviews what factors have influential impacts on CHF and how those factors affect CHF and HTC. Although many analytical CHF models and empirical correlations are proposed to analyze the effects of various factors and predict CHF under particular conditions, there are still some aspects that are not satisfactory including the effects of oxidation, material properties, heater geometries and dimensional sizes of heater. Thermal physical properties of working fluids and the surface morphologies are primary factors of affecting CHF, HTC and ONB. Many enhancement techniques are studied and proposed to improve boiling performances based on these two primary factors, for example, nanoparticles, nano carbon tubes and micro colloids are added into the working fluids to modify the thermal physical properties of working fluids including thermal conductivities, contact angles, wicking, surface tensions and densities of liquid and vapor. Modifying the surface morphologies are primary techniques to improve CHF and HTC, and to decrease ONB and wall superheat. Those surface modification techniques are extensively studied including micro-structures fabrication, micro-porous layers coating and nanoparticle sintering. Although substantial experimental investigations have been performed to show evidences that those surface modification techniques could help augment boiling heat transfer performances, the plausible physical enhancement mechanisms still remain ambiguous and controversial, and corresponding analytical models have limited applications requiring the unmeasurable parameters such as the liquid resupply velocities and bubble departure frequencies. In all enhancement techniques discussed above, each of them needs specific strategies to optimize the maximum CHF and HTC, for example, in nanofluid application, there are optimal concentrations and average diameters of

nanoparticles allowing CHF to be ultimately enhanced, micro pillar array with certain parameters can optimize CHF, those optimal parameters are determined by thermal properties of materials related with heater, working fluids, nano particles and operation conditions. Meanwhile those proposed techniques might improve CHF but deteriorate HTC including nanofluids and micro-porous layers.

3 MICROSTRUCTURE ENHANCED CHF BY DATA-DRIVEN MODELLING

3.1 Pool Boiling CHF Experiments by Microstructures

A lot of efforts have been made for CHF enhancement, such as using materials with higher thermal conductivities as heat transfer medium and/or fluids with higher heat capacities and saturation points as working fluids, modifying surface morphologies. CHF enhancement by surface modification in saturated pool boiling has been widely considered

because recent novel micro fabrication and manufacture techniques enable precise surface modification to be embedded on heat transfer surfaces (Mori & Utaka, 2017).

Regular fin microstructures, one of surface modification techniques, have been investigated in many experiments mainly by means of two microstructure patterns as shown in Fig.3-1. Generally speaking, the pin fin array microstructure holds better enhancement to CHF and HTC than that of the ridge fin array microstructure because the first pin fin array has more liquids filled in gaps between fins than that of ridge fin microstructured surface although both of microstructured surfaces have the same total surface areas. Several physical mechanisms are proposed to explain CHF triggering phenomena observed in microstructure enhanced CHF experiments, such as extended surface areas, higher nucleation site density, improvements of surface wettability, and reinforcement of capillary wicking and critical wavelength decrement of hydrodynamic instability (Mori & Utaka, 2017).

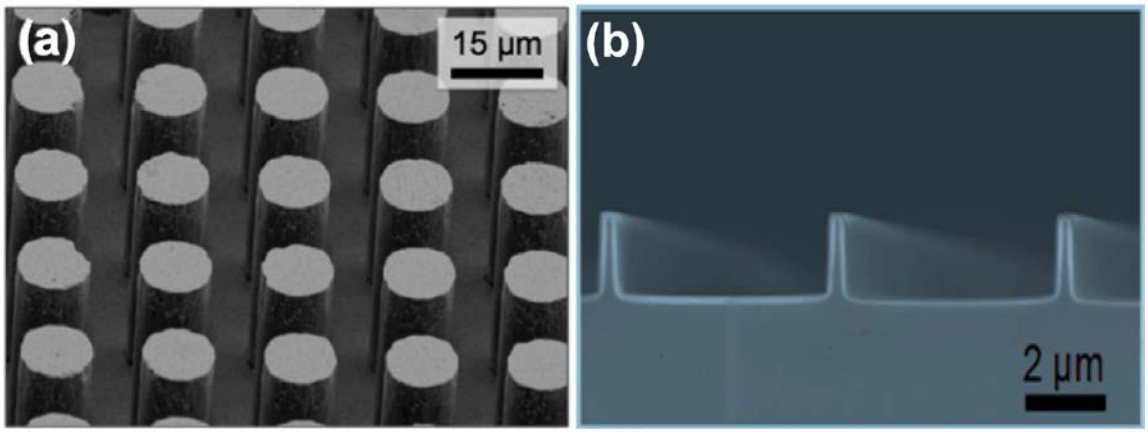

Fig.3-1 Two Microstructure Patterns for CHF Enhancement: (a) Pin Fin (b) Ridge Fin (note that Fig.3-1(a) and (b) are respectively citied from (Rahman, Ölçeroglu, & McCarthy, 2014) and (Zou, Singh, & Maroo, 2016))

In microstructure enhanced CHF experiments, thermal-mechanical properties are examined for various materials and fluids. For example, silicon wafer is often used as a heat transfer substrate material because silicon can be easily and precisely fabricated into different geometries upon a bare silicon surface. Stainless steel and copper are also adopted as sample materials of heat transfer medium in experiments (Choi & No, 2016; C. K. Yu & Lu, 2007) since stainless steel is widely applied in industrial thermal systems and copper has preferred heat conductivity. In addition, microstructures are also applied to flow boiling CHF and HTC (Bigham, Fazeli, & Moghaddam, 2017).

A uniform micro-structured surface can be fabricated via several micro manufacturing methods such as electrical discharge machining(C. K. Yu & Lu, 2007), reactive ion etching (S. H. Kim, Lee, et al., 2015a), laser etching (Shojaeian & Koşar, 2015), chemical vapor etching (Shojaeian & Koşar, 2015), and dry etching (J. J. Wei, Guo, & Honda, 2005). Besides cylindrical pillars with the square lattice distribution, other microstructured pillars shown in Fig.2 are also investigated in pool boiling experiments, such as square pillars, triangular lattice distributed pillars, staggered pillars and piranha pillars. It is noteworthy that piranha pillars in Fig.2 (d) are widely applied to enhance flow boiling CHF. In the pool boiling enhancment by microstructures, both water (K. Chu et al., 2013) and FC-72 (J. J. Wei et al., 2005; Zhang, Zhou, Zhou, Qi, & Wei, 2018a) are often utilized to study the effects of microstructures on CHF, besides, the cylindrical pillars are usually deployed in saturated water pool boiling while the cuboidal pillars are generally investigated in FC-72 subcooled and saturated pool boiling. Considering the influence of oxidized surface materials on improvement of CHF limits, microstructured pillars that are made of silicon

dioxide and copper oxide are respectively evaluated for their CHF enhancement performance (K. H. Chu, Joung, Enright, Buie, & Wang, 2013). In most experimental studies of pool boiling, the heat transfer substrate is cuboidal while the disk-shape transfer surface is examined in a few experiments (Mei, Shao, Gong, Zhu, & Gu, 2018b).

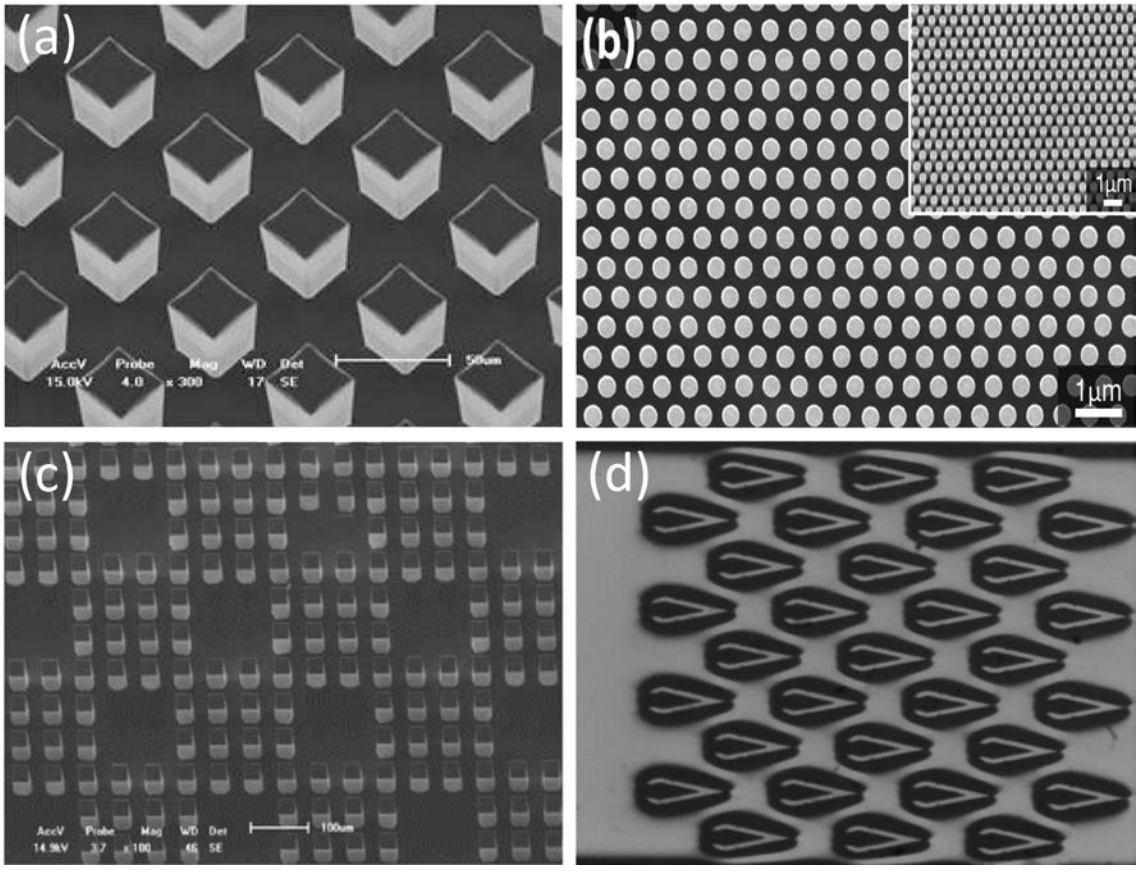

Fig.3-2 Four Different Structures of Pillars: (a) square pillar (Zhang et al., 2018a), (b) triangular lattice (B. S. Kim, Lee, Shin, Choi, & Cho, 2014), (c) aligned pillars (Zhang, Zhou, Zhou, Qi, & Wei, 2018b) and (d) piranha pillars (X. Yu, Woodcock, Wang, Plawsky, & Peles, 2017).

A micro-structured array of micro-pillars on a boiling surface can intensify the heat removal capacity, i.e., increasing CHF and HTC when comparing with pool boiling on a smooth surface. Microstructure enhanced CHF experiments conducted on cuboidal heat transfer substrates are reviewed as follows. In the microstructure enhanced boiling

experiments of Chu et al. (K.-H. Chu, Enright, & Wang, 2011; K. Chu et al., 2013; K. H. Chu et al., 2013), experimental CHF data obtained from microstructured silicon surfaces are harnessed for validating the improved model that accounts for the surface wettability magnification on the basis of Kandlikar's model (Kandlikar, 2001a) and the effects of microstructured material oxidation on CHF enhancement are simulated by depositing silica and copper oxide layers respectively on silicon and copper microstructures. In a set of micropillar enhanced boiling experiments (S. H. Kim, Kang, et al., 2015; S. H. Kim, Lee, et al., 2015a; S. H. Kim et al., 2016a), the critical gap with the optimal CHF is discussed analytically considering the improvement of surface wettability by liquid entrapment between micropillars and the augmentation of dry-region rewetting capability by capillary-induced inflow. In different pool boiling CHF experiments enhanced by engineered micropillars (Dong, Quan, & Cheng, 2014a; B. S. Kim, Lee, et al., 2014; D. E. Kim, Yu, Park, Kwak, & Ahn, 2015; J. M. Kim, Park, Kong, Lee, & Ahn, 2018a; Nguyen et al., 2018; Rahman et al., 2014; D. I. Yu et al., 2018), the capillary-wicking induced flow is regarded as the primary CHF enhancement mechanism on structured surfaces. Park et al.(Y. Park, Kim, Kim, & Kim, 2016) analyzed the fundamental parameters of pool boiling on nano and micro structured surfaces, mainly nucleation site density bubble nucleation frequency and dry area fraction by using an infrared-based detection technique, and argued that the increasing density of nucleation sites might improve CHF limits.

In their successive FC-72 pool boiling experiments (Cao et al., 2018a; Honda, Takamastu, & Wei, 2002a; Kong, Zhang, & Wei, 2018a; J. J. Wei et al., 2005; J. J. Wei & Honda, 2003; J. Wei & Xue, 2011; Xue, Zhao, Wei, Zhang, & Qi, 2013a; M. Yuan, Wei, Xue, &

Fang, 2009a; Zhang et al., 2018a), four distinct experimental conditions are designed for understanding the effects of subcooled temperature, microgravity, nanoparticle deposition, and aligned arrangement of micro-pillars on CHF and HTC. Wei et al. evaluated the enhancement performances of square micopillar structures with different geometrical sizes for CHFs at various subcooled temperatures (Honda, Takamastu, & Wei, 2002b; J. J. Wei et al., 2005; J. J. Wei & Honda, 2003; J. Wei & Xue, 2011; M. Yuan, Wei, Xue, & Fang, 2009b; Zhang et al., 2018a). Experimental results demonstrated that micropillars have much better enhancement to CHF and HTC under the microgravity condition (Xue, Zhao, Wei, Zhang, & Qi, 2013b), and the results shows that allowing micro-pin-finned and smooth areas alternately distributed on the whole surface of heat transfer yields around 20% higher CHF compared to the heated surface completely covered by micropillars (Kong, Zhang, & Wei, 2018b). However, the heat transfer enhancement only by microstructures is limited but depositing nanoparticles on microstructured surfaces can further improve HTC and CHF (Cao et al., 2018b). Rainey et al. (Rainey & You, 2000a; Rainey, You, & Lee, 2003) coated microporous layers on pin-fined copper surfaces to further enhance FC-72 pool boiling heat transfer and corresponding experiments showed that significant increases of HTC but limited improvements of CHF compared to pure pin-finned copper surfaces. Choi et al. (Choi & No, 2015, 2016) extended the hot spot model based on the Walli's correlation to explain the peak profile of CHF with respect to the increasing height of square micropillars. In FC-72 CHF experiments of copper microstructure enhanced pool boiling (S. Lee & Chien, 2011a; C. K. Yu & Lu, 2007), through bubble visualization, it is revealed that nucleate boiling was initiated from the tip of the pillar, then spread to the pillar foot where the denser and/or higher pillar array

initiates nucleate boiling at lower wall superheat. The maximum CHF of FC-72 obtained from the pin-finned surface is five times greater than that of the plain surface.

Details about the experiments discussed above are included in **Tab.3-1**. Noting that all experiments listed in **Tab.3-1** are performed on the upward horizontal surfaces, the materials of heat transfer substrates are the same to that of pillars arrays. Apart from cylindrical and square pillars, other novel geometries are also investigated in microstructure-enhanced pool boiling, such as hoodoo-shaped silicon pillar array (Guan, Bon, Klausner, & Mei, 2014), elliptical pin fins (Ndao, Peles, & Jensen, 2014), hydrofoil pin fins (Ndao et al., 2014) and diamond pin fins (Ndao et al., 2014). In addition, nanowire coated surfaces have the similar enhancement with microstructured surfaces but only differ in that the geometrical parameters of nanowires are not fixed for an individual surface (B. S. Kim, Choi, Shin, Gemming, & Cho, 2016). The databank of microstructure enhanced CHF experiments is presented in Appendix.

The experimental studies confirm that the linear relation between subcooled temperature and CHF also holds true for subcooled pool boiling enhanced by microstructures. From **Tab.3-1, Tab. V** and **Tab. VI**, the significant difference is found in the dimension scales of pillars that are made of different materials: the geometrical parameters of silicon pillars are usually scaled from nanometers to micrometers while copper pillars are fabricated on a plain surface at a scale of millimeters. Because of the scale effect of hydraulics, the CHF enhancement mechanisms of silicon pillars at micrometer scales may present a different story from those at millimeter scales. Whether the effects of the distribution pattern and

geometry of pillars can be correlated by r and φ_s are not validated in experiments yet. Hydrophilic surfaces have higher CHF while HTC is higher for pool boiling on hydrophobic surfaces, and much higher CHF can be obtained on the surface embedded with hydrophilic and hydrophobic in a certain manner. Fabricating micro-pillars meanwhile leaving some regions untouched on a plain surface have similar pool boiling enhancement to a hydrophilic and hydrophobic mixed surface because a microstructured surfaces has higher CHF and lower HTC compared to a plain surface (Cao et al., 2018a; Kong et al., 2018b). Therefore, how to balance pin-finned and untouched regions for achieving the maximum microstructure-enhanced CHF should be explored in future experiments. Besides, whether the optimal geometrical parameters of pillars are dependent on the dimensional sizes of heat transfer substrate or not are not covered by experimental or theoretical studies.

3.2 The effects of geometries of pillar array

The rationale for microstructure enhanced CHF still remains controversial although several mechanical interpretations are proposed to explain the enhancement mechanisms such as wettability (Kong, Wei, Deng, & Zhang, 2017), wickability (Rahman et al., 2014), hydrodynamic instability (Quan, Dong, & Cheng, 2014), incremental of total surface area and nucleation site density (Zou et al., 2016). Most of microstructure enhanced CHF experiments, however, supports the wickability improved by capillary-induced flow as the primary CHF enhancement mechanism on structured surfaces (Shojaeian & Koşar, 2015). The parametrical trends of CHF with respect to geometrical parameters of pillars can be qualitatively analyzed even if related CHF enhancement mechanisms are still ambiguous.

Kim et al. (S. H. Kim, Lee, et al., 2015a) analyzed the effects of spacing on CHF and discussed the optimal spacing between micropillars through analysis of the capillary flow rate on the structured surface. Given pillar arrays with specific diameter and height, small spacing can generate a compact pillar array that makes it difficult for liquid to rewet the dry region between micro-pillars, thus resulting in low CHF. On the other hand, big spacing leads to fewer sparsely-distributed micropillars and reduces the capillary forces of pillars, resulting in low spreading velocity of liquid and CHF decrement. Accordingly, the spacing-variant CHF behavior presents a concave trend and the CHF enhancement effect will be negligible if spacing is much greater than diameter and height. In an engineered surface with large diameter pillars, bubbles are initiated at the tip of the fin and then spread to the root of pillars (C. K. Yu & Lu, 2007). Thus CHF very likely occurs on the top surfaces of large diameter pillars, which results in little-enhanced CHF. If diameter is much smaller than height and spacing, heat removal by pillars is limited and CHF occurs first at the root of pillars, resulting in lower CHF. Moreover, Li et al.(R. Li & Huang, 2017) pointed out that CHF is proportional to the flow velocity of the surface rewetting liquid following a concave function of diameter. Consequently, there exists a critical diameter that can ultimately enhance CHF of microstructured surfaces. Compared with that of diameter and spacing, the effects of increasing height on CHF are thought more complicated due to multiple mechanisms acting together, such as bubble departure frequency degradation, vapor film fragmentation enhancement (Zou & Maroo, 2013), bubble entrapment enhancement (Rainey et al., 2003), and the surface area increment. It can be postulated that there should be an optimal height for pillars with specific diameter and spacing because CHF enhancement by very short pillars is limited, while bubbles along the axial surface of

long pillars tend to form vapor regions that result in lower CHF. The effects of pillar shape and distribution patterns are not elaborated in experiments but cylindrical pillars with square lattice distribution pattern may have better enhancement performance due to the higher solid fraction and fluidic resistance.

3.3 Physical CHF Models and Discussions

Physical models, which account for the effects of microstructures, are developed on the assumed mechanisms discussed above and cannot cover multiple mechanisms. However, explicit CHF triggering mechanisms remains ambiguous although many relevant experiments have been performed. Consequently, applications of current physical models are limited.

For example, Rahman et al (Rahman et al., 2014) proposed a hydrodynamics-wavelength based model that correlates with wicked volume flux at the occurrence of CHF but the wicked volume flux is difficult to be measured in industrial applications. The objective of this study is to compile the databank of microstructure enhanced CHF for future model developments that account for the effect of microstructures. At the same time, this study evaluates advantages and disadvantages of current physical CHF models.

In papers (Liang & Mudawar, 2018b; M. C. Lu, Huang, Huang, & Chen, 2015a; Rainey & You, 2001), the material, area, and thickness of heat transfer substrate have impacts on the pool boiling CHF although the thermal-mechanical properties of working fluids are correlated by Zuber model, which models CHF in saturated pool boiling of a specific liquid on any upward-facing infinite horizontal smooth surface. The dimensionless CHF K is

often adopted to correct for the effects of medium materials, surface orientation, subcooled temperature, surface wettability, wickability among others, defined as the ratio of the experimental CHF to the predicted CHF of Zuber model. Kandlikar (Kandlikar, 2001a) correlated the effects of surface wettability and surface orientation on CHF as follows:

$$K = \frac{1+cos\beta_{rec}}{16}\left(\frac{2}{\pi} + \frac{\pi}{4}(1 + cos\beta_c)cos\phi\right)^{1/2} \quad (3\text{-}1)$$

, where β_c is the receding contact angle of the plain surface and ϕ is the inclination angle of surface orientation (in this study, $\phi = 0°$).

Tab.3-1 CHF Studies on Microstructures over Flat Surfaces for Pool Boiling

ID	Reference	Fluid	Pressure	Subcooled	Material	Substrate Dimension (mm^3)	Pillar Shape	Physics Modeled	Features
1	Chu et al. (K. Chu et al., 2013)	water	1 atm	0 K	Si	20×20×0.635	Cylindrical	Yes	the extended model based on Kandlikar correlation(Kandlikar, 2001a)
2	Chu et al. (K.-H. Chu et al., 2011)	water	1 atm	0 K	Si	20×20×0.635	Cylindrical	Yes	as above
3	Chu et al. (K. H. Chu et al., 2013)	water	1 atm	0 K	SiO_2 CuO	20×20×0.635	Cylindrical	Yes	as above, surface oxidation and roughen of pillars
4	Kim et al. (S. H. Kim, Lee, et al., 2015a)	water	1 atm	0 K	Si	28×25×0.5	Cylindrical	No	fin efficiency evaluation ,liquid inflow modelling by capillary pressure and friction
5	Kim et al. (S. H. Kim, Kang, et al., 2015)	water	1 atm	0 K	Si	28×25×0.5	Cylindrical	No	as above
6	Kim et al. (S. H. Kim et al., 2016b)	water	1 atm	0 K	Si	28×25×0.5	Cylindrical	No	heat flux partitioning analysis through essential parameters of bubble
7	Rahman et al. (Rahman et al., 2014)	water	1 atm	0 K	Si	10×10×1	Cylindrical	Yes	hydrodynamic analysis, nanowire-coated micropillars
8	Kim et al. (D. E. Kim et al., 2015)	water	1 atm	0 K	Si	15×10×0.5	Cylindrical	Yes	bubble dynamics analysis

9	Nguyen et al. (Nguyen et al., 2018)	FC-72	1 atm	0 K	Si	10×10×0.5	Cylindrical	Yes	nanoscale-pillar induced rewetting velocity analysis
10	Moon et al.(Moon, Yoon, Park, Myung, & Kim, 2016)	water	1 atm	0 K	Si	15×10×0.525	Cylindrical	No	comparison between micro-sized pillars and cavities
11	Kim et al. (B. S. Kim, Lee, et al., 2014)	water	1 atm	0 K	Si	10×5×0.5	Cylindrical*	Yes	the hydrodynamic analysis of wickability
12	Kim et al. (J. M. Kim, Park, Kong, Lee, & Ahn, 2018b)	water	1 atm	0 K	Si	25×20×0.475	Cylindrical	No	micropillars coated with porous graphene networks
13	Park et al.(Y. Park et al., 2016)	water	1 atm	0 K	Si	20×10×0.5	Cylindrical	No	bubble dynamics analysis
14	Dong et al.(Dong, Quan, & Cheng, 2014b)	Ethanol	1 atm	0 K	Si	15×15×0.5	Cylindrical	No	CHF enhancement comparison between pillars and cavities
15	Yu et al. (D. I. Yu et al., 2018)	water	1 atm	0 K	Si	10×10×NA	Cylindrical	No	capillary-induced flow analyses synchrotron x-ray imaging
16	Ho et al.	FC-72	1 atm	0 K	$AlSi_{10}Mg$	10×10×1	Cylindrical	Yes	the modified Rohsenow model accounting for pillars' effects

	(Ho, Wong, & Leong, 2016)								
17	Wei et al. (J. J. Wei & Honda, 2003)	FC-72	1 atm	0,3, 25,45 K	Si	10×10×0.5	Square	No	the influence of dissolved gas and orientation on CHF
18	Wei et al. (J. J. Wei et al., 2005)	FC-72	1 atm	3,25, 35,45 K	Si	10×10×0.5	Square	No	fin efficiency evaluation
19	Zhang et al.(Zhang et al., 2018a)	FC-72	1 atm	15,25,35 K	Si	10×10×0.5	Square	Yes	semiempirical CHF regression for micropillars and subcooling
20	Honda et al.(Honda et al., 2002b)	FC-72	1 atm	0,3, 25,45 K	Si	10×10×0.5	Square	No	enhancement comparison between roughened and pin-fined surfaces
21	Choi et al .(Choi & No, 2015, 2016)	water	1 atm	0 K	stainless steel	50 ×15 ×2	Square	Yes	CHF modelling based on capillary and counter-current flow, hot spot
22	Rainey et al.(Rainey & You, 2000b; Rainey et al., 2003)	FC-72	30,60, 100,150 kPa	0,10, 30,50 K	Cu	10×10×2	Square	No	heat transfer comparison between microporous-coated and pin-fined surfaces
23	Lee et al. (S. Lee & Chien, 2011b)	FC-72	78.18 kPa	0 K	Cu	10×10×2	Square	No	HTC and CHF evaluation between ridged and pin-fined surfaces

24	Yu et al. (C. K. Yu & Lu, 2007)	FC-72	1 atm	0 K	Cu	10×10×2	Square	No	studies about effects of pillars on boiling incipience
25	Kong et al.(Kong et al., 2018b)	FC-72	1 atm	15,25,35 K	Si	10×10×0.5	Square	No	CHF comparison of different distribution patterns of pillars
26	Cao et al. (Cao et al., 2018a)	FC-72	1 atm	15,25,35 K	Si	10×10×0.5	Square⋆	No	further enhancement of micro-pin-finned surface CHF by nanoparticle deposition
27	Xue et al. (Xue et al., 2013a)	FC-72	1 atm	32,41,43 K	Si	10×10×0.5	Square	No	bubble dynamics analysis of microstructure enhanced boiling under microgravity condition
28	Kim et al. (S. Kim et al., 2010)	water	1 atm	0 K	Si	15×10×0.5	Cylindrical	No	dual CHF enhancement studies via nanofluids and nanostructures

Notes: ⋆ represents the triangular distribution pattern of pillars.

On the basis of the Kandlikar model, Chu et al.(K.-H. Chu et al., 2011; K. Chu et al., 2013; K. H. Chu et al., 2013) extended to account for the effects of micro pillars on CHF as follows:

$$K = \frac{1+cos\beta}{16}\left(\frac{2(1+rcos\beta_c)}{\pi(1+cos\beta)} + \frac{\pi}{4}(1+cos\beta)cos\phi\right)^{1/2} \quad (3\text{-}2)$$

, where r denotsthe ratio of total surface area to the projected area ($r = 1 + \pi dh/(d+s)^2$), and β is the apparent receding contact angle which can estimated with Extand's proposed model (Extrand, 2016),

$$\beta = \frac{1}{1+2s/\pi d}(\beta_c - 180°) + 180° \quad (3\text{-}3)$$

but $cos\beta = 1$ if $rcos\beta_c > 1$. Terms, h, d and s indicate the height, diameter and spacing of the cylindrical pillar respectively. In the papers (Nguyen et al., 2018; Rahman et al., 2014), the effects of microstructures on CHF are correlated based on the hydrodynamics model of Eq.(3-4) coupled with measured indicators of micro pillar induced capillary wickability, such as the measured wicked volume flux $\dot{V}_0^{"}$ and the measured velocity of liquid inflow δv_{ca}

$$K = 1 + \frac{\dot{V}_0^{"}\rho_l}{\rho_v^{1/2}(\sigma g(\rho_l - \rho_v))^{1/4}} \quad (3\text{-}4)$$

where $\dot{V}_0^{"}$ is assumed here, however, to scale linearly with δv_{ca}, ρ_l and ρ_v are respectively the liquid and vapor densities of working fluid, σ is the surface tension of the liquid and g is the local gravitational acceleration. Nevertheless, it is difficult to measure those two parameters in practical applications. The analytical prediction methods of average liquid inflow velocity can approximate these two parameters with fair accuracy (S. H. Kim, Lee, et al., 2015a; Mai et al., 2012). Instead of incorporating effects of microstructures into the dimensionless CHF, the enhanced CHF, due to surface rewetting by the capillarity-induced

liquid, is considered to linearly superpose upon the CHF of Kandlikar's model (B. S. Kim, Lee, et al., 2014; R. Li & Huang, 2017), expressed as a sum of two terms

$$q''_{pillar-CHF} = q''_{Kandlikar-CHF|plain} + q''_{enhanced\ CHF} \tag{3-5}$$

In Eq.(3-5), $q''_{enhanced\ CHF}$ can be derived based on different assumptions: Kim et al. (B. S. Kim, Lee, et al., 2014) derived the enhanced CHF from the wickability dependence on capillary pressure and hydraulic resistance as follows,

$$q''_{enhanced\ CHF} = C_1 \frac{h_{lv}\rho_l(1-\varphi_s)W^2}{\lambda_{RT}^2} \tag{3-6}$$

where C_1 is the compensating factor for the wicking capacity, $h_{lv}$is the latent heat of fluid, λ_{RT} is the Rayleigh–Taylor wavelength (Kandlikar, 2001a) and W is the wicking coefficient, satisfying as follows,

$$W = \frac{2}{3(1+4h^2/w^2)} \frac{\sigma h}{\mu} \frac{cos\beta_c - cos\theta_c}{cos\theta_c} \tag{3-7}$$

in Eq.(3-7), μ is the viscosity of the liquid, w is the characteristic width of the pillar and θ_c is the critical angle (more details about w and θ_c, see (Mai et al., 2012)); Li et al. (R. Li & Huang, 2017) assumed that the liquid film had the same height as the pillars and based on the balance equation between energy that the bubble absorbs and the evaporation heat of liquid inflow to derive the additional CHF that evaporates the capillarity-induced liquid supply as follows,

$$q''_{enhanced\ CHF} = C_2 \frac{h_{lv}hsd}{(s+d)^2} \sqrt{sg\rho_l cos\beta_c(\rho_l - \rho_v)} \tag{3-8}$$

where C_2 is a resultant factor obtained by experimental data fitting.

In the physical models discussed above, CHF models of Chu et al.(K. Chu et al., 2013), and Kim et al.(B. S. Kim, Lee, et al., 2014) are dependent on the apparent contact angle. In practical applications, it is implausible to measure the apparent contact angle

experimentally for CHF prediction. As a result, it is of importance to estimate the apparent contact angle of bubbles on the microstructured surface in an accurate manner. Besides the estimation method proposed by Extand (Extrand, 2016), a piece-wise estimation method of contact angle is suggested in the paper (R. Li & Huang, 2017), as follows,

$$\cos\beta = \begin{cases} r\cos\beta_c \text{ , if } \beta_c \geq \theta_c \\ 1 + \varphi_s(\cos\beta_c - 1), \text{if } \beta_c < \theta_c \end{cases} \tag{3-9}$$

where φ_s is the solid fraction defined as the ratio of the area of the top of the pillar to the projected area ($\varphi_s = 0.25\pi d^2/(d+s)^2$), it should be noteworthy that $\cos\beta = r\cos\beta_c$ is the Wenzel contact model for any roughened surface (Bhushan & Chae Jung, 2007).

Prediction performance of various physical models is evaluated through the experimental microstructure-enhanced CHF datasets of saturated water pool boiling from (K.-H. Chu et al., 2011; K. Chu et al., 2013; K. H. Chu et al., 2013; B. S. Kim, Lee, et al., 2014; D. E. Kim et al., 2015; J. M. Kim, Park, et al., 2018b; S. H. Kim, Kang, et al., 2015; S. H. Kim, Lee, et al., 2015a; S. H. Kim et al., 2016b; Y. Park et al., 2016; Rahman et al., 2014). Due to the triangular lattice distribution of micropillars in (B. S. Kim, Lee, et al., 2014), both r and φ_s are increased by a factor of $2/\sqrt{3}$. The hydrodynamics CHF model proposed in papers (Nguyen et al., 2018; Rahman et al., 2014) is dependent on the measured wicked volume flux or the measured velocity of liquid inflow. However, in this study, the velocity of liquid inflow is estimated by the approximation method of Mai et al. (Mai et al., 2012), and the capillary pressure is calculated by a theoretical model proposed by Hale et al. (Hale, Ranjan, & Hidrovo, 2014a). All three constants, the scale factor in (Nguyen et al., 2018), the compensating factor (B. S. Kim, Lee, et al., 2014), and the resultant factor in (R. Li & Huang, 2017) are obtained by a data-fitting technique. In order to consistently evaluate the

prediction performance between various physical models discussed above, 82 experimental CHF data of cylindrical micropillar surfaces are screened and comparative results are shown in Fig.3-3. It is noteworthy that the model proposed by Li et al. (R. Li & Huang, 2017) has the best prediction performance compared with the other four physical models as indicated by the coefficient of determination (R^2).

It should be noted that the hydrodynamics-based CHF model proposed in (Nguyen et al., 2018; Rahman et al., 2014) is not necessarily valid due to two factors. First, while papers (Nguyen et al., 2018; Rahman et al., 2014) used measurements of rewetting velocity or wicked volume flux to predict CHF , in this study, the rewetting velocity is approximated with the mean velocity proposed by Mai et al. (Mai et al., 2012) . Second, this study adopts a first-order approximation of surface-energy based model from (Hale, Ranjan, & Hidrovo, 2014b) as the capillary pressure required in (Mai et al., 2012). As shown in Fig.3-3, the models of Chu et al. (K. Chu et al., 2013) and Kim et al.(B. S. Kim, Lee, et al., 2014), tend to overestimate the CHF predicted value when the true CHF is less than 1400 kW/m^2. However, all physical models generally underestimate the predicted value when the true CHF is above 1900 kW/m^2.

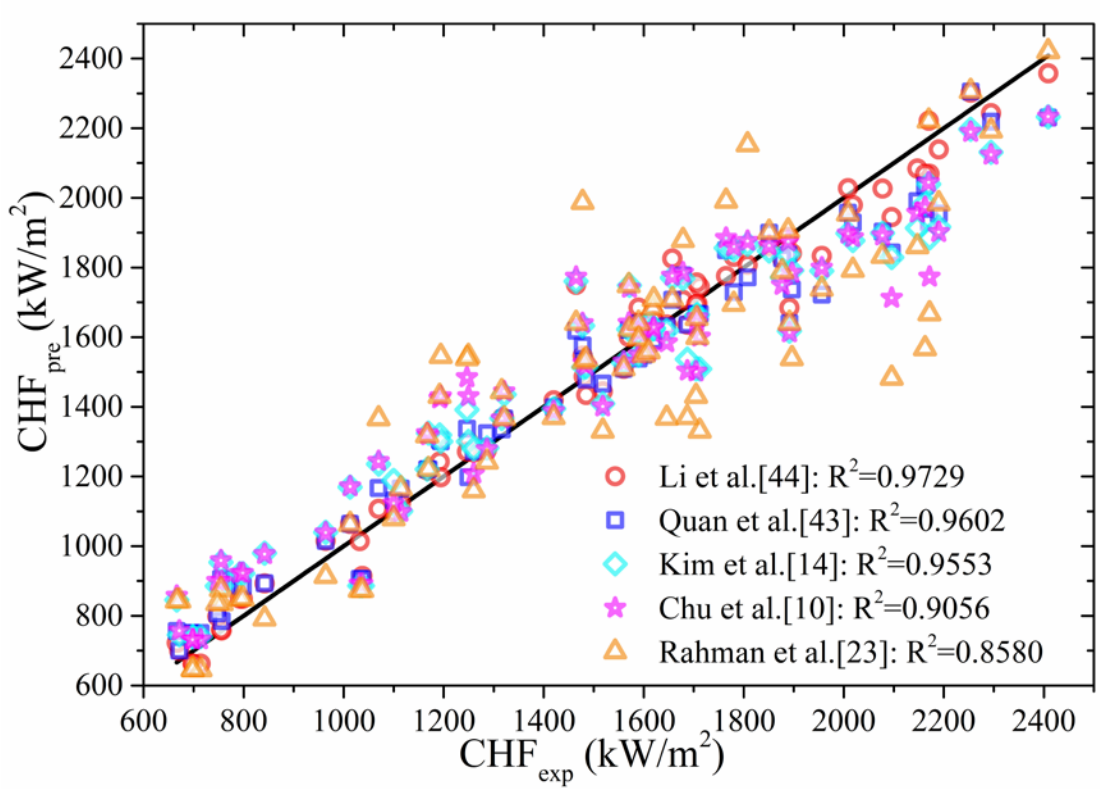

Fig.3-3 Comparisons of different models with experimental microstructure enhanced CHF

Although the CHF physical models discussed above are able to predict CHF of microstructure enhanced saturated pool boiling water with a high level of accuracy, further analyses of parametrical trends are necessary to verify model veracity. Because of their relatively low prediction accuracy and measurement requirements , the model proposed by Chu et al.(K. Chu et al., 2013) and the hydrodynamics-based models (Nguyen et al., 2018; Rahman et al., 2014) are not assessed in terms of parametrical trends and convergence. The experimental CHF datasets of microstructured surfaces from (S. H. Kim, Lee, et al., 2015a) are utilized for model verification.

Before discussing model convergence and parametrical trends, zero-infinity convergence is introduced to define how physical models correlate with positive effects of

microstructures on pool boiling CHF. The zero-infinity convergence means that the model is supposed to converge to the CHF behaviors if the diameter, height, or spacing approaches zero or an "infinitely big magnitude," (here "infinitely big" means that the magnitude of one parameter is at least 50~100 times greater than that of other one.) but at least one of other two variables is positive. For example, if diameter is zero but either height or spacing or both are greater than zero, the K value of this imaginary microstructured surface will be equal to 1. This means that regardless of height and spacing, all CHF profiles start from the point (d=0, $CHF_{\text{plain surface}}$). Infinity-convergence denotes that CHF is limitedly enhanced or even not enhanced at all when diameter, height, or spacing is much greater than other two parameters. For instance, in an experimental case from the paper (D. E. Kim et al., 2015), diameter and height of micro-pillar array are fixed at 80 um and 20 um, respectively, and spacing is 240 um, but the CHF of this microstructured surface is 1114.40 kW/m^2, slightly greater than the CHF of plain surface 1100 kW/m^2. It can be anticipated that the further increasing spacing will force the CHF of the sparsely-distributed pillared surface approach 1100 kW/m^2.

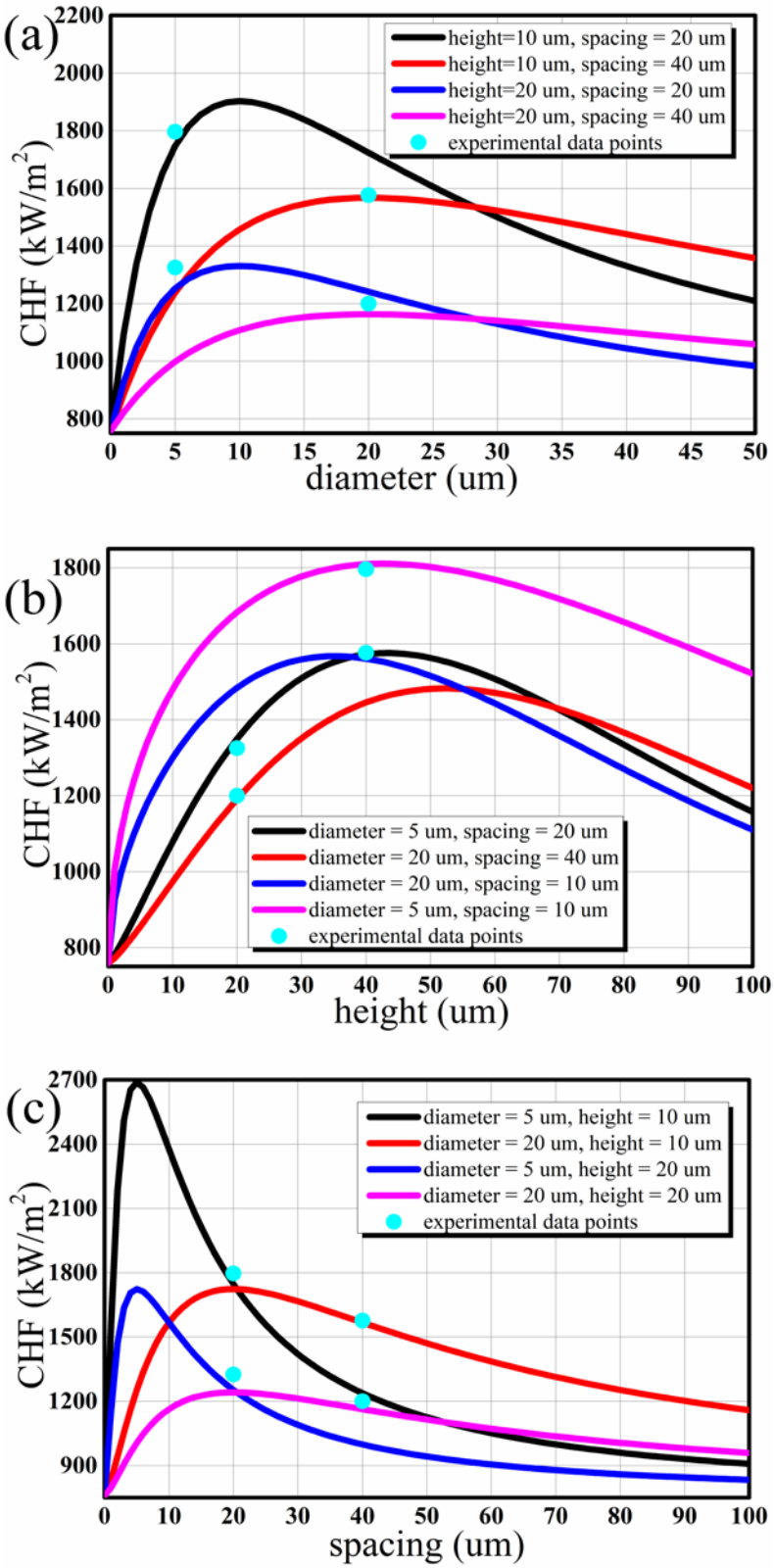

Fig.3-4 Parametrical Trends of CHF with respect to: (a) diameter, (b) height and (c) spacing in the Model of Li et al. (R. Li & Huang, 2017).

For models of Li et al.(R. Li & Huang, 2017) and Kim et al.(B. S. Kim, Lee, et al., 2014), the parametrical trends are respectively shown in Fig.3-4 and Fig.3-5 with respect to diameter, height, and spacing. As observed in Fig.3-4, the CHF model of Li et al.(R. Li & Huang, 2017) presents zero-convergence for diameter, height, and spacing and achieves the infinity convergences of diameter and spacing. However, Fig.3-4 (b) demonstrates that the height-variant CHF profile presents a concave parametric trend, resulting in the CHF convergence as the increasing height. This is in agreement with the effects of height on CHF because the relation between height and CHF is nonlinear and the height-variant CHF profile should follow a concave trend. However, the reason why the CHF model of Li et al.(R. Li & Huang, 2017) fails at CHF prediction is that the thickness of liquid film is assumed same as the height of pillars, and the total heat carried by bubbles is assumed to have a linear relation with the total volume rate of rewetting liquid that is proportional to the thickness of liquid film. For the model of Kim et al.(B. S. Kim, Lee, et al., 2014), the spacing-variant CHF behavior is in accordance with the zero-infinity convergence as demonstrated in Fig.3-5 (c). But the improvement of CHF enhancement by the increasing height of pillar arrays is limited once the height is above a certain value because of the model dependence on $(w^2\,h^2)/(4h^2+w^2)$. Whether the diameter-variant CHF is in agreement with zero-infinity convergence is determined by the height and spacing as shown in Fig.3-5(a). It is possibly because the model of Kim et al.(B. S. Kim, Lee, et al., 2014) is developed on the basis that CHF occurs at the bottom regions between pillars. This assumption holds true if the height reaches a certain value that can allow bubbles to coalesce together and form vapor film before their departure from micro-pillars, otherwise CHF occurs at the top surface of micropillars and the gap between pillars is filled with

liquid, therefore deteriorating the basis of the model proposed by Kim et al.(B. S. Kim, Lee, et al., 2014).

Based on discussions above, theoretical CHF models have several drawbacks. For example, the models proposed in (Nguyen et al., 2018; Rahman et al., 2014) depend on measurements of rewetting liquid volume flux or rewetting velocity. The model of Li et al.(R. Li & Huang, 2017) does not capture the nonlinear trend of CHF with respect to height. Besides the application ranges of theoretical CHF models are tough to be determined because theoretical models are on the basis of various bubble growth assumptions. For instance, when bubbles are about to depart from surface, the gap space between pillars can be assumed to be fully filled with liquid only or vapor only. On the one hand, theoretical studies are developed based on single enhancement mechanisms such as the augmented wettability, the intensified capillary wickability and so on. On the other hand, it is difficult to isolate the individual effects of single geometrical parameters of pillar arrays on CHF enhancements for mechanisms analyses because the CHF trigger mechanisms result from multiple effects of pillared surface. When the spacing between pillars is large, bubbles can be initiated at the tip, side and root of pillars, while bubbles start to grow on the tip surface of pillars. Microscopic pillar arrays have different enhancement mechanisms on CHF from that of macroscopic pillar arrays. Thus, CHF models based on the observed phenomena of micro-pillar arrays can not be applied to predict CHF enhanced by macro-pillar arrays because of the effects of dimensional scale. Therefore, the parametrical trends of CHF with respect to the geometrical parameters of

pillar arrays present nonlinear and complicated behaviors that are not accurately correlated by theoretical models.

It should be pointed out that pool boiling CHF can change with the dimensional sizes of heat transfer substrate or geometrical shapes if the dimensional sizes are below a certain critical size. For instance, if the dimensionless size of silicon heater is greater than 5 (i.e., the ratio of the heater characteristic dimension, to the Taylor instability wavelength), the pool boiling regime will be assumed in a “infinitely large heater” configuration and the heater size will be considered independent of CHF, otherwise, the pool boiling regime will be regarded on a small heater, the size of which has influential effects on CHF (H. Yang & Banerjee, 2016). Besides, the certain critical size is dependent on working fluids, heater materials, operation pressures and etc. However, in current pool boiling CHF experiments where the effects of heater sizes and shape are often ignored, most of them fall in the regime of small heater.

As a result, it is not clear whether the CHF enhancements reported in microstructure enhanced CHF studies are caused by the heater size issues or the geometrical parameters of pillar arrays. As a consequence, similar experiments performed on different heater sizes yield inconsistent results. And different CHF models are proposed based on various observations of CHF occurrence, thus resulting in biased CHF predictions. On different size microstructured surfaces with same pillar arrays, the total number of pillars differs, which may be attributed to the different CHF enhancement ratios. However, this quantity difference of pillars between structured surfaces with different dimensions are not covered by experimental and theoretical studies. In the light of complexity and nonlinearity rooted

in microstructure enhanced CHF relation to geometrical parameters and heat transfer substrate sizes, machine learning techniques can help model the CHF regression. While traditional machine learning approaches successfully solve problems with final values that are a simple function of input data, on the contrary, deep learning techniques are able to capture composite relations between input and output datasets.

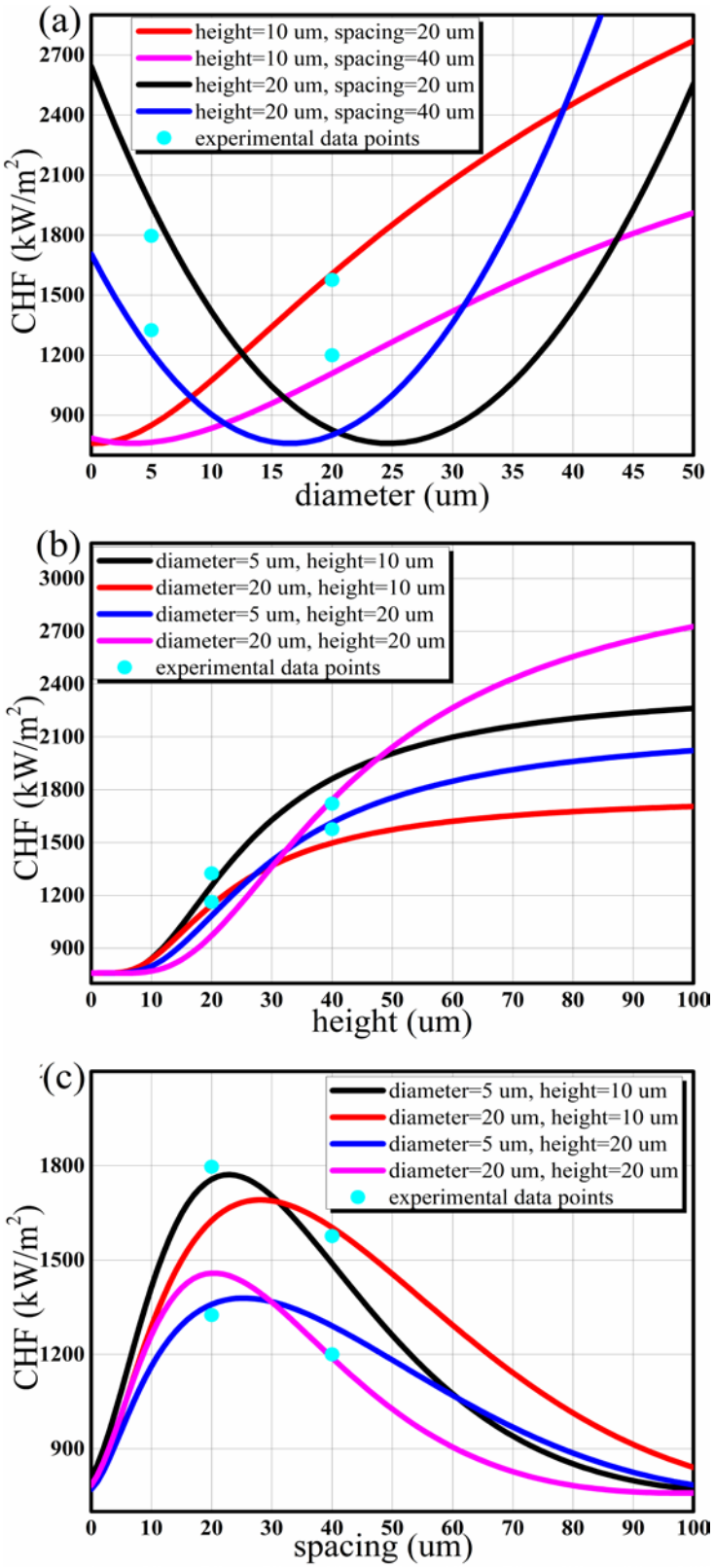

Fig.3-5 Parametrical Trends of CHF with respect to: (a) diameter, (b) height and (c) spacing in the Model of Kim et al.(B. S. Kim, Lee, et al., 2014).

As a class deep learning technique, deep belief net (DBN) is a probabilistic generative model that is composed of multiple layers of stochastic, latent variables and it is able to regress the nonlinear and complicated relationship hidden in the training datasets (F. Li et al., 2018). In this study, DBN is utilized to develop a prediction framework of microstructure-enhanced CHF and study the parametrical trends of CHF with respect to geometrical parameters of micro-pillars.

3.4 Deep Belief Network Modelling for Microstructure Enhanced CHF

DBN is a class of deep feed-forward neural network that is composed of multiple hidden layers of graphical models having both directed and undirected edges, and is capable of revealing complicated patterns deeply rooted in datasets. As shown in Fig.3-3, DBN is composed of two modules: an unsupervised feature extraction module sequentially stacked by RBMs, and a supervised perceptron for data classification and regression (F. Li et al., 2018). In the stacked structure of DBN, the visible layer of the former RBM is the hidden (latent) layer of the latter RBM. RBM is a two-layer (visible layer and hidden layer) probabilistic neural network. Both visible and hidden (latent) units of RBM are binary and stochastic in terms of the data characteristics, and its visible units can be accurately reconstructed based on its hidden units through unsupervised training of a RBM. This suggests that the visible units can be exactly represented by the hidden units in a different dimensional space, and no information is lost during data transformation. Representing a dataset in a different dimensional (especially high-dimensional) space improves the ability of the network in revealing the patterns hidden in the training datasets. Once a RBM is trained, its hidden units are supposed as visible units for the next RBM, initiating the

following unsupervised training of the next RBM. The network input data (i.e. the geometrical parameters of micro-pillars) can be represented in multiple high-dimensional spaces through utilizing a stack of RBMs, resulting in the higher regression accuracy of nonlinear and complicated relation hidden in training sets. Subsequently, outputs from the RBMs and the original inputs are passed to the perceptron for CHF regression. The perceptron is a feedforward neural network trained by a back-propagation algorithm, and models the CHF as a function of the outputs from the RBMs.

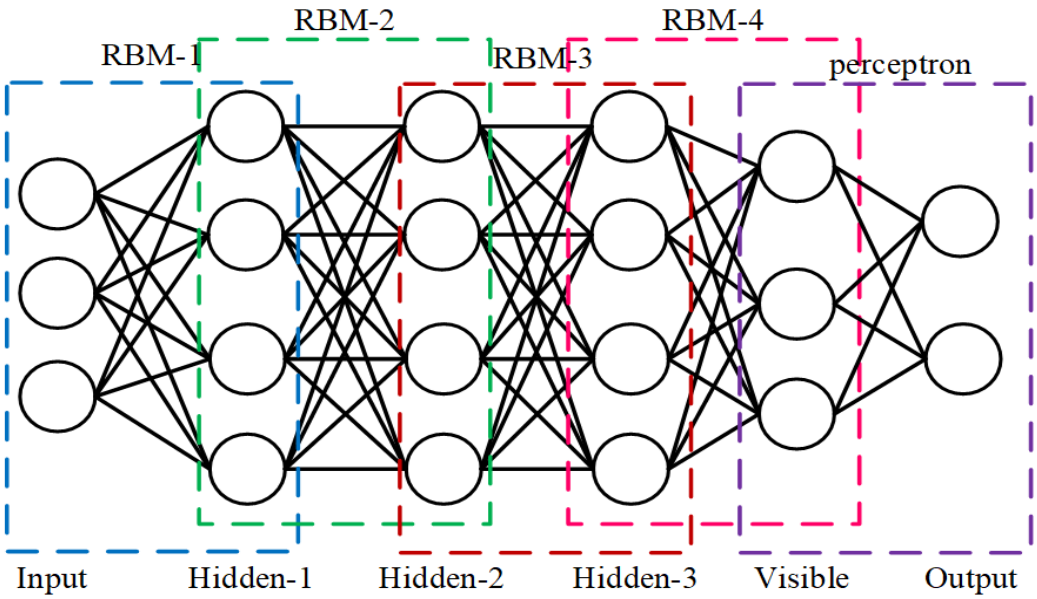

Fig.3-3 DBN Structure with four RBMs and one Perceptron

The training process of DBN is divided into unsupervised and supervised training stages: unsupervised training is implemented by contrastive divergence algorithm and the input target of training datasets for obtaining the initial weight matrixes of the stacked RBMs $\boldsymbol{W^R} = (\boldsymbol{w_1^R}, \boldsymbol{w_2^R}, \ldots, \boldsymbol{w_l^R})$; then the supervised training is implemented by error back-propagation algorithm based on the input and output targets of training datasets, which fine-tunes the initial weight matrixes to acquire the final global optimal weight matrixes $\boldsymbol{W} = (\boldsymbol{w_1}, \boldsymbol{w_2}, \ldots, \boldsymbol{w_l}, \boldsymbol{w_p})$. Noting that l is the number of stacked RBMs, w_l^R and w_l are

the pre-trained and fine-tuned weight matrixes for the lth RBM, and w_p is the weight matrix of perceptron layer.

The main intention of unsupervised training is to determine the initial weights only by using input target samples of training datasets (i.e. the geometrical parameters of micropillars), which is enacted by training the sequentially-stacked RBMs. In a typical RBM, there are *I* hidden units in the hidden layer $\boldsymbol{h}$ and *J* visible units in the visible layer $\boldsymbol{v}$, respectively denoted by $\boldsymbol{h} = (h_1, h_2, \dots, h_I)$ and $\boldsymbol{v} = (v_1, v_2, \dots, v_J)$; the corresponding initial weight matrix is $\boldsymbol{w^R}$. the RBM uses the conditional probability $p(\boldsymbol{h}|\boldsymbol{v})$ to calculate the value of each unit in the hidden layer, and then uses the conditional probability $p(\mathbf{h}|\boldsymbol{v})$ to calculate the value of each unit in the visible layer. This process is performed repeatedly until the rank of initial weight matrix converges. Two conditional probabilities are derived from the joint probability of RBM, which is defined as follows:

$$\mathrm{p}(\boldsymbol{v}, \boldsymbol{h}; \theta) = \exp(-E(\boldsymbol{v}, \boldsymbol{h}; \theta))/Z \tag{3-10}$$

where $Z = \sum_{\boldsymbol{v}} \sum_{\boldsymbol{h}} \exp(-E(\boldsymbol{v}, \boldsymbol{h}; \theta))$ is used for normalization. *E* denotes the energy function with the Bernoulli distribution that is calculated via:

$$E(v, h; \theta) = -\sum_{i=1}^{I} \sum_{j=1}^{J} {w_{ij}}^R v_i \, h_j - \sum_{i=1}^{I} b_i v_i - \sum_{j=1}^{J} a_j h_j \tag{3-11}$$

where b_i and a_j are the biases of the visible neuron and the hidden neuron respectively, $a = (a_1, a_2, \dots, a_J)$ and $b = (b_1, b_2, \dots, b_I)$, and θ is the parameter set of RBM given as $\{\mathrm{w}^R, \mathrm{b}, \mathrm{a}\}$. The weights can be learned as follows:

$${w_{ij}}^R = {w_{ij}}^R + \eta(\langle v_i h_j \rangle_{data} - \langle v_i h_j \rangle_{model}) \tag{3-12}$$

where $\langle v_i h_j \rangle_{data}$ and $\langle v_i h_j \rangle_{model}$ represent averages with respect to the distribution of training dataset and model, η is a learning rate (in this study, $\eta = 0.05$) Since a RBM is

represented by a bipartite graph, it is easy to get an unbiased sample of $\langle v_i h_j \rangle_{data}$. However, it is very difficult to compute $\langle v_i h_j \rangle_{model}$ and Gibbs sampling is used to approximate $\langle v_i h_j \rangle_{model}$ [54], the update of the biases is based on the iterative method(Hinton & Salakhutdinov, 2006). During the process of Gibbs sampling, the conditional probability distributions of visible neurons and hidden neurons are computed as follows:

$$\mathrm{p}(h_j|v;\theta) = f(\sum_{i=1}^{I} w_{ij} v_j + a_j) \tag{3-13}$$

$$\mathrm{p}(v_i|h;\theta) = f\left(\sum_{j=1}^{J} w_{ij} h_j + b_i\right) \tag{3-14}$$

where *f* is the activation function typically as the Sigmoid function. Since visible neurons and hidden neurons are binary, the corresponding values are usually determined by as follows:

$$h_j = \begin{cases} 1 \text{ if } p(h_j|v;\theta) \geq \varsigma \\ 0 \text{ if } p(h_j|v;\theta) < \varsigma \end{cases} \tag{3-15}$$

where ς is a threshold constant ranging from 0.5 to 1. The supervised training procedures proposed in the paper (Hinton & Salakhutdinov, 2006) are adopted to fine-tune the optimal weight matrixes based on the initial matrixes obtained by the unsupervised learning. As for other parameters of DBN structure including the number of stacked RBMs, a trial-and-error approach is adopted to find the optimal values for the best performance of DBN.

The physical CHF models discussed in this study usually are dependent on the extended surface ratio and the solid fraction that are latent variables while the DBN-based prediction framework can directly model the relation between CHF and geometrical parameters and keep the orthogonality between input targets of training datasets. It is evident that the

variables of input layer units are length (*L*), width (*W*) and thickness (*Th*) of the cuboidal heat transfer substrate, diameter, height, and spacing of the cylindrical micro-pillars, and CHF is the single output variable of perceptron. The training datasets are selected from the CHF databank complied in the Appendix based on the following screening criteria.

Table 3-2. Screening Criteria of Training CHF Datasets

Working Fluid			Heat Transfer Substrate			Micro pillar		
Pressure Condition	Type	Equilibrium Quality	Geometry Shape	Material	Orientation Angle	Material	Geometry Shape	Lattice Distribution
1 atm	Water	0.0	Cuboid	Silicon	0°	Silicon	Cylinder	Square

It is noteworthy that the trained DBN model for modelling CHF at the microstructured surface is supposed to converge to CHF at the plain surface if any of *d*,*h* and *s* approaches to zero, defined as zero convergence of DBN model. For an example of the microstructured silicon surface with specific dimension size, the corresponding CHF is dependent on *d*,*h* and *s*; the minimum CHF is obtained at the plain surface of $d^2 + h^2 + s^2 = 0$ but there should be six CHF cases $d^2 + h^2 + s^2 \neq 0$ that are equivalent to the plain surface incorporated into the DBN model, listed in **Table 3-3**.-1. In this study, the model convergence is bounded by using training datasets coupled with constraint CHF data points that are artificially derived from the minimum CHF datasets of various plain surfaces. **Table 3-3**.-2 shows 6 constraint CHF data points for the **#5** case equivalent to plain surface. As anticipated, prediction accuracy demonstrated by the coefficient of determination (R^2) increases as the number of training data increases (**Fig.3-4**), however, it should be noted in **Fig.3-4** that once the number of constraint data points is beyond 25, R^2 does not increase anymore and it maintains 0.9991. Therefore, the optimal number of constraint CHF data points is 25 and there are 150 artificially derived CHF data points that couple with the training datasets for completing model convergence.

Table 3-3. (-1) the variable values of *d*,*h* and *s* of 6 microstructured surfaces that are equivalent to the plain surface, (-2) the exemplary case of #5 deriving 6 constraint CHF data points from the silicon plain surface with dimension size of 15×10×0.5 mm^3

Table III. -1	#	*d* (μm)	*h* (μm)	*s* (μm)
	1	=0	=0	>0
	2	=0	>0	=0
	3	>0	=0	=0
	4	=0	>0	>0
	5	>0	>0	=0
	6	>0	=0	>0

Table III. -2	##	*d* (μm)	*h* (μm)	*s* (μm)	CHF (kW/m^2)
	1	20	1	0	1100
	2	40	8	0	1100
	3	60	16	0	1100
	4	80	24	0	1100
	5	100	32	0	1100
	6	120	40	0	1100

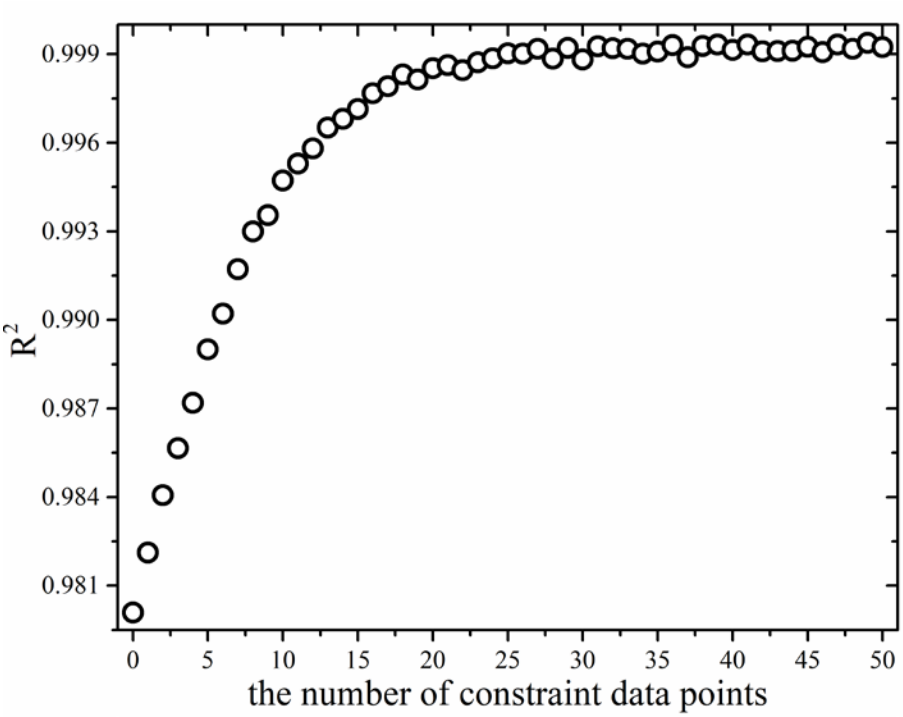

Fig.3-4 Prediction accuracy (R^2) change with the increasing number of constraint CHF data points, note that the equal numbers of constraint CHF data points are uniformly distributed respectively within the parametrical ranges of diameter, height and spacing in the training datasets.

3.5 Comparison of DBN with Other CHF Models

Apart from DBN, other machine learning techniques are also capable of modelling intricate and nonlinear relation patterns rooted in datasets, including ν- SVM, BPNN, RBFNN, and GRNN. To highlight the application superiority of DBN over SVM, BPNN, RBFNN and

GRNN, comparative experiments are performed in terms of prediction accuracy. The same training CHF datasets coupled with the same constraint CHF data points are used to train all five machine learning models whose structures parameters are optimized by the trial-and-error approach. To avoid the overfitting problem, the K-fold cross validation technique is adopted, the numerical experiments showed that K=5 can well help avoid the overfitting problem in all five machine learning models. There are 144 CHF points meeting the screening out criteria of **Table.3-2**. Two thirds of them are model training while the other one third are for testing. It is observed from Fig.3-5 that DBN has the best performance of CHF prediction for pool boiling intensified by micropillar structures compared with other 4 machine learning techniques.

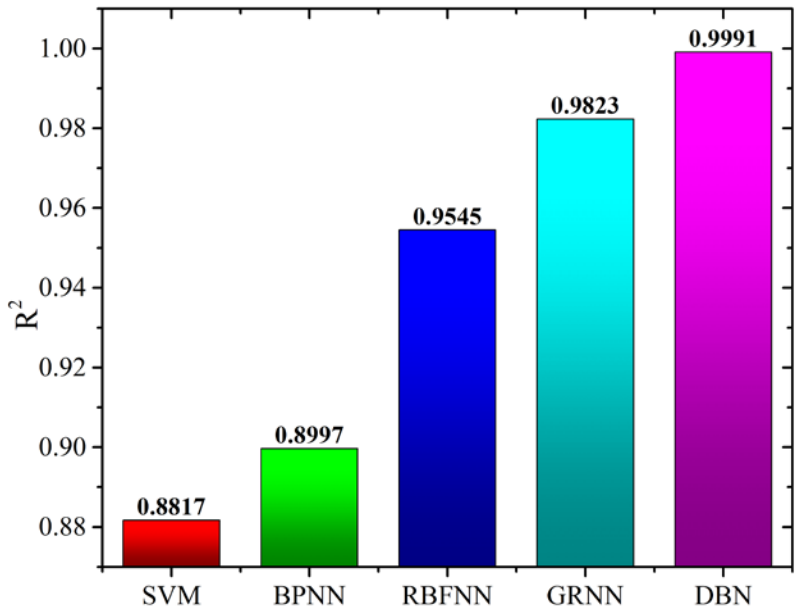

Fig.3-5 Prediction Accuracies of Different Machine Learning Techniques

As shown in Fig.3-6 (a), the CHF can be accurately predicted by DBN, though Fig.3-6 (b) demonstrates that GRNN can still capture the CHF profiles with respect *d*, *h* and *s* but more predicted CHF data points are further away from the line of true CHF when compared with that of DBN in Fig.3-6 (a). Noting that in Fig.3-6, true CHF denotes the experimental CHF

points collected from the published literatures. DBN holds better performance of CHF prediction than that of the other 4 machine learning techniques in pool boiling enhanced by microstructures. Since multiple complicated physical mechanisms behind CHF enhancement are convoluted together and therefore attributable to highly nonlinear parametric trends of CHF with respect to geometric parameters of micro-pillars, DBN is anticipated more suitable to model the CHF phenomena on micro-structured surfaces. DBN, one of deep learning models, can take advantage of training data samples to extract the high-level features and to learn the hierarchical representations by combining the low-level input more effectively for datasets with the characteristics of large variety and large veracity due to its two-stage training strategy with pre-training and fine-tuning. However, traditional training strategies of multi-layer neural networks and their network structures always result in a locally optimal solution or get trapped in overfitting or under-fitting problems. Those two factors contribute to the best CHF prediction performance of DBN model instead of the other 4 traditional machine learning methods. Compared with results of traditional physical CHF models in this first part of this study, the DBN-based method also presents a higher prediction accuracy because the DBN-based method because DBN-based method has a good agreement with the “zero-infinity” convergence.

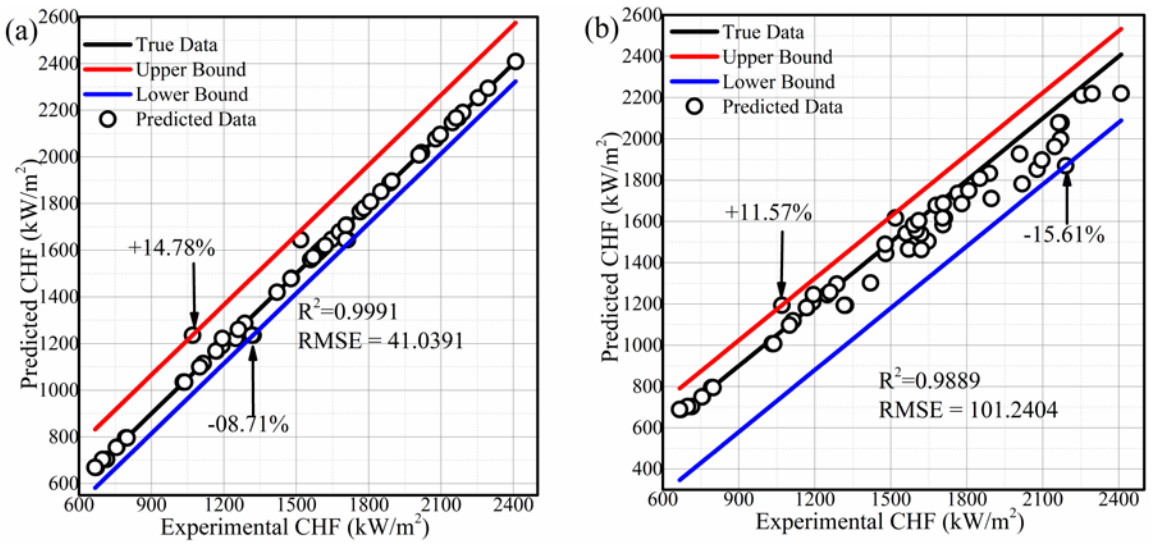

Fig.3-6 Comparison of Experimental and Predicted CHF: (a) DBN (b) GRNN

3.6 Parametrical Trends of CHF for Geometrical Parameters of Pin Fin Array

It is notable that the parametric trends of CHF with respect to geometrical parameters of microstructured surfaces – diameter, height and spacing – are rather complicated and highly nonlinear and in a good accordance with the zero-infinity convergence as shown in Fig.3-7, Fig.3-8 and Fig.3-9. If micropillars are relatively small, the CHF enhancement will be much limited due to pool boiling of tiny micropillars fabricated on the heat transfer surface approximately equivalent to that of the plain surface. If spacing is much greater than the diameter, there will be very few micropillars sparsely distributed on the surface, which results in thumbnail CHF enhancement. That explains the existence of the optimal spacing of micropillars in Fig. 3-8 and Fig.3-9. As pointed out by Lu et al.(M. C. Lu, Huang, Huang, & Chen, 2015b), CHF is inversely proportional to the total area of heat transfer surface. So the micro-pillars with larger diameter is assumed to lead to smaller CHF, elucidating the observed parametric trend of CHF with respect to diameter in Fig.3-

8 and Fig.3-9. Unlike the aforementioned diameter-variant and spacing-variant CHF behaviors characterized with single inflection points, the height-variant CHF behavior presents two peaks in Fig.3-8 which are contributed by two different competing mechanisms. On the one hand, the right peak results from the competing mechanism between the decreasing CHF induced by increasing heat transfer surface areas and the increasing CHF led by better fragmentation effect of increasing height on the subsequent vapor film; on the other hand, the left peak is the ultimate consequence of the competing balance between two distinct CHF triggering mechanisms: the bubble departure frequency is lowered by the increasing height of micropillars resulting in lower CHF and the fragmentation capability of height is improved by the increasing heights, helping to increase CHF. However, for height-variant CHF profiles in Fig.3-9, the competing mechanism between the extended surface area and the fragmentation capability of height dominates the CHF occurrence. In addition, other potential mechanisms about the effect of the pillar height, such as the bubble entrapment and coalescence, also generally affect the CHF enhancement. However, it should be noted that dimensional sizes of heat transfer substrate have influential impacts on how micro-pillar array affects CHF. As demonstrated in Fig.3-8 and Fig.3-9, the parametrical trends of CHF present different behaviors on different sizes of heat transfer substrates possibly because of the different total numbers of pin fins fabricated on surfaces, and it is observed that a specific micro-pillar array has better CHF enhancement on heat transfer surfaces with larger areas due to more pin fins.

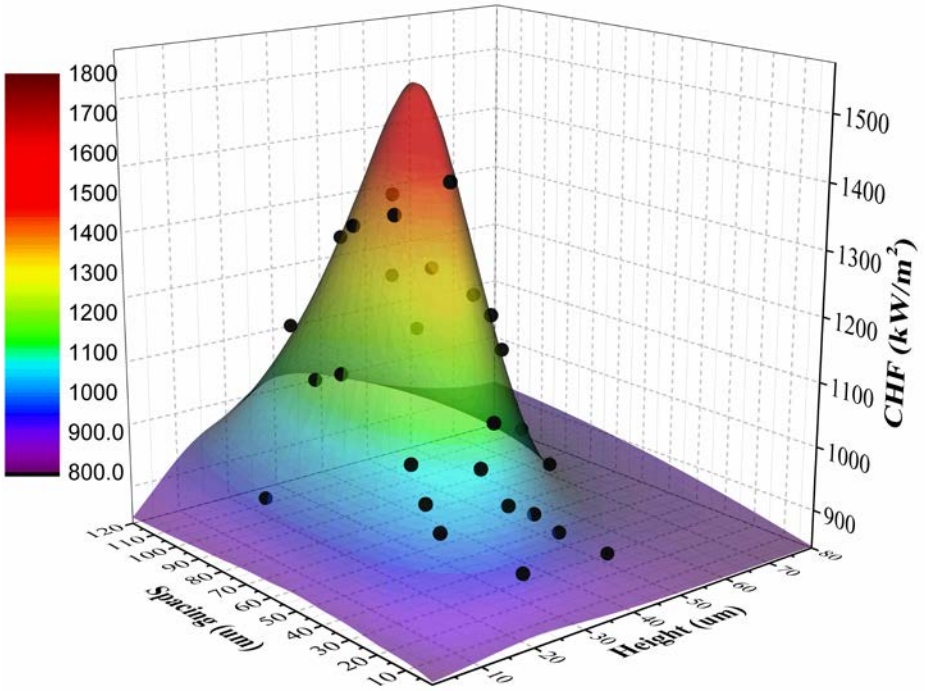

Fig.3-7 CHF profile in terms of height and spacing of micropillar fin (diameter = 30 um)

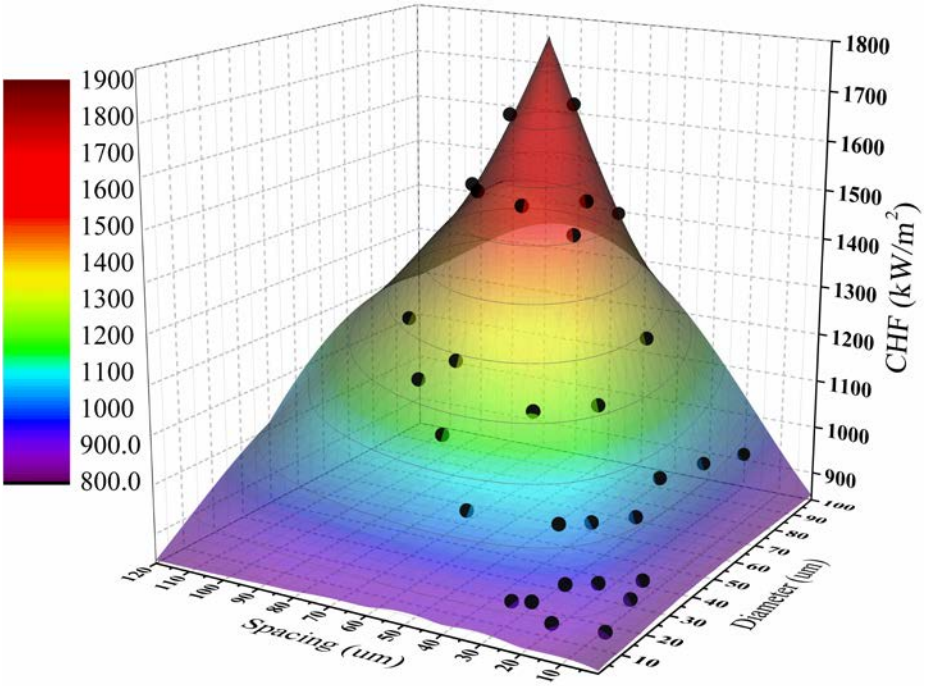

Fig.3-8 CHF profile in terms of diameter and spacing of micropillar fin (height = 20 um)

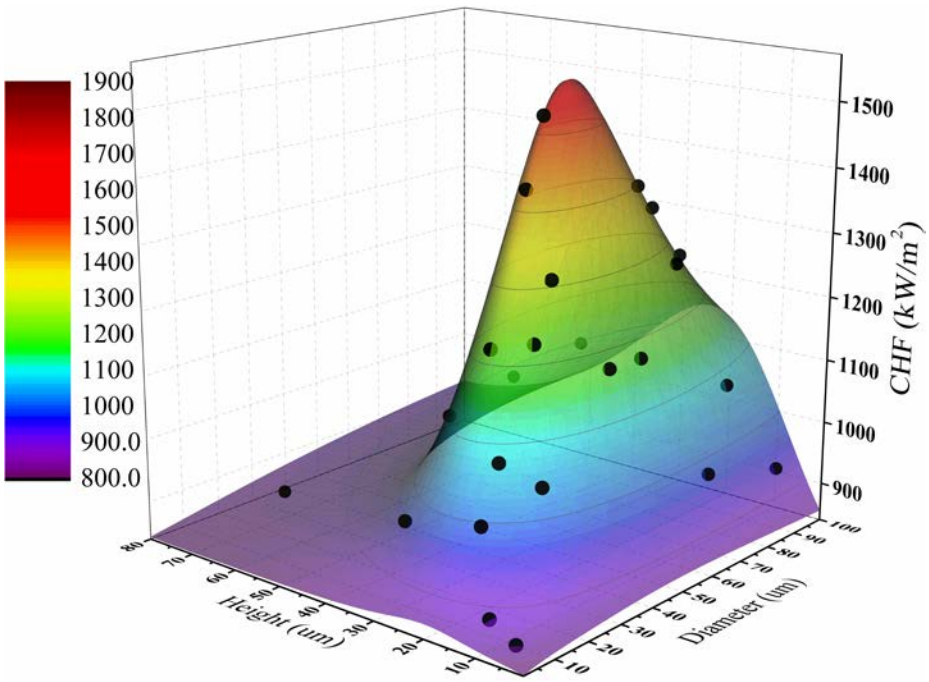

Fig.3-9 CHF profile in terms of diameter and height of micropillar fin (spacing = 30 um)

3.7 Summaries of Chapter 3

This chapter reviews experiments, which are performed for pool boiling CHF enhanced by microstructured surfaces, and compiles a microstructure-enhanced pool boiling CHF databank, thereby supporting further experimental explorations in the untouched regions of microstructure-enhanced pool boiling and the development of more accurate models. Through qualitative analyses for the effects of structured surfaces on CHF, the potential parametrical trends of CHF are elucidated with respect to geometrical parameters of pillar. Based on the complied experiment CHF datasets of saturated water pool boiling on silicon-microstructured surfaces, four current CHF models are evaluated for their prediction performances in terms of coefficient of determinant. The results demonstrate that: the least optimal prediction accuracy is achieved by the hydrodynamics based models in (Nguyen et al., 2018; Rahman et al., 2014), of which measurements of wicked volume flux and rewetting velocity of liquid inflow are estimated by physical models, but these two models

only utilizing measured parameters are capable of accurate CHF prediction; the capillary wicking models of Kim et al.(B. S. Kim, Lee, et al., 2014) and Li et al. (R. Li & Huang, 2017) give higher prediction accuracy compared to that of the model proposed by Chu et al.(K. Chu et al., 2013). Then a term, zero-infinity convergence, is introduced for discussing parametrical trends of CHF depicted in two models of Kim et al.(B. S. Kim, Lee, et al., 2014) and Li et al. (R. Li & Huang, 2017).

Motivated by the drawbacks of physical CHF models, the deep belief network is proposed to predict CHF of microstructure enhanced pool boiling. The proposed CHF model based on deep belief network has the best performance of prediction accuracy and shows a good agreement with the zero-infinity convergence. Different from the training process of other regression models, the microstructure-enhanced CHF model of deep belief network is supposed to be trained by CHF training datasets coupled with constrained CHF data points, which are manually derived from raw CHF training datasets for zero-infinity convergence at the CHF of the plain silicon surface. This new technique not only guarantees accurate parametric trends of CHF with respect to geometrical parameters of micropillars, but also helps improve the prediction accuracy of the deep belief network model. More importantly, the introduction of zero-infinity convergence and the proposal of constrained training datasets can provide a new solution to the similar constrained machine learning problems. Due to its excellent regression capability in capturing complex and nonlinear trends of microstructure-enhanced saturated water pool boiling CHF, deep belief network exhibits much better performance of CHF predictions than other traditional neural networks. Through studying parametric trends of CHF with respect to geometric parameters of

cylindrical micro-pillar array, it reveals that the effect of height on CHF is more complicated than that of diameter and spacing. And besides the total number of pillars fabricated on the surface has influential impacts of the parametric trends of CHF. The DBN-based CHF model is a data-driven method that will becomes more accurate and robust in modelling as the accumulation of microstructure enhanced CHF experimental datasets. Last but not least, this paper provides a guideline about how to borrow machine learning frameworks for resolving the complex problems and helping interoperate the physical mechanisms in boiling heat transfer.

4 STUDY OF EFFECTS OF HEATER DIMENSIONS AND MATERIALS BY MACHINE LEARNING

4.1 Impacts of Thermal Properties of Heater Materials on CHF

The difference of boiling curves among various families of heater materials, such as stainless steel, copper, aluminum, zircaloy, silicon and silica, reveals variations in the thermal physical properties of boiling surface materials. Those property variations among heater materials bring significant disparities in terms of CHF, HTC and ONB. For example, in the CHF experiments of pool boiling conducted by Raghupathi and Kandlikar (Raghupathi & Kandlikar, 2018), CHF difference could reach 383.8 kW/m^2 for water boiling on different materials with same dimensions. Tachibana et al (TACHIBANA, AKIYAMA, & KAWAMURA, 1967) suggested that in the CHF model, the thermal properties of boiling surface materials should be incorporated to account for predicted CHF variations based on hydrodynamic based models. Guglielmini and Nannei (Guglielmini & Nannei, 1976) firstly adopted the squared product of thermal conductivity, density and specific heat capacity, namely thermal effusivity, to correlate the effects of thermal physical properties on CHF. Besides, they also found that CHF was asymmetrically dependent on the thickness of heat transfer substrate and gave the empirical expression of the asymptotic thickness in terms of thermal effusivity only. To better optimize the relation between thermal properties of heater materials and CHF, Saylor (Saylor, 1989) suggested the product of the heater thickness and thermal effusivity, namely thermal activity, as the control variable in the asymptotic correlation of CHF. Based on FC-72 CHF experiments performed on different materials with a set of different thicknesses, Golobi and Bergles proposed a new asymptotic CHF correlation and a piece-wise empirical expression of the

asymptotic thickness (Iztok Golobič & Bergles, 1997). Arik and Bar-Cohen compared different asymptotic CHF correlations and thought that the thermal activity was the best parameter for the optimal CHF correlation (Arik & Bar-cohen, 2006). Although several empirical correlations have been proposed to predict CHF within 12.5% deviation, the satisfactory analytical basis had not been found yet. However, the Kandlikar CHF model partially explained the effects of heater materials on CHF from the physics perspective of wettability (Kandlikar, 2001b). Besides wettability, nucleation site density and wickability are also traditionally accepted to have impacts on CHF. It is widely believed that CHF decreases with increasing nucleation site density (K. Wang, Gong, Bai, & Ma, 2017) while improved wettability and wickability can be the major cause of CHF enhancement (Moon et al., 2016; Rahman et al., 2014). Therefore, it is extremely difficult to theoretical model the effects of heater materials on CHF based on thermal physical-chemical properties of materials. Moreover, those properties of materials actually are dependent on the saturation temperatures of working fluids. It should be noted that there is considerable uncertainty about these aforementioned parameters due to the limited data and generally large data scatter.

4.2 Effects of Heater Dimensions on CHF

It is widely agreed that the dimensions of heat transfer substrates have impacts on CHF. The mechanisms causing the dimensional effects, however, still remain undetermined (Gogonin & Kutateladze, 1977; Henry, Kim, Chamberlain, & Hartman, 2005; Kwark, Amaya, Kumar, Moreno, & You, 2010; Juno Lee & Chang, 2012; J. Lienhard & Dhir, 1972; M.-C. Lu, Chen, Srinivasan, Carey, & Majumdar, 2011; M. C. Lu et al., 2015a; K.-

A. Park & Bergles, 1988; Rainey & You, 2001). Several explanations are proposed by various researchers to elaborate how dimensions affect CHF. For instance, the heater size effects were attributed to the smaller flow resistance on small-sized heaters (Kwark et al., 2010; Rainey & You, 2001) but the total number of vapor columns was reduced on smaller heaters in the CHF model of Lienhard and Dhir (J. H. Lienhard & Dhir, 1973b); however, the assumption of Lienhard and Dhir (J. H. Lienhard & Dhir, 1973b) was overridden by the experimental results, which demonstrated that there was just one single vapor column/mushroom was present on their small plate heaters (M.-C. Lu et al., 2011; M. C. Lu et al., 2015a). Lu et al (M.-C. Lu et al., 2011) speculated that the actual Helmholtz wavelength might be affected by the size of the heater and the Helmholtz wavelength was directly related with the rewetting velocity of liquid to the hot spots on the surface. However, Bar-Cohen and McNeil (Bar-Cohen & McNeil, 1992) attributed the effect of heater size on CHF to the transient conduction ability of the heater. On the other hand, the systematic experimental study performed by Gogonin and Kutateladze (Gogonin & Kutateladze, 1977) had shown that the effect of heater sizer on CHF would be absent if the non-dimensional heater size is beyond a certain critical point (the non-dimensional heater size is the ratio of heater length to the capillary length of working fluid). But this critical point varied in different reported experiments. It should be addressed that geometrical shapes of heater surface also mattered to CHF (Henry & Kim, 2005; Henry et al., 2005; Kam, Choi, & Jeong, 2018; S. B. J. Kim et al., 2003; S. H. Yang, Baek, & Chang, 1997). Based on the experimental results from the paper (Kam et al., 2018), it was found that CHF decreases as the area aspect ratio approaches to 1. The plausible explanation was how the following case occurred, assuming that the length of heater is much greater than the

width of heater, meaning the area aspect ratio is close to zero, bubble coalescence will occur only along the length, if the length is approximate to the width, denoting that the area aspect ratio is 1, the bubble coalescence will take place around all directions, which increases the possibility of local dry spot formation. CHF of a bare square copper plate is 1027 kW/m^2 (Kam et al., 2018) while CHF of a bare circular copper disk is 793.6 kW/m^2 (Ha & Graham, 2017) although both heaters have the same volume and operation conditions. As a matter of fact, the Hydrodynamic based CHF model correlated the effect of heater size by assuming that CHF was proportional to the number of bubbles present in the surface and inversely proportional to the total surface area of heater (M. C. Lu et al., 2015a). In this regard, CHF obtained on finitely big surfaces is proportional to the reciprocal of side length squared for square heaters. However, in the empirical correlations proposed by Bar-Cohen and McNeil (Bar-Cohen & McNeil, 1992), and Saylor (Saylor, 1989), CHF decreases linearly with the increasing of heater side length. Nevertheless, theoretical models or empirical correlations have not been reported to account for the effect of geometrical shapes of heaters on CHF so far.

4.3 Machine Learning Based Study for Effects of Heaters on CHF

The dedicated selection of the input parameters could help enhance the prediction accuracy of machine learning framework and provide an insightful understanding of modelling physical problems (Yadav, Malik, & Chandel, 2014). On the other hand, selecting the relevant input parameters can help reduce the number of input parameters and computational resources (Goodfellow, McDaniel, & Papernot, 2018). Because of limited CHF experiments that are involved with rectangular surface plates, the experimental CHF

data points that are obtained on square heaters are collected from tremendous various publications to investigate how the side length and thermal properties of heaters exert impacts on CHF. Training data preparation also matters to the regression accuracy and the reliability of predicted results. The criteria of training data selections are listed in Table 4-1. In the GRNN framework of this study, the input parameters to GRNN are side length, thermal activity and thermal diffusivity of boiling heated plates. Although thermal activity accounts for the thermal properties of boiling surface materials, the experimental CHF results from the paper (Ho et al., 2016) show that FC-72 CHF of saturated pool boiling on Al-6061 and $AlSi_{10}Mg$ surfaces are much higher than the CHF correlated by methods in the paper (Arik & Bar-cohen, 2006). However, thermal activities of these two materials are less than that of the stainless steel, which should result in lower than CHF on these two plates compared with that of stainless steel according to the correlations discussed by Airk and Bar-Cohen (Arik & Bar-cohen, 2006). It is pointed out by Seo et al (Arik & Bar-cohen, 2006) that thermal activity and thermal diffusivity are considered to be factors enhancing CHF and activating nucleation sites. The thermal activity speaks for the capacity of heat transfer surface dissipating heat from a local region to adjacent regions, thus further prohibiting an overshoot of wall superheat (J. M. Kim, Kong, Lee, Wongwises, & Ahn, 2018). Also thermal activity indicates thermal energy conductance through the tangential direction of the surface. The higher thermal activity could inhibit the development of local hot spots into irreversible dry spots, thus delaying the occurrence of CHF during the nucleate boiling near the CHF point (M. H. Lee, Heo, & Bang, 2018). The higher thermal activity, the more effectively the heat can be dissipated from the hot/dry spots. On the other hand, thermal diffusivity quantifies the heat transfer rate of boiling surface materials from

the hot side to the cold side. Besides thermal diffusivity somehow might have influence on the thermal readjustment time from the high local temperature to the low local temperature because of the rewetting liquids (Staszel & Yarin, 2018).

Table 4-1 The selection criteria of training datasets for the GRNN framework of this study

Shape	Surface Inclination	Boiling State	Pressure	Fluid	Boiling Type
Square	Horizontal-FacingUpward	Saturation	101.325 kPa	Water	Pool Boiling

GRNN, which was firstly proposed by Specht (Specht, 1991), has been successfully and extensively developed and studied by researchers. GRNN is an exemplary illustration with high adaptability as well as a better prediction accuracy. GRNN is a kind of feed-forward neural network and the model is based on the mechanism of nonlinear regression(Song, Romero, Yao, & He, 2016). As shown in Fig. 4-1, GRNN is composed of four neural layers, the input layer, the pattern layer, the summation layer and the output layer (Chelgani & Jorjani, 2011). First, data is given to the input layer and the number of input parameters should be equal to the neurons of the input layer. Then, data is fed into the pattern layer by the neurons of the input layer. The pattern layer's output is then given to the summation layer which has two kinds of neurons (Ni & Li, 2016).

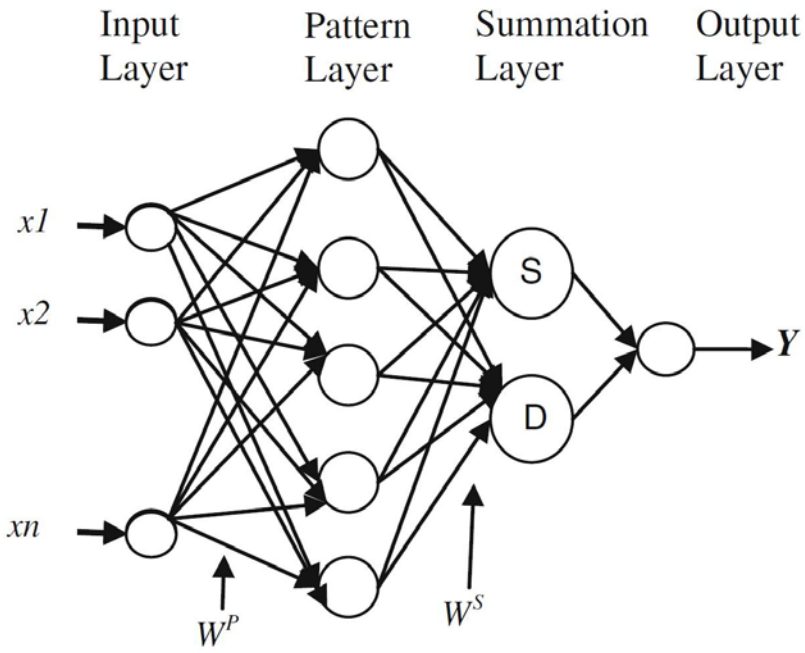

Fig.4-1 Schematic Diagram of GRNN

Finally, the summation layer's data is delivered to the output layer. The equation of GRNN can be summarized as (Rooki, 2016)

$$E[y|x] = \frac{\sum_{i=1}^{n} y_i \exp(-\frac{(x-x_i)^2}{2\sigma^2})}{\sum_{i=1}^{n} \exp(-\frac{(x-x_i)^2}{2\sigma^2})} \quad (4\text{-}1)$$

where σ denotes the spread parameter, y_i is the predicted output, x_i is the input parameter and $E[y|x]$ is the expected output value. GRNN possesses only one variable σ, which is highly crucial in the GRNN model (Giri Nandagopal & Selvaraju, 2016) and can be decided by some trial and error methods. More specifically, the generalization performance of GRNN is decided by the parameter σ (Bendu, Deepak, & Murugan, 2016).

4.4 Results Analyses and Discussions

Although DBN discussed before might yiled a little better modelling accuracy than GRNN for regressional analyses of heater materials and dimensions, GRNN can speed up the training process, which helps the network to be trained faster and reduces computional time loads. Unlike other artifical neural networks, such as mulitiple feedforward network, radial

neural network and back propagation neural network, GRNN estimation is always able to converge to a global solution and won't be trapped by a local minimum. In the training process of GRNN, the split-sample cross validation is adopted to find the spread parameter σ (Schenker & Agarwal, 1996). 84 experimental CHF data points of saturated water pool boiling are collected from published literatures based on the data screening criteria of Table 4-1. 34 data points were selected out as for testing data sets while the other 50 data points are utilized to train the GRNN model. The predicted results of testing datasets are shown in Fig. 4-2, showing the predicted results in a good agreement with experimental results. Based on the trained framework of GRNN, the model produced the parametrical trend curves of CHF with respect to increasing thermal activity in terms of different materials and dimensions, as shown in Fig.4-3. The predicted results are benchmarked with the empirical correlation proposed by Golobic and Bergles (Iztok Golobič & Bergles, 1997), and expressed as follows:

$$\frac{q_{CHF}^{"}}{q_{CHF,asy}^{"}} = 1 - \exp\left(-\left(\frac{S}{2.44}\right)^{0.8498} - \left(\frac{S}{2.44}\right)^{0.0580}\right) \quad (4\text{-}2)$$

where S is the thermal activity, $q_{CHF}^{"}$ is the corrected CHF for experimental results that are obtained on boiling surfaces of different materials and $q_{CHF,asy}^{"}$ is the asymptotic CHF value that is usually determined by fitting experimental results with Eq.4-2.

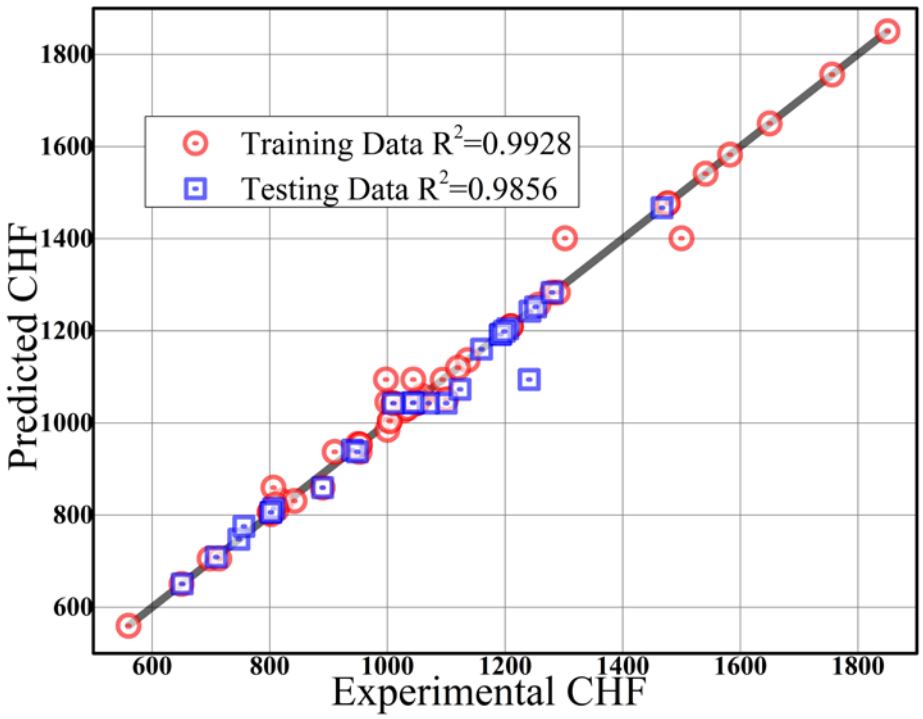

Fig.4-2 the experimental CHF VS Predicted CHF of GRNN

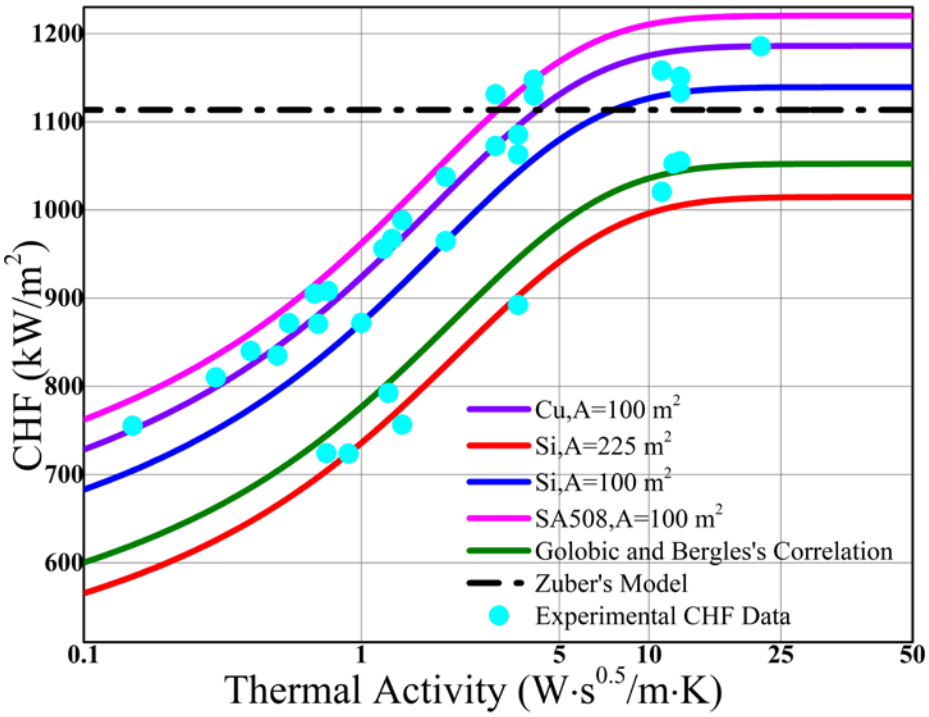

Fig.4-3 the parametrical trend of CHF with respect to thermal activity

It is observed that CHF is often underestimated by the correlation of Eq.4-2. Fig.4-3 also demonstrated that the parametrical trend predicted by the trained GRNN presents similar

behaviors to that of the empirical correlation proposed by Golobic and Bergles (Iztok Golobič & Bergles, 1997). But it is notified that there are two obvious result differences between GRNN and the empirical correlation, the one is that the boiling surface has impacts on CHF and the other is that the GRNN model that also accounts for the thermal diffusivity gives better CHF prediction than the empirical correlation does. Because the thermal activity is not capable of fully representing the thermal properties of boiling surface materials. Therefore, it is reasonable to postulate that there should be another correlation factor on the top of Eq.4-2, only depending on thermal diffusivity and the surface area. There would be another possible cause resulting in CHF difference between various materials, the wettability. The static contact angle of polished silicon is 89°, 70° for copper surface and ~17° for SA508 (Barisik & Beskok, 2013). If the static contact angle is closer to 0, the higher wettability the boiling surface will have, thus promoting CHF. Otherwise, CHF will be degraded on the hydrophobic surfaces. Besides, in terms of thermal diffusivity of material, SA508 is greater than copper while copper is also greater than silicon. In this regard, when applying the same heat flux to those surfaces made of SA508, copper and silicon, then the average wall superheat on the SA508 surface will be anticipated the lowest, hence augmenting the CHF.

The trained GRNN framework renders the parametrical trend of CHF with respect to increasing side length of heater in Fig. 4-4. It is observed from Fig.4-4 that CHF will be independent on the side length once the side length exceeds 15 mm. This critical side length is roughly 5.94 times greater than the capillary length of saturated water 2.5256 mm. However, in the literatures (M.-C. Lu et al., 2011; M. C. Lu et al., 2015a; You et al., 2003),

when the side length is more than or equal to 5 times of capillary length of working fluid, then working fluid can be considered boiling on infinite surface area and CHF can be predicted by Zuber's Model. It is noticeable that in Fig.4-4 there is an optimal side length allowing CHF to reach the maximum value, which is, however, decided by the thermal activity and other parameters of boiling surface materials. Those peaks indicate that there exist two mutually competing mechanisms, the one is for enhancement and the other is for degradation. It was argued by Rainey and You that a significant portion of the heater is rewetted from the edges of the heater for smaller heaters, which has a smaller flow resistance compared with larger heaters due to the supply liquid rewetting the surface from the downward vertical flow on larger heaters, resulting in a higher CHF (Rainey & You, 2001). On the other hand, Kim et al (E. S. Kim, Jung, & Kang, 2013) found that the increase of CHF is proportional to the effective boiling surface area that is dependent on the total number of vapor mushrooms present on the surface and the bubbled departure frequency. The number of vapor mushrooms increases with the increasing surface area. Besides as surface area increases, the rewetting liquid supply transits from the sides to above, which boosts the upraising speed of bubbles and improves the departure frequency of bubbles, thus delays the occurrence of local dry spots and enhances CHF.

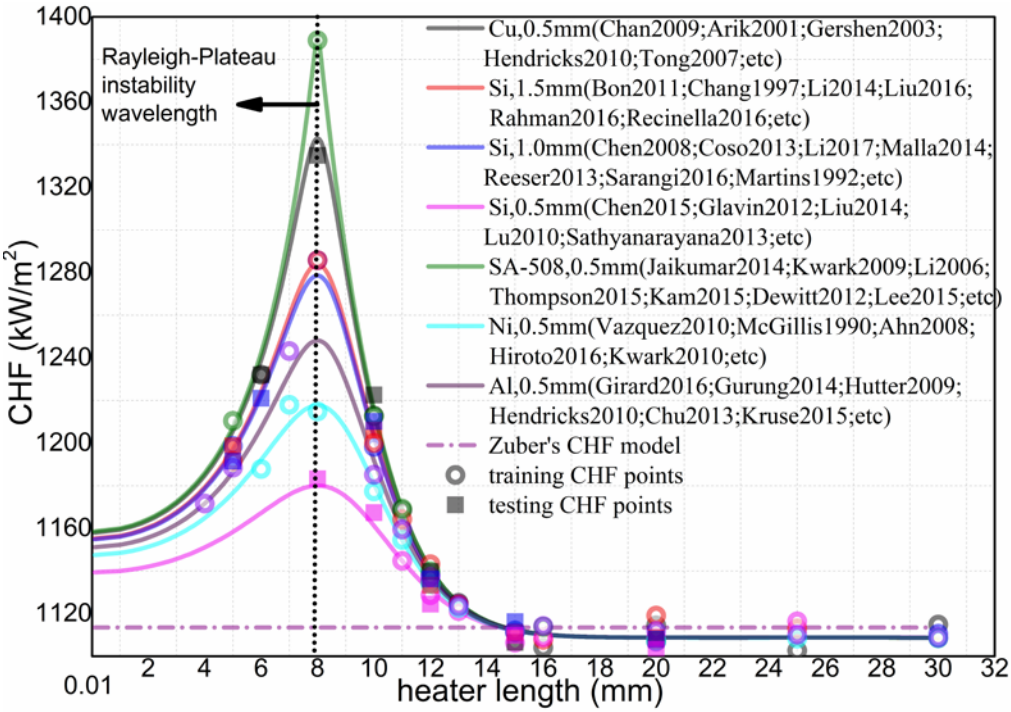

Fig.4-4 the parametrical trend of CHF against the increasing side length of square heater

It is found that the critical heater length is independent on the thermal properties of boiling surface material and is equal to the Rayleigh-Plateau instability wavelength $\lambda_R = \pi\sqrt{\sigma/g\Delta\rho}$. According to the hydrodynamics theory, the instability growth rate is related with the characteristic length of surface (Abarzhi, 2010; Abarzhi & Rosner, 2010). Guan et al (Guan, Klausner, & Mei, 2011) assumed that the kinetic behaviors of the liquid macro layer that is underneath the vapor mushroom could be described by the Rayleigh–Taylor instability wave. Based on viscous potential flow analysis, the linear stability analysis for a small disturbance results in the following dispersion relation (de Gennes, Francoise, Brochard-Wyart, & Quere, 2004; B. J. Kim, Lee, & Kim, 2016; B. S. Kim, Lee, et al., 2014; S. H. Kim, Lee, et al., 2015b),

$$\omega = \sqrt{\frac{\Delta\rho g\lambda - \sigma\lambda^3}{\rho_1 \coth(\lambda\delta_1) + \rho_2 \coth(\lambda\delta_2)}} + \frac{\sigma\delta_2^3}{3\mu L^2}\left(3L^2\lambda - \frac{\lambda^3}{12}\right)\mathrm{i} \qquad (4\text{-}3)$$

where ω , λ, ρ, δ, σ, μ , L, and g are the growth rate, wave length, fluid density, fluid layer thickness, surface tension, liquid viscosity, characteristic length of surface and gravitational acceleration, respectively.

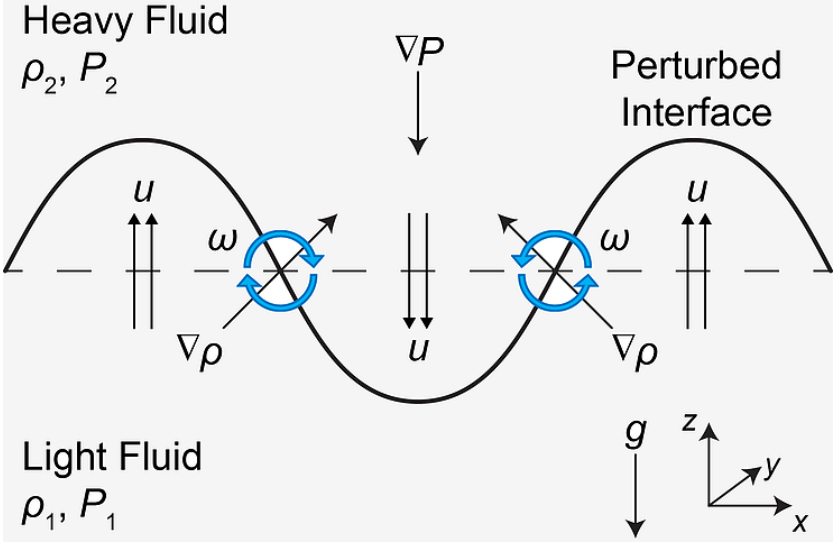

Fig. 4-5 Schematic demonstration of the Rayleigh–Taylor instability at a perturbed interface separating two liquids of different densities. Here, ω is the perturbation growth rate, u is the velocity of liquid, ρ is the density and g is the gravity factor (Alkhadra, 2017).

In Eq.4-3, the real component depicts the instability growth rate along the horizontal direction while the complex component speaks for the growth rate along the vertical direction. And the coth is the hyperbolic cosine function. In this study, light fluid is the vapor of working coolant while heavy fluid is the liquid of working coolant. Here the liquid macrolayer thickness recommended by Rajvanshi et al (Rajvanshi, Saini, & Prakash, 1992) is adopted to replace δ_2 while the thickness of the vapor film δ_1 is estimated by the predictive method proposed by Dasgupta et al (Dasgupta, Chandraker, Nayak, & Vijayan, 2015). The occurrence of the most rapid growth rate leads to$d\omega/d\lambda = 0$, as a result, $\lambda_c = 2\pi\sqrt{3\sigma/\Delta\rho g}$, $L = \pi\sqrt{\sigma/\Delta\rho g}$. The perturbation growth rate is of importance because it indicates how fast the wavy interface oscillates. Besides the bubble departure frequency is determined by rapid growth rate (B. J. Kim, Lee, & Kim, 2015; B. J. Kim et al., 2016).

The bubble departure frequency increases over the increasing growth rate of perturbation (Cole, n.d.) while Kim et al. (D. E. Kim et al., 2015) proposed an analytical relation between CHF and the bubble departure frequency, demonstrating that CHF linearly increases with the increasing departure frequency of bubbles.

4.5 Summaries of Chapter 4

This chapter reviews how dimensional sizes and materials of heaters affect CHF based on available mechanistic explanations and experimental results. Based on the aforementioned discussions, the thermal activity, which is proposed by Saylor (Saylor, 1989), cannot alone sufficiently correlate the effects of thermal properties of materials on CHF. In order to capture how thermal properties of boiling surface materials have influence on CHF, thermal activity and thermal diffusivity are investigated to better correlate the effects of thermal properties of materials on CHF and represent four primitive parameters of heater materials, including, thickness, density, specific heat capacity and thermal conductivity. In virtue of GRNN regression framework, the parametrical trends of CHF are studied with respect to the thermal activity and dimensional sizes. The numerical results demonstrated that the trained GRNN framework yields better predicted results than the empirical correlation. Although the GRNN showed similar parametrical trends of CHF to that of the empirical correlation with respect to thermal activity, the parametrical studies towards the effect of heater sizes on CHF are way different in the trained model of GRNN compared with that of empirical correlations. Besides the numerical results also demonstrated that there was an optimal heater size that allows CHF to reach the maximum point. This optimal

heater size is exactly equal to the Raleigh-Plateau instability wavelength, and the physical rational behind this phenomenon is also analyzed based on the hydrodynamics theory.

5 CHF LOOKUP TABLE RECONSTRUCTION

Noting that the primary contents of Chapter 5 was adopted from the journal paper(He & Lee, 2018) written by the author and his advisor.

5.1 Current Status of CHF Lookup Table Reconstruction

CHF sets the limits to the maximum heat flux of nuclear fuel rods and thus determines the attainable maximum thermal power in the steady-state of PWR operation. In order to sufficiently marginalize to CHF, nuclear regulation committee addresses the compliance with the safety factor, that is, Departure from Nucleate Boiling Ratio (DNBR) - the ratio of CHF to the actual local heat flux. CHF is a complicated phenomenon influenced by various factors and parameters such as mass flow rate, system pressure, equilibrium quality, fuel bundle geometry and surface characteristics of cladding materials (Bruder, Bloch, & Sattelmayer, 2017). The empirical CHF correlation models and relevant CHF lookup tables are widely used in the thermal hydraulics system codes, such as REALP5-3D, TRACE and etc.

The high experimental costs that are in association with the CHF investigation developments and primarily from high pressure pumping tests prohibits numerous experimental CHF studies from their applications to aforementioned thermal hydraulics

system codes. This situation has been even more obvious in the recent developments and studies of Accident Tolerant Fuel (ATF) cladding (Brown, Ludewig, Aronson, Raitses, & Todosow, 2013; Y. Lee & Kazimi, 2015; Y. Lee, McKrell, Yue, & Kazimi, 2013; Y. Lee, NO, & Lee, 2017). Past studies and investigations that demonstrated the impact of the material surfaces on nucleate boiling (G. H. Seo, Jeun, & Kim, 2015, 2016) make the community of nuclear engineering think that CHF of ATF cladding materials is more likely to be way distinct from CHF of metal alloys of Zirconium family, or steel materials used for the W-3 correlation or look-up table (Bruder et al., 2017). The high cost of associated CHF experiments measurements covered a wide range of operating conditions, which gives us motivations to find a new technology to effectively inter/extrapolate experimentally measured CHF data points. Based on this inter/extrapolation techniques, we can setup a modeling foundation upon which CHF look-up tables construction can be expedited to apply the usage of experimentally measured CHF points to the thermalhydraulic codes and nuclear reactor licensing.

Remarkably, the parametric profiles of CHF are relatively simple, despite the complex phenomena subjected to dominant operating conditions – pressure (P), equilibrium quality (X_e), and mass flux (G). CHF monotonically decreases, and increases with increasing X_e, and G, respectively (Fig. 5-1(a), and (b)). The pressure sensitivity of CHF can be parameterized by a simple function that gives a local maximum value at a certain pressure (Fig.5-1(c)).

The straightforward parametric profiles of CHF with respect to the three primary parameters of subcooled flow conditions (X_e, G, and P) imply that CHF look up tables can

be efficiently constructed if an enabling machine learning method is applied with a suitable set of training dataset.

5.2 ν-SVM Aided CHF Prediction with Sparingly Distributed CHF Data Points

SVM is able to determine its model size and obtain the globally optimal and unique solution in an automatic manner with contrasting to ANN. In Cai's study (Jiejin Cai, 2012a, 2012b), ε-SVM was adopted to find the correlation of the tube geometry parameters and the physical properties of liquids with Kutateladze number. Its comparative analysis with experimental results showed that ε-SVM gave a better prediction accuracy than different ANNs. Past investigation of CHF prediction modelled by ν-SVM (Jiang, Ren, Hu, & Zhao, 2013; Jiang & Zhao, 2013b, 2013a) showed that CHF profiles with respect to the aforementioned parameters of subcooled flow boiling, mass flux, pressure and quality (G, P, and X_e) can be well and accurately predicted by ν-SVM. The numerical investigation performed by Jiang and Zhao (Jiang & Zhao, 2013b) improved its model prediction accuracy by finding global optimal coefficients of ν-SVM in the virtue of particle swarm optimization techniques, with which dryout CHF was predicted by adopting the CHF look-up tables prepared by Groeneveld et al.(Groeneveld et al., 2007) and Kim et al.(H. C. Kim, Baek, & Chang, 2000). These numerical experimentations with concentration on how ν-SVM models CHF with more than three parameters, showed that ν-SVM has evident superiority of CHF prediction when compared with other different machine learning algorithms, such as radial basis function network (Jiang & Zhao, 2013a). It is interesting that during their training datasets preparation (Jiang et al., 2013; Jiang & Zhao, 2013b), seventy-five percent of the total CHF data collection were used as training datasets for

support vector machine in a manner of the subtractive clustering scheme. That is, twenty-five percent of the CHF dataset are used for the evaluation of prediction performance. Bearing this in consideration, the SVM was essentially used and applied to enable inter/extrapolation method for the CHF data points of a close distribution.

Practically speaking, it would be best to realize the SVM application to CHF prediction if the training data sets successfully capture CHF parametrical behavior on the basis of sparingly distributed experimental data. This could strongly suggest that the CHF look-up tabulation for different cladding materials including ATF claddings like SiC and FeAlCr, can be achieved only with the limited number of experimental CHF data points, which by that expedites system-levelly the simulation of ATF claddings. Additionally, with the support of SVM, extrapolation of CHF data beyond the experimental conditions could help reduce the experimental costs of CHF procurement. Accordingly, in this study, the goal is to model CHF behaviors with respect to three primary parameters of subcooled flow boiling and explore strategies for the data-driven CHF look-up table construction with ν-SVM, based on sparingly distributed experimental data points. Additionally, its potential application to the CHF extrapolation beyond the experiments is investigated in this paper.

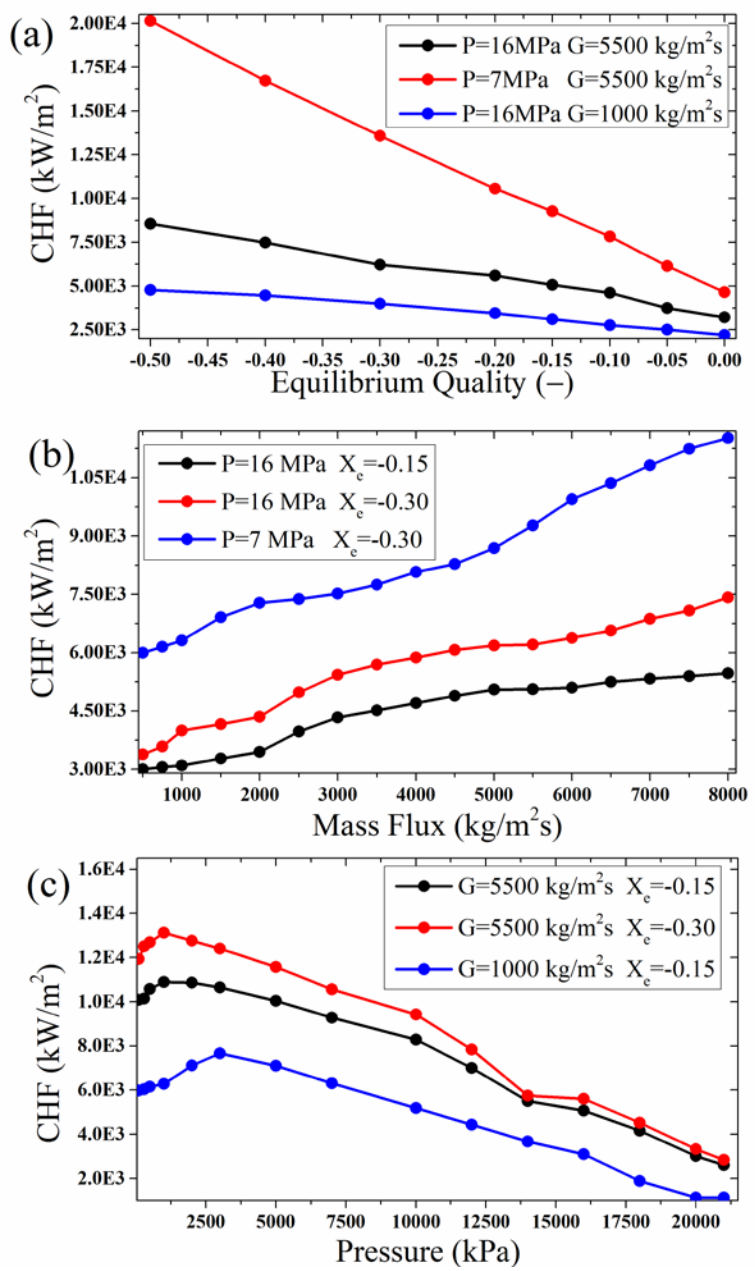

Fig.5-1 The parametric trends of CHF in subcooled flow with respect to (a) equilibrium quality (*Xe*), (b) mass flux (*G*), and (c) pressure (*P*)

The CHF look-up table of Groeneveld et al (Groeneveld et al., 2007) is used as the reference CHF data bank in this study. The Groeneveld (2007) look-up table is a commonly applicable data bank that is incorporated in major system-level codes. Thus, any prediction results and conclusions explored in this study can be readily and reasonably used to the

system-level codes of thermal hydraulics (i.e., *RELAP-5 3D*, or *COBRA-TF*). In this data bank of 2007 CHF data, CHF under the subcooled flow ($X_e < 0$) is selected to study for the PWR steady-state conditions.

5.3 The Proposed Method: CHF Lookup Table Construction by ν-SVM

In this study, ν-SVM is adopted to reconstruct CHF lookup tables based on experimental CHF data (training dataset) in accordance with the consequent methodologies and procedures. Given a set of CHF data point under a specific equilibrium quality (x_e), the relation between x_i and y_i can be modelled by using ν-SVM, where x_i is the input vector of (P_i, G_i) and y_i is the output data of CHF value ($i = 1,2, \dots, N$, N is the total number of training datasets). And CHF can be predicted in a manner of regression through model optimization as follows

$$\{\alpha_i, \alpha_i^*\} = argmin\ \frac{1}{2}\sum_{i=1}^{N}\sum_{j=1}^{N}(\alpha_i^* - \alpha_i)(\alpha_j^* - \alpha_j)\,K(x_i, x_j) - \sum_{i=1}^{N}(\alpha_i^* - \alpha_i)y_i \quad (5\text{-}1)$$

Eq. (5-1) is a mutant form of the prime duality optimization problem in the ν-SVM classification and regression. The purpose of the first term of Eq.(5-1) is to minimize the total number of support regression vectors while regularization of the deviations of solutions is achieved in the second term of Eq.(5-1). Besiding, the search of optimal and unique solution to Eq.(5-1) is a constrained dual problem. The solution to Eq. (5-1) is subjected to the following set of constrained conditions,

$$\begin{cases} \sum_{i=1}^{N}(\alpha_i^* - \alpha_i) = 0 \\ 0 \le \alpha_i^*, \alpha_i \le \frac{C}{N} \\ \sum_{i=1}^{N}(\alpha_i^* + \alpha_i) \le C\nu \end{cases} \quad (5\text{-}2)$$

where α_i^* and α_i are the Lagrangian multipliers that associate with the constraints. This study adopted the Gaussian kernel function to map pressure *P* and mass flux *G* into a higher dimension space by the Eq.(5-3),

$$\mathrm{K}(x_i, x_j) = \exp(-\frac{\|x_i - x_j\|^2}{2\sigma^2}) \tag{5-3}$$

where $\|x_i - x_j\|^2$ is the $\mathcal{L}^2$-2 norm of $x_i - x_j$ and σ is the scale parameter of the hypersurface. This Gaussian kernel function is to map the nonlinear relation of CHF with respect to pressure and mass flux into the linear high-dimensional relation. Then the regression equation of CHF prediction is defined by as follows:

$$y = \sum_{i=1}^{N}(\alpha_i - \alpha_i^*)\mathrm{K}(x_i, x) + b \tag{5-4}$$

where b can be computed as

$$b = \frac{1}{2}(y_m + y_n - \sum_{x_i \in SV}(\alpha_i - \alpha_i^*)[K(x_i, x_m) + K(x_i, x_n)]) \tag{5-5}$$

where m and n are the subscripts of which $\alpha_m \approx 0$ and $\alpha_n \approx C/N$ respectively. SV is referred as the support vector set of $|\alpha_i - \alpha_i^*| \neq 0$. Eq.(5-4) is the so-called expansion of support vector. It is noted that three important parameters in the ν-SVM should be properly tuned by optimal methods - σ, C and ν. σ^2 is automatically determined by the optimal method based on distances from samples to enclosing surfaces as proposed by Xiao et al. (Xiao, Wang, & Xu, 2015); an overestimation of σ will enable the kernel function to weaken the nonlinear projection power of from low-dimension to high-dimensions while underestimating σ makes kernel function weaken regularization of deviation, and the decision hyperplane will become highly sensitive to outliers in training data. It is very significant to tune *C* correctly in the good practice of SVM application. If *C* is larger than the expected value, the SVM regression model will restrict its fitting ability of trained data

points. While a small value of C enhances the fitting ability of SVM, but deteriorates the prediction ability of the SVM regression model. ν is also needed to be tuned properly with training CHF data. A large value of ν forces the model selector to enclose more support vectors and yield an over-fitting model. On the contrary, for a small value of ν, the model will utilize less support vectors, which will under-fit the trained data. The grid search coupled with five-fold cross validation proposed in the previous research (Rudi, Chiusano, & Verri, 2012) is used to obtain optimal C and ν in the SVM regression CHF model of this study. In this study, the CHF regression to mass flux and pressure is performed only under the highly subcooled flow boiling. This approach capitalizes on the fact that the parametric profile of CHF exhibits clearly linear behaviors with respect to X_e in the subcooled flow (Fig.5-1 (a)). Hence, the primary objective of CHF regression was to resolve issues with the parametric behaviors of CHF with respect to pressure (P) and mass flux (G).

5.3.1 Look-up Table Reconstruction with Sparingly Distributed Experimental Data

First of all, a CHF-look up table construction from sparingly-distributed experimental CHF data points was studied to explore experimental strategies for helping save and rationalize efforts in collecting CHF experimental data. That is, the proposed methodology is designed to highlight the engineering concern – how many experimental CHF data points are needed for ν-SVM to achieve tabulation of CHF look table within an acceptable accuracy. The following contents are conducted and investigated to prepare training datasets for ν-SVM: evenly-distributed CHF data points shown as A,B,C,D, and E in Fig.5-2 were used for the training. The rest untouched region of the look-up table space served as the validation data points. In the first trial, 12 light green shaded entries marked by A in Fig.2 (~4% percent

of the total 315 data points) are used to train ν-SVM while the other data points were used for validation. In the second trial, 24 shaded entries (12 'A' data points + 12 'B' data points) are used as training data points. In the third trial, 36 shaded entries (12 'A' data points + 12 'B' data points + 12 'C' data points) are used for the training. In the fourth trial, 48 shaded entries (12 'A' data points + 12 'B' data points + 12 'C' data points + 12 'D' data points) are used for the training. In the fifth trial, all the marked points (total 60 points - A, B, C, D, and E) in Fig. 2 were used for the training. By progressively and gradually increasing the number of well-distributed data points used for training around the selected pattern, this study explores the sensitivity of prediction accuracy with respect to the number of training data CHF points.

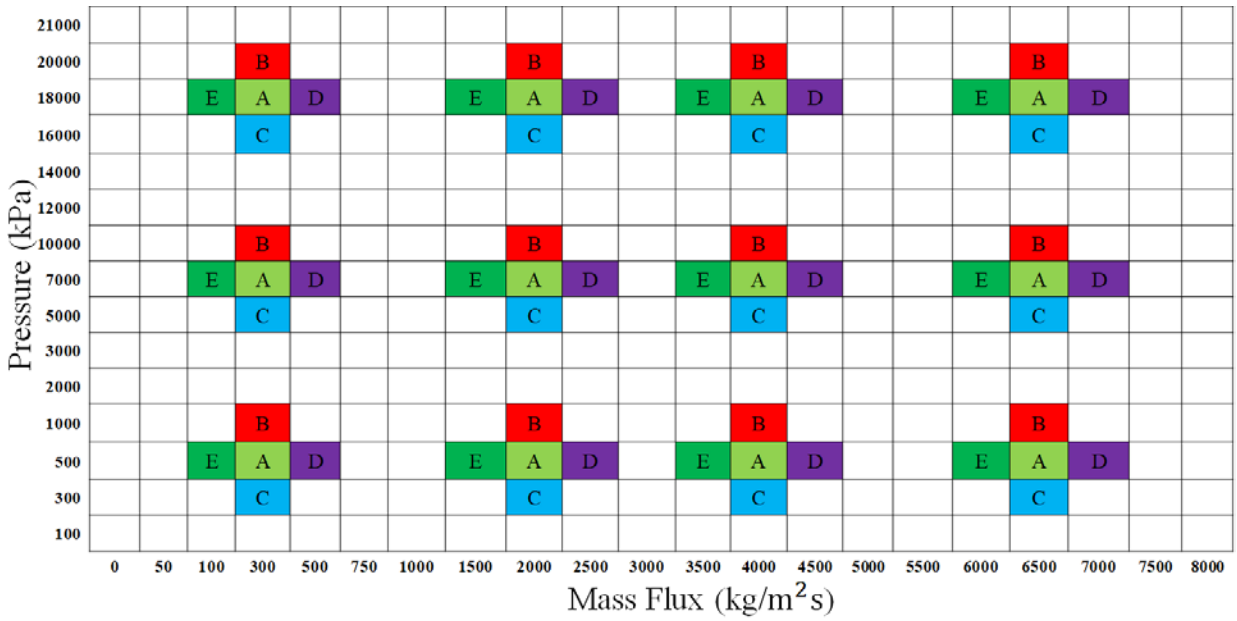

Fig.5-2 Schematic Illustration of CHF Extrapolation Using a Few Data Points

5.3.2 CHF Extrapolation for High Pressure using Low Pressure CHF Data

Two numerical validation experiments are performed to investigate the plausibility of high pressure CHF prediction using CHF under low pressure data. Firstly, CHF prediction at the pressure of 16 MPa (close to PWR steady-state operation,15.5 MPa) was evaluated by

SVM machines trained with data all lower than 16 MPa (Fig. 5-3a). Pressure of the training data was progressively increased from 100 kPa. It emulates the experimental cases where all CHF data were measured and collected at lower pressure than the PWR operating pressure. Secondly, a few data points from the high target pressure (16 MPa) were included in the training data while the majority of the data points used for training were based on the pressure lower than the target pressure (Fig. 5-3b). This emulates the experimental case where a limited number of experimental CHF data points is available and accessible at the high target pressure of PWR operation while most data points used for training were at lower pressures. Similar to the first experiment, training pressure progressively increased from 100 kPa while a limited number of data points (1 (A), 3 (A+B), and 5 (A+B+C), in Fig. 5-3b) of the target pressure were included for the training set. This methodological scheme enables experimentalists to investigate the strategic integration of low pressure experiments and high pressure experiments, for a tabulation establishment of comprehensive CHF data banks of new ATF cladding materials.

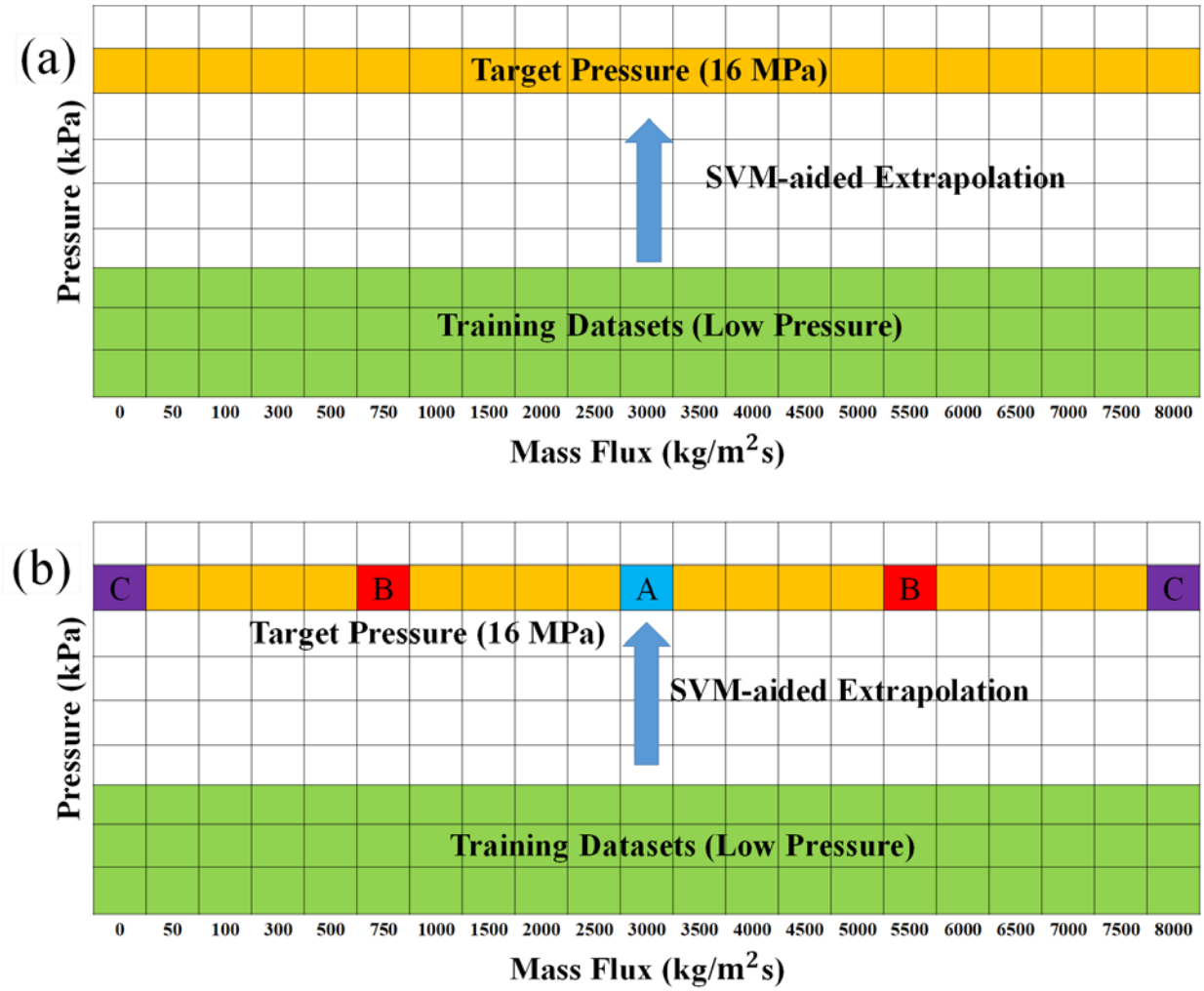

Fig.5-3 Schematic Illustration of High Pressure CHF Extrapolation using Low Pressure Data: (a) No data is available at High Pressure, (b) a limited number of data points (A, B, and C) are available at high pressure

5.4 Numerical Experimental Results

As expected, prediction accuracy of SVM based CHF model by the coefficient of determination (R^2) increases as the increasing number of training data (Fig.5-4). It can be noticed in Fig.4 that highly subcooled CHF with ($X \leq -0.1$) presents higher levels of accuracy compared to relatively less subcooled CHF ($-0.1 < X \leq 0.0$). Because PWR operates under the equilibrium quality (X_e) between -0.35 and -0.15, the pronounced prediction accuracy for the highly subcooled flow CHF experiments is an encouraging finding. It is remarkable that only 12 data points can yield a high level of prediction

accuracy (R^2 >0.8). The cost-benefit curve for the prediction accuracy versus the increasing training data population doesn't present a linear trend while shows an asymptotically increasing trend, which supports a rational decision for the number of experimental data to be collected, that is at certain point, further increasing the number of CHF training data points doesn't help gain the prediction accuracy much even at all. And two exemplary cases of highly subcooled CHF (Fig.5(a)-(b)) and less subcooled CHF (Fig.5(a)-(b)) further demonstrate that the region of prediction difference and prediction accuracy are dependent on the equilibrium quality because the thermalhydraulic presents different behaviors between less and highly subcooled flow boiling.

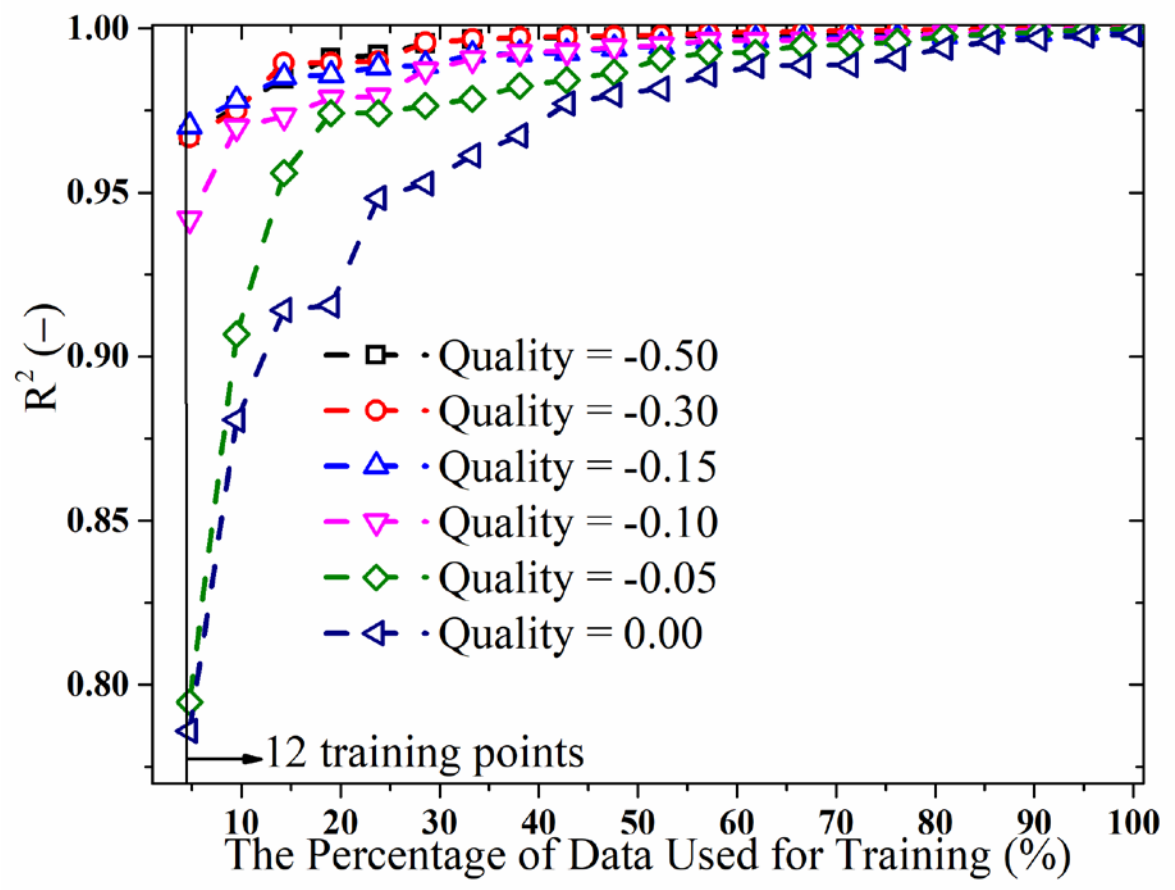

Fig.5-4 Prediction accuracy (R^2) change with increasing data population used for training (percentage of data in the CHF map for a specific quality, X_e), with the reference data distribution (12 evenly distributed locations)

In order to explore further the sensitivity of prediction accuracy with respect to the training data distribution, training data points were redistributed in a different manner while the total number of training data stayed the same as twelve as before. Four different data distributions were tested as shown in Fig.5-6; instead of assigning 12 locations, the number of locations for data selection for training respectively reduced to 4 and 6. Hence, the presented predictions represent cases where experimental data collection was not as well distributed as the reference case of 12 uniformly-distribution locations.

As shown in Fig. 5-7, increasing spread of data used for training (i.e., 12> 6> 4 for data collected locations) in the pressure & mass flux region of the CHF look up table helps improve CHF prediction accuracy. Additionally, prediction accuracy with the vertical data arrangements (along the pressure axis) is improved when comparing to the horizontal data arrangements (along the mass flux axis) implies that capturing CHF behavior with respect to pressure is more critical to the overall prediction accuracy. It is clearly observed in Fig. 5-7 that a nicely spread pattern of experimental CHF data can drastically help reduce requirements of experimental CHF data points.

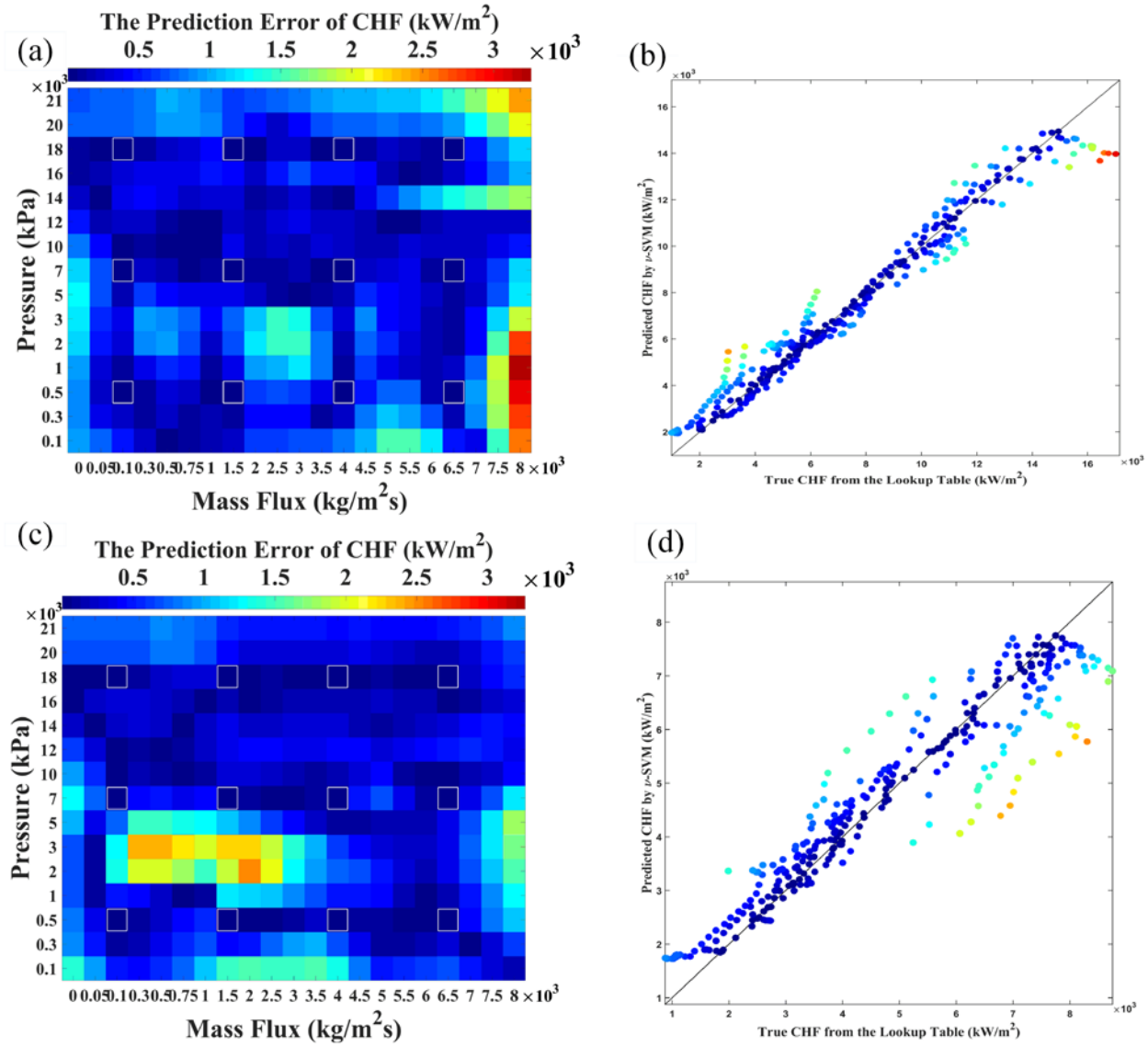

Fig.5-5 CHF Prediction with 12 evenly distributed data points: (a) Map for absolute difference in CHF prediction (X_e=-0.15), (b) Comparison between prediction and true CHF (X_e=-0.15), (c) Map for absolute difference in CHF prediction (X_e=-0.05), (d) Comparison between prediction and true CHF (X_e=-0.05)

As for the CHF extrapolation from low pressure to high pressure is considered, it is clearly demonstrated in Fig. 5-8 that a reasonable level of prediction accuracy can be achieved only when training data has pressures fairly close to the target pressure (16MPa). The prediction accuracy demonstrating non-linear behaviors, showing a sharp increase after a certain pressure. It provides us with a suspect that those pressures after which the prediction

accuracy sharply increases correspond to the inflection points of the CHF behavior. It is elaborated with more details and discussions below.

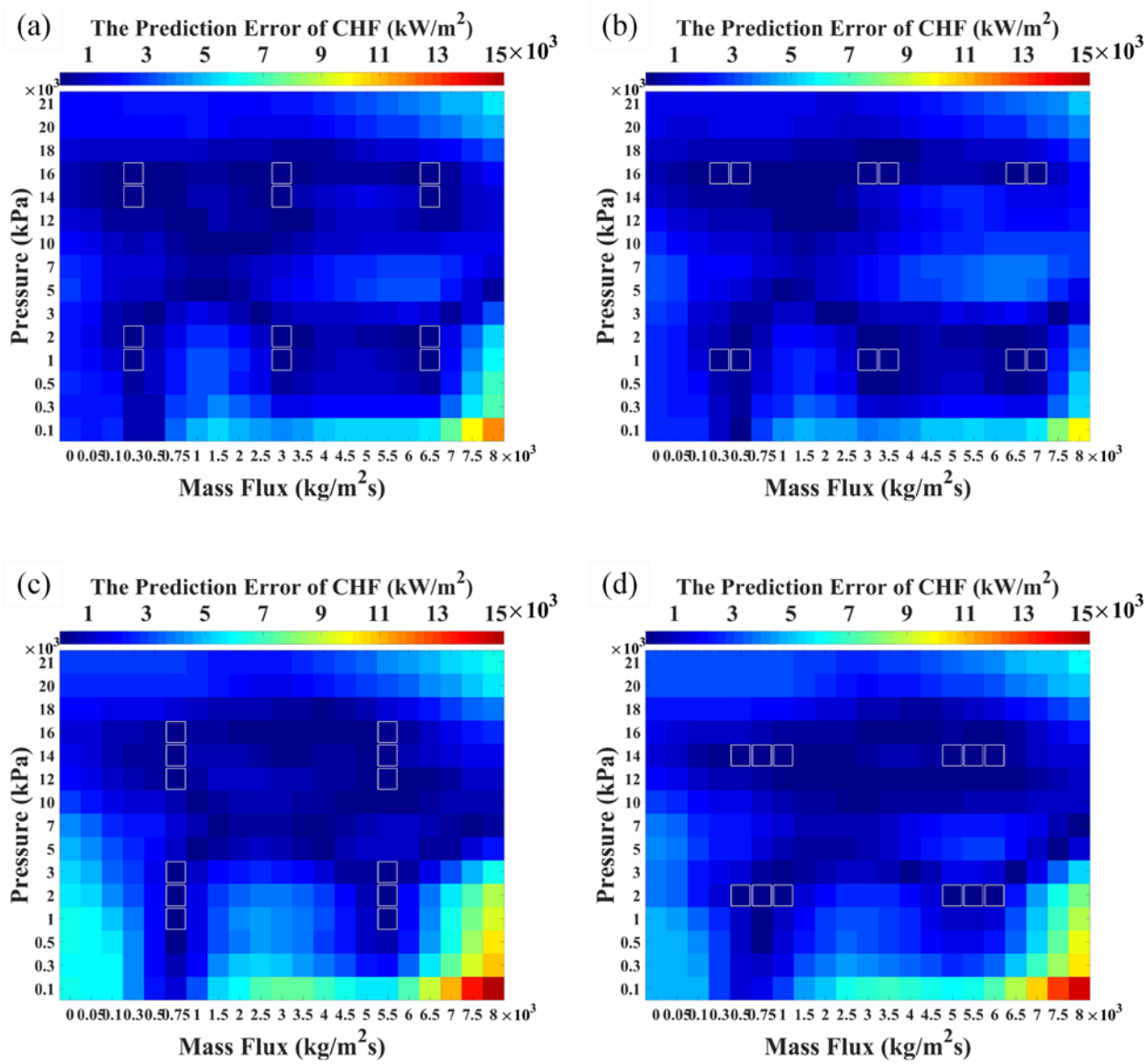

Fig.5-6 CHF Prediction with data distributions different from the reference 12 even locations for the case with X_e =-0.5: (a) 6 vertical locations, (b) 6 horizontal locations, (c) 4 vertical locations, (d) 4 horizontal location

Including a few CHF data points from the high target pressure of 16 MPa dramatically helps ν-SVM obtain modeling accuracy in CHF extrapolation from low pressure to high pressure. In Fig. 8 (a)-(d) , it was found out that incorporating a limited number of CHF

data points from the target pressure (16MPa) into training CHF data increases the too much accuracy CHF prediction primarily based on low pressure data. This announces a chance of strategic CHF experiment integration between high pressure and low pressure. In other words, while most experimental CHF data are measured and obtained at low pressure conditions, the ν-SVM can effectively make a good use of a limited number of CHF data points in the high target pressure for highly accurate CHF prediction.

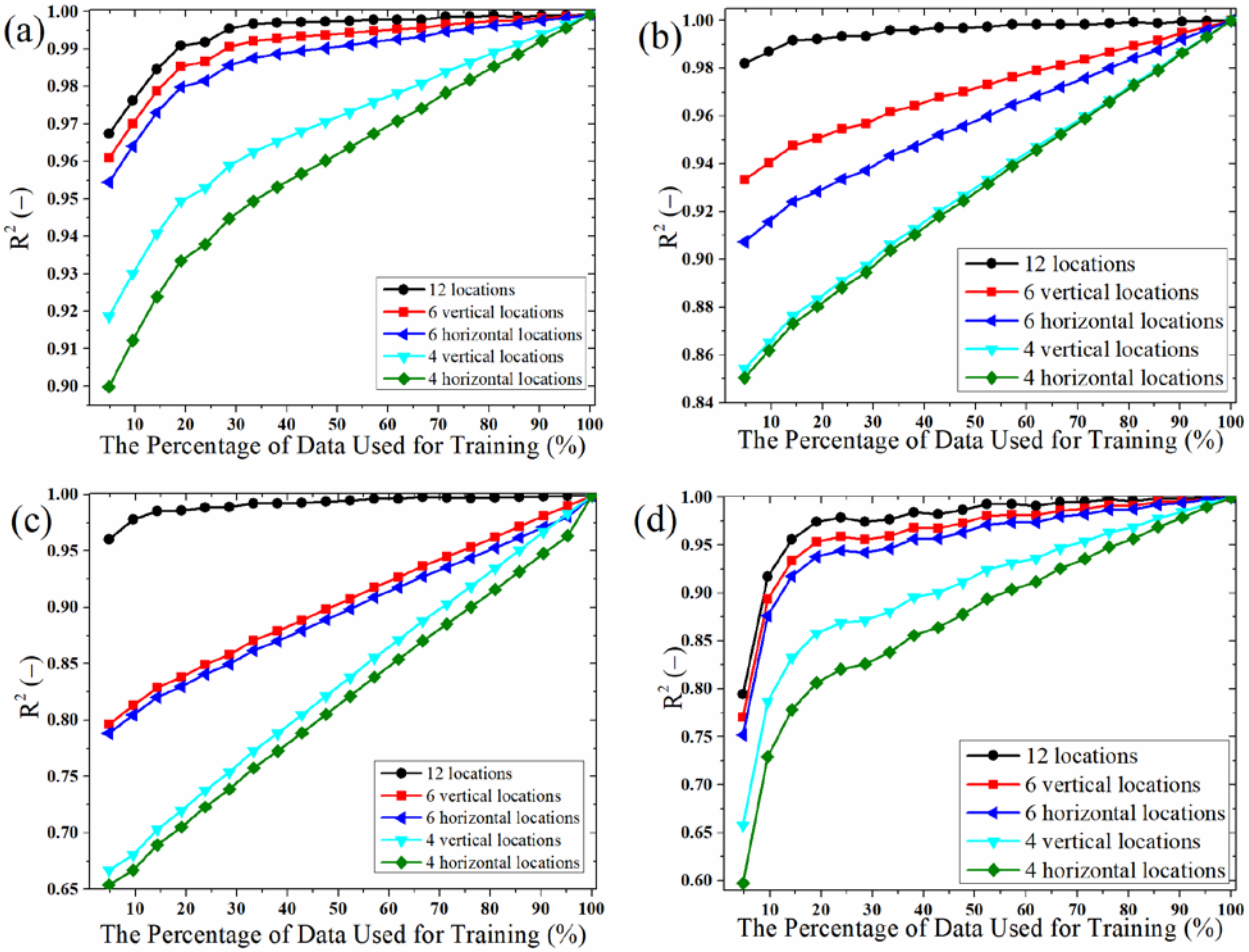

Fig.5-7 Investigations of the Effects of Different Blocks Distribution under Subcooled Conditions: (a) X_e = -0.50, (b) X_e = -0.20, (c) X_e = -0.15, (d) X_e = -0.05

5.5 Results Analyses and Discussions

5.5.1 Pressure-Variant CHF Inflection and its Impact on Prediction accuracy

The ν-SVM prediction performance depends on the CHF parametric profiles with regard to system pressure, mass flux of coolant and equilibrium quality of flow boiling, and the distribution of training data points capturing that parametric behavior. For the CHF regression to pressure, the CHF prediction accuracy is directly determined by existence of a CHF inflection point and availability of training data in the proximity of that inflection point. In the Groeneveld's look-up table (Groeneveld et al., 2007), when the equilibrium quality is above -0.20, an inflection point exists in the parametric profile of CHF with respect to pressure. In Fig.5-9 (a), it is demonstrated that for an exemplary case (G=3000 kg/m^2s, X_e=-0.15) the maximum absolute error of CHF prediction with respect to pressure occurs at the inflection point of the pressure-CHF variant. In this situation, the pressure of the inflection point is 3000 kPa while two closest pressures to the CHF inflection point used for the training data are 500kPa and 7000kPa, respectively from left and right sides. This explains why the ν-SVM trained by such datasets cannot precisely model the CHF profiles with a pressure inflection point.

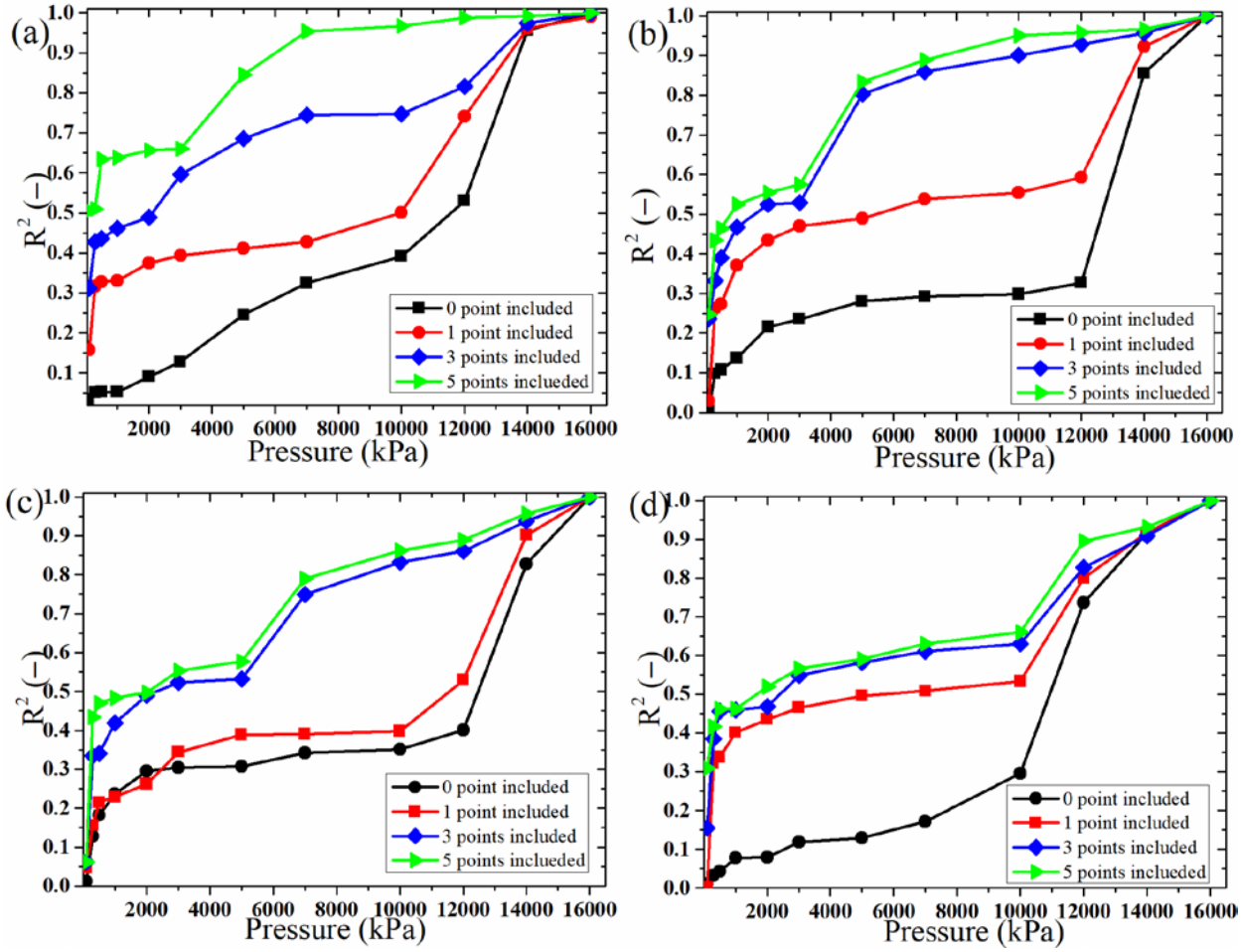

Fig.5-8 ν-SVM supported pressure extrapolation for the target pressure of 16 MPa, and x-axis represents progressively increasing pressure level used for training: (a) x_e=-0.5, (b) x_e=-0.3, (c) x_e=-0.15, (d) x_e=-0.05

It is shown in Fig.5-9(b) that how the prediction error of the inflection point contributes to the overall error (summation of absolute errors of CHF prediction for the range of pressure for fixed mass flux and X_e). As the difference between the closest pressure to the inflection pressure ($\Delta P_{inflection} = min|P_{inflection} - P_{training}|$) increases, the contribution of error at the inflection CHF point to the overall error increases. It is seen in Fig. 5-9(b), that in the Groeneveld CHF look-up table (2007), around 15~20 percent of the overall CHF prediction error with respect to pressure is contributed by the error at the pressure inflection point, for the reference data case of 12 evenly distributed CHF data points. This explictly

implies that preparation of training data points close to pressure inflection points is key to the overall accuracy improvement of ν-SVM CHF prediction.

All ongoing analyses in Fig5-9.(a)-(d) were evaluated by the reference case of 12 evenly distributed training data that is shown in Fig. 5-2. Contribution of the pressure-variant CHF inflection point to the overall prediction accuracy can be explored from a different perspective by evaluating the accuracy gain of R^2 for CHF prediction but excluding the pressure inflection point. It was shown in Fig. 5-9 (c) that the potential improvement of R^2 for CHF prediction in case pressure inflection points were excluded. This implies the reduction of the CHF predictability due to the pressure-variant CHF inflection point, addressing the importance of procuring training CHF data points around pressure-variant CHF inflection points. This insight naturally leads to consideration that conditions (G and X_e) with no or less pronounced pressure-variant CHF inflection behavior would produce a higher level of CHF prediction accuracy based on ν-SVM.

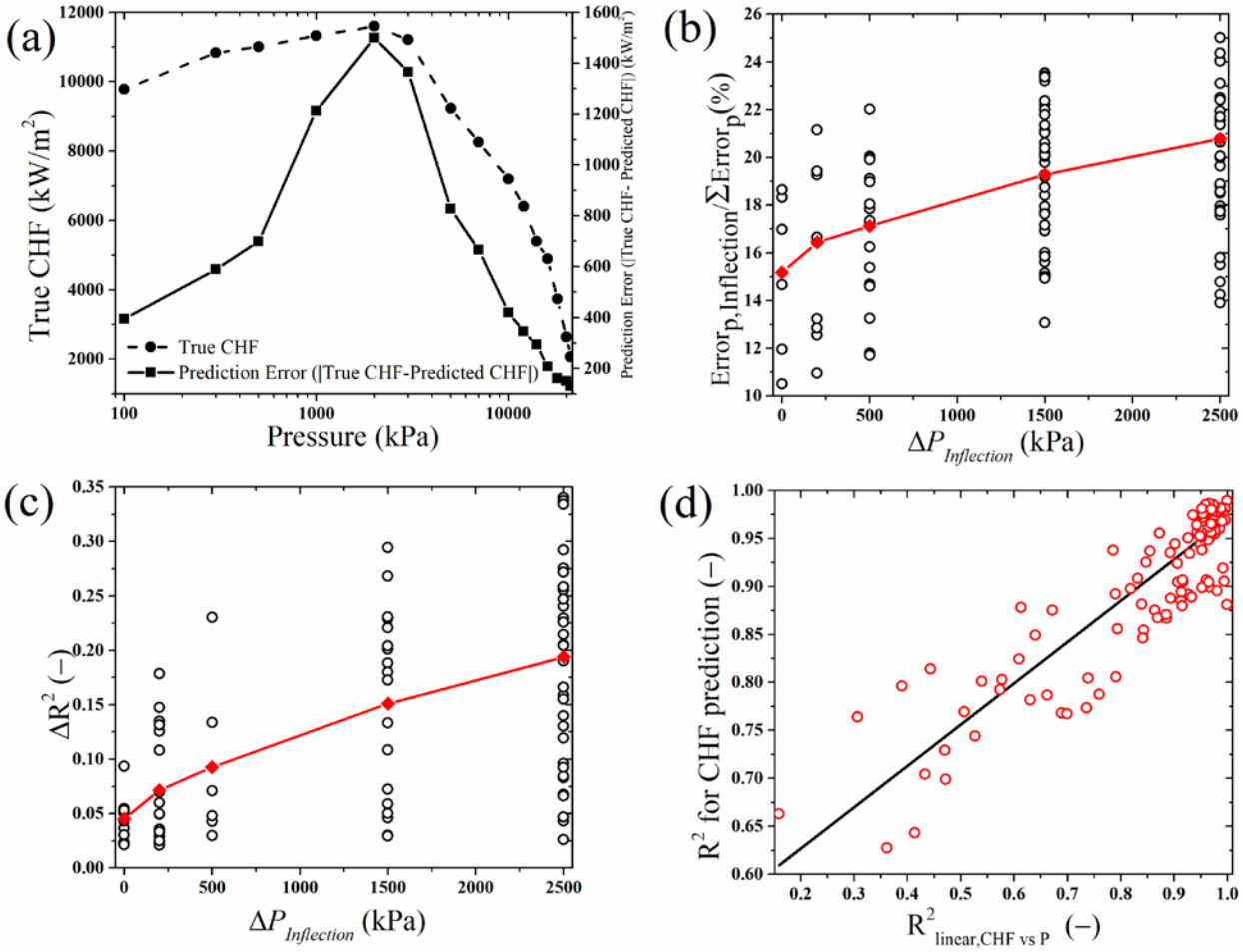

Fig.5-9 (a) Exemplary CHF behavior and ν-SVM prediction error with respect to pressure at X_e =-0.15 and G=3000 kg/m^{2}s; (b) Fraction (%) of prediction error of the inflection point to the overall error (summation of absolute errors of CHF prediction for the range of P for fixed G and X_e) with respect to the difference of closet training data to the inflection pressure ($\Delta P_{inflection} = min|P_{inflection} - P_{training}|$), red line shows the average; (c) Potential improvement of R^2 by excluding the pressure inflection point ($\Delta R^2 = R_*^2 - R^2$, where R_*^2 is the coefficient of determination excluding the inflection pressure) with respect to the difference of closest training to the inflection pressure, $\Delta P_{inflection}$; (d) ν-SVM prediction accuracy with respect to linearizability of CHF behavior with pressure where $R^2_{linear,\ CHF\ vs\ P}$ is the coefficient of determination for the linear fitting of pressure-variant CHF behavior.

How CHF inflection behavior presents could be indicated by parameterizing its pressure-variant behavior with the linear fitting ($R^2_{linear,\ CHF\ vs\ P}$). Fig. 5-9 (d) shows the clearly positive correlation between the CHF prediction accuracy and linearizability of CHF with respect to pressure ($R^2_{linear,\ CHF\ vs\ P}$), which demonstrates that ν-SVM could yield a more robust prediction under conditions resulting in more linear CHF behaviors with respect to

pressure. The inflection point of CHF appears because of the two competing mechanisms of the fluid property variation characterized by increasing density and decreasing heat of vaporization (h_{fg}) with regard to increasing pressure. Hence, for some fluids with a less pronounced h_{fg} decreasing with pressure, the pressure-variant CHF inflection may be not so appreciable as water does. As those fluids, the applicability of ν-SVM to support CHF prediction is expected to further rise.

The observed behavior of prediction accuracy for CHF extrapolation from low pressure to high pressure in Fig. 5-8 can also be explained by the pressure inflection points. There exists a pressure inflection point at which the CHF extrapolation accuracy sharply increases while the pressure for training data progressively increases towards the high target pressure. This pressure point corresponds to the pressure-variant CHF inflection point. Physically, the CHF inflection behavior is significantly because of the decreasing heat of vaporization (ΔH_{fg}) with respect to increasing pressure. It implies that the CHF extrapolation from low pressure to high pressure can only be accurately performed with the presence of training data implying the inflection of pressure-variant CHF. Those training CHF data points from which the overall pressure-variant CHF behavior can be inferred can be provided by data in the proximity of the inflection point and/or the high target pressure.

5.5.2 CHF behavior with Mass Flux and its Impact on Prediction Accuracy

Unlike the aforesaid pressure-variant CHF profile that is typically characterized with the inflection point, the CHF monotonically increases with the increasing of mass flux (G),

implying that ν-SVM can predict CHF more accurately for mass-flux-variant CHF behavior than pressure-variant CHF behavior. However, the departure from the linear behavior of CHF with regard to mass flux still deteriorates the CHF prediction accuracy. Fig. 5-10 (a) shows exemplary behaviors of CHF of two completely different conditions; highly linear behavior with mass flux ($R^2_{\text{linear, CHF vs G}}$= 0.9512) and significant departure from the linear behavior with mass flux ($R^2_{\text{linear, CHF vs G}}$=0.6467). How CHF linearly behave with respect to mass flux is the primary key to the CHF prediction accuracy of ν-SVM. As clearly demonstrated by the positive correlation between R^2 for CHF and $R^2_{\text{linear, CHF vs G}}$ in Fig.5-10 (b), the linearizability of CHF with mass flux is a robust parameter that is directly proportional to prediction accuracy of ν-SVM. Hence, conditions that enhance the linear behavior of CHF with mass flux will allow ν-SVM to achieve a higher prediction accuracy. It is important, however, to note that ν-SVM is very much applicable for CHF prediction as far as parametric behavior dependent on the mass flux is considered in the training data as CHF monotonically decreases with mass flux regardless of types of fluids.

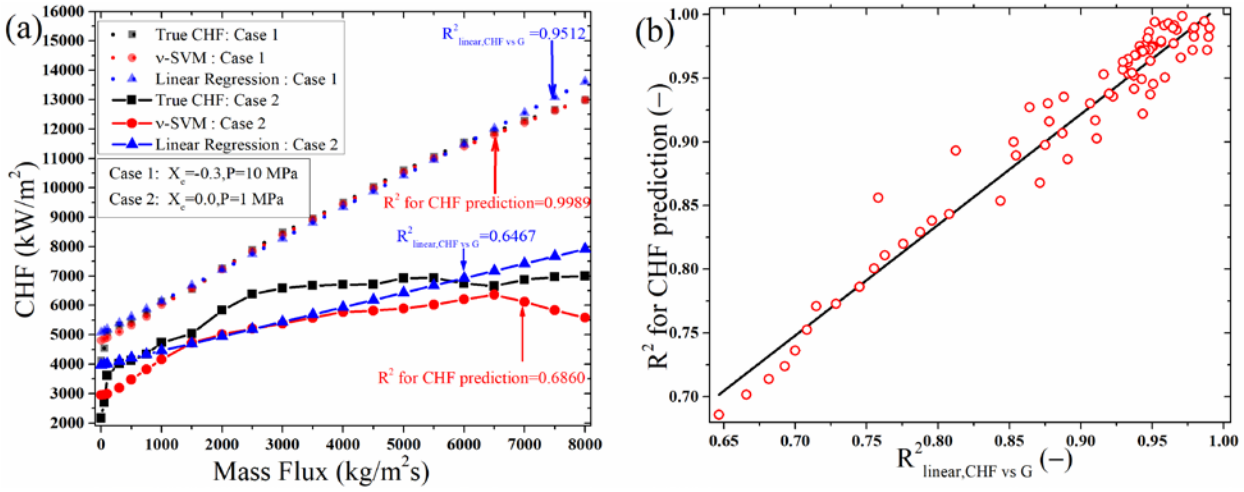

Fig.5-10 (a) Exemplary behavior of CHF in two different conditions - highly linear behavior with G ($R^2_{\text{linear, CHF vs G}}$= 0.9512) and significant departure from the linear behavior with G ($R^2_{\text{linear, CHF vs G}}$=0.6467) and ν − SVM predictions; (b) the predicted CHF respectively based on linear regression and ν-SVM regression for the case with X_e= -0.15 and P=7000 kPa. All presented analyses in (a)-(b) were evaluated with the reference 12 evenly distributed training data shown in Fig. 5-2.

5.5.3 Limited predictability for pool boiling using flowing boiling data

It is noteworthy that the ν-SVM trained by flow boiling CHF data points (G >0) has limited ability in predicting pool boiling CHF accurately (G=0). Fig. 5-11 shows the significant decrease of prediction accuracy for the pool-boiling CHF (G=0) throughout the entire range of subcooled equilibrium qualities. Namely, the abrupt change of CHF for pool boiling due to the absence of different flow phenomenology, cannot be solely modelled by the numerical method based on the training CHF data of flow boiling. This typifies a limitation of the ν-SVM based CHF prediction. More precisly, ν-SVM cannot take the role of physics; procuring CHF data in wide ranges to cover the key phenomenology is critical in the assurance of an acceptable level of prediction accuracy.

5.6 Summaries of Chapter 5

In this study, it was demonstrated that the ν-SVM can be effectively and reasonably applied to predict CHF under subcooled flow boiling, thereby supporting the tabulation of ATF look-up table for PWR operation. Obtainment of training data points that include the information about the parametric behavior of CHF with respect to pressure and mass flux is the key to predict CHF in a high level of accuracy. As for the pressure-variant CHF profile, training data in the proximity of the inflection point drastically contribute to the accuracy of CHF prediction. Hence, the prediction accuracy could be much enhanced by physics-informed training data preparation with knowledge of CHF inflection points. The linearization trend of CHF with respect to pressure and mass flux determines the degree of prediction accuracy, in the absence of a good spread distribution of training data points that captures the parametric trends. CHF extrapolation to a higher pressure by using many CHF

data points measured at low pressure can be efficiently conducted if a few data points are available in the high pressure. This speaks to the possibility of the strategical CHF experimentation integration between high and low pressure conditions, with a significantly-reduced experimental cost associated with the high system pressure requirements. Nowadays, there is a compelling demand of CHF evaluation of advanced ATF cladding materials compatibly with the current look up table CHF implementation in thermal hydraulics codes. The proposed methodological finding provides engineering experiment strategies to help the look-up table tabulation for advanced cladding materials in an efficient manner.

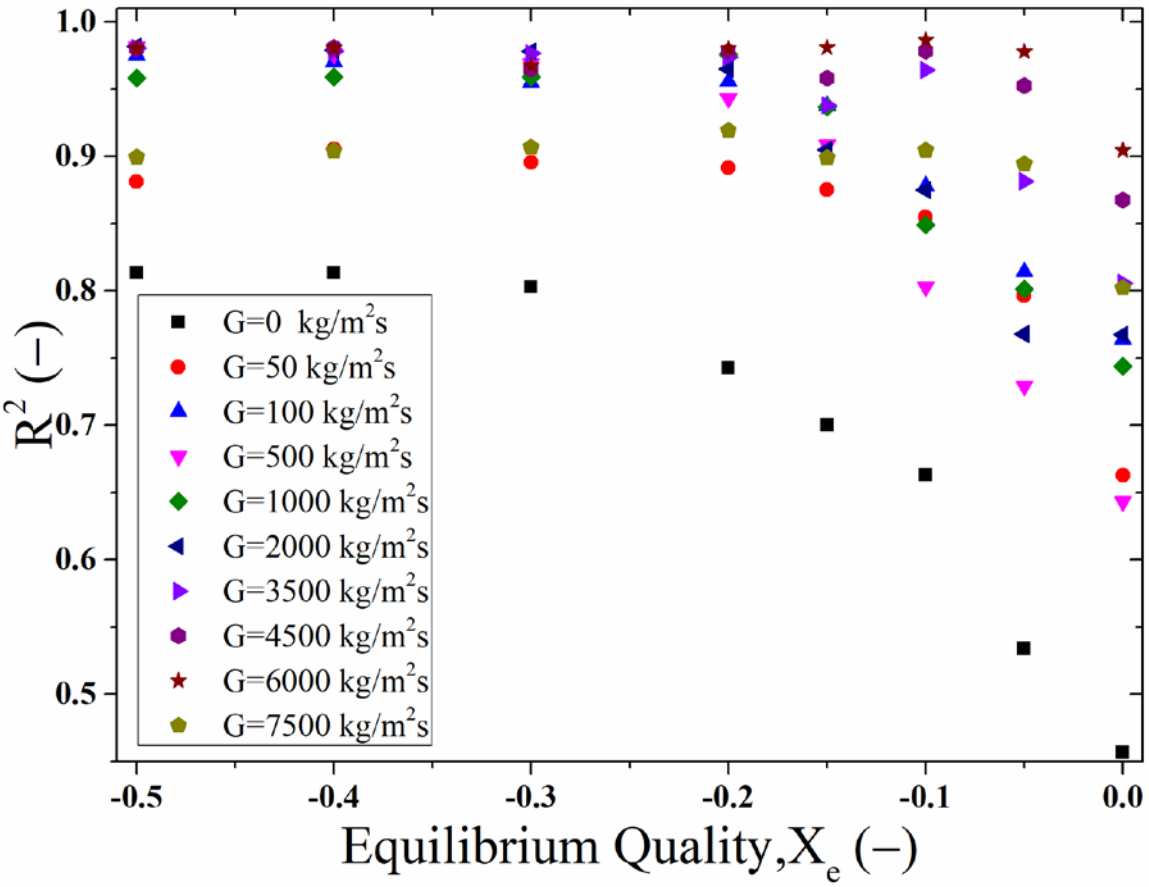

Fig.5-11 CHF prediction accuracy with respect to different equilibrium qualities and mass flux. Note the relatively low prediction accuracy for pool boiling CHF (G=0) based on flow boiling data. The prediction was made with the reference 12 evenly distributed training data shown in Fig. 5-2.

6 CLOSING REMARKS

6.1 Concluding Summaries

Various enhancement techniques for boiling heat transfer are comprehensively reviewed in this thesis. Macroscale enhancement techniques, including extended surfaces of macro fins and ridges, porous mesh grids and foamings, provide different enhancement degrees of both HTC and CHF, along with a certain decrement of the incipience superheat and ONB. However, attaching extended surfaces on a top of a temperature sensitive device might introduce significant contact resistances that increase surface temperature of device, and even may induce thermal stresses. On the contrary, macroscale enhancement techniques are more able to resist effects of aging and structure failures than both (either) micro and(or) nanoscale enhancement techniques. Microscale boiling heat enhancement techniques have following primary benefits including increased nucleation site density, wettability augmentation, wickability amplification of liquids. It seems that modulated microporous structures are especially prominent owing to their significant potential improvement of CHF because vapor detachment paths is separated from the rewetting paths of resupplying paths through the different microscale techniques. Nanoscale enhancement techniques, which are surface coatings by tubes, fibers, wires, porous and film layers at nanoscales. The primary advantage of nanoscale enhancement is boiling heat enhanced by improving capillary forces of working liquids within nanostructures. Nevertheless, surface structures at micro- and/or nanoscale are highly susceptible to the blockage of oxidization layer, introducing enhancement decay of HTC and CHF as time goes by. The nanofluids application to enhancement of boiling heat transfer is full of uncertainties because the mechanisms behind enhancements of CHF and HTC are still not

clearly and controversial. On the hand, the concentration of nano-particles will increase as the total amount of boiling time accumulates due to the solution vaporization of working fluids; there is an optimal concentration of nanofluid allowing CHF to be maximally enhanced.

In this thesis, a prior work has been done for the CHF prediction approach based on the framework of ensemble learning. Three primary influential factors that remarkably affect CHF are explored their effects on CHF respectively by different machine learning algorithms, namely, deep belief network, general regression network and support vector machine. The main findings about CHF studies are presented as follows based on the proposed methodologies:

(1) Through studying parametric trends of CHF with respect to geometric parameters of cylindrical micro-pillar array reveals that the effect of height on CHF is more complicated than that of diameter and spacing and the total number of pillars fabricated on the surface has influential impacts of the parametric trends of CHF.

(2) The parametric trends of CHF predicted by the proposed methodologies corresponds to the analyses of experimental results from the published literatures and the qualitative analyses to the effects of diameter, height and spacing of micro-pillar arrays.

(3) In studies of the effects of thermal properties of heater materials on CHF, the trained machine learning model gives similar parametrical trends of CHF to that of current empirical correlation models with respect to thermal activity. But the trained model yields better prediction accuracy because thermal activity alone cannot sufficiently

represent the effects of thermal properties of materials on CHF as pointed out in published literatures.

(4) Regardless of boiling surface materials, the effects of dimensional sizes of boiling surface on CHF are absent once the side length is beyond a certain value that is related with the capillary length of fluids. Besides, CHF reaches the maximum value that is determined by thermal activity and diffusivity of boiling surface material when the side length of square boiling surface is equal to the Raleigh-Plateau instability wavelength. Because in such case, the instability growth rate reaches the maximum value.

(5) The ν- support vector machine is the best reconstruction method for the CHF lookup table of the subcooled flow boiling if the total number of experimental CHF data points is small and those experimental data points could reflect the CHF-variance with respect to pressure.

(6) The existence of inflection points has impact on the prediction accuracy and the size of training datasets. Because more training data points around those inflection points are needed by the machine learning algorithms to capture parametric trends effectively.

From a prospective of thermal system design, despite a large amount of published articles addressing experimental investigation and theoretical analyses for boiling heat enhancement, there is a scarcity of sufficiently reliable databases elaborating these enhancement explanations and experiments in terms of fluid type, surface material, size, and orientation, enhancement shape, pattern, scale, subcooled temperature, and operating pressure. This thesis renders a prior databased for designing enhanced surfaces for practical applications to boiling heat transfer, condensation and cooling. This thesis also provides a

guideline to predict CHF enhanced by multiple techniques such as nanofluids hybrid with micro pin fin structures.

6.2 Recommendations for Future Works

Although CHF obtained on plain plate surfaces is used as the reference case in many CHF enhancement experiments and the side length of those plate surfaces varies from 5 mm to 50 mm to some extent, almost all of them are square boiling surfaces and a few of surfaces are non-square shapes. There are still some experimental investigations about the effects of geometrical dimensions on CHF:

(1) For the plate and circular heat transfer substrates with same surface areas and thickness, the CHF is much different for each substrate as experimental results from published paper shown, but how to correlate the effect of geometrical shape is still unresolved yet.

(2) For plate surfaces, some experimental results have shown that the aspect ratio has some unknown influences on CHF (Kam et al., 2018). But the experiments about CHF on plate surfaces with various aspect ratios and the same surface area are in the pending status.

There are still some untouched regions that are worthy of theoretical and experimental exploration in the future design of microstructure enhanced pool boiling although many experiments and theories are reported, including:

(1) Whether r and φ_s are capable of correlating the effects of pillar shape and distribution pattern should be verified by pool boiling experiments enhanced by different microstructured surfaces but the fixed r and φ_s.

(2) How the dimensional sizes of heat transfer substrate affect the microstructure enhanced CHF is not clear now, pool boiling CHF experiments are suggested to perform on different sized surfaces with a same set of pillar array.

(3) In the reported experiments, for silicon based pillar arrays, the geometrical parameters are at the nano- and micro-scales while the copper or stainless steel pillar array has a magnitude of millimeters. Due to the scale effect, the CHF triggering mechanisms at the scale of nano-and micrometer present a different story from those at the millimeter scale. In order to further utilize the regression capacity of deep belief network, the silicon pillar arrays at the macroscale shall be explored in future designs of structured surfaces.

(4) Pillar arrays improve the hydrophilic ability of surface but degrades the heat transfer coefficient. Leaving some regions untouched but fabricating pillar arrays on plain surfaces in a certain manner can further enhance CHF and heat transfer coefficient because experiments demonstrate that much higher CHF and heat transfer coefficient are obtained on the heat transfer surface with hydrophilic networks featuring hydrophobic islands than of the hydrophilic or hydrophobic surface. Therefore, how to configure the untouched and pillared regions optimally for CHF maximization might be one of the experimental explorations in future designs of CHF experiments.

(5) How to reduce and predict the heat flux and superheat at the nucleate boiling incipience is of importance to the improvement of thermal efficiency. But relevant experiments and studies are not reported yet for the microstructured surfaces. Researches about the onset of nucleate boiling should be performed on structured surfaces to complete the framework of enhanced heat transfer.

APPENDIX

Microstructure-Enhanced CHF Databanks of Pool Boiling

CHF datasets from experiments concluded in **Tab.3-1** are complied in **Tab.V** and **Tab.VI**, noting that ID in **Tab. V** and **Tab.VI** are referred to the experiment ID in **Tab.3-1**, and in some papers, CHF data are extracted by using plot digitizer app. For a plain surface, diameter, height and spacing are zero.

Tab. V CHF Databank of Pool Boiling Enhanced by Cylindrical Pillar Surfaces

ID	Subcooled (K)	Diameter (um)	Height (um)	Spacing (um)	CHF (kW/m^2)
1	0	0	0	0	756.1156
1	0	10	10	15	1646.125
1	0	10	20	15	1678.473
1	0	5	20	10	1764.83
1	0	10	20	10	1888.88
1	0	10	20	5	2018.274
1	0	5	20	5	2077.627
2	0	0	0	0	747.4443
2	0	11.2	10.4	13.8	1687.344
2	0	11	17	14	1956.18
2	0	10.8	16.3	14.2	1657.245
2	0	16	17	9	1464.796
3	0	0	0	0	794.5586
3	0	10	20	15	1962.367
3	0	10	20	5	2044.428
3	0	5	20	10	2356.65
3	0	0	0	0	1957.136

3	0	30	35	30	2325.918
3	0	30	61	30	2356.65
3	0	35	68	30	2494.943
4	0	0	0	0	699.0447
4	0	20	10	5	792.5973
4	0	20	10	20	1032.178
4	0	20	10	40	671.5166
4	0	20	20	5	1321.008
4	0	20	20	20	1711.993
4	0	20	20	40	1169.818
4	0	20	40	5	1571.556
4	0	20	40	20	2171.583
4	0	20	40	40	1249.607
4	0	5	20	5	1618.44
4	0	5	20	10	1589.656
4	0	5	20	20	1896.302
5	0	0	0	0	697.8
5	0	20	10	5	798.484
5	0	20	10	20	1037.505
5	0	20	10	40	666.4657
5	0	20	20	5	1316.257
5	0	20	20	20	1704.744
5	0	20	20	40	1167
5	0	20	40	5	1570.203
5	0	20	40	20	2162.604
5	0	20	40	40	1194.329
5	0	5	20	2	1620.025

5	0	5	20	10	1891.419
5	0	5	20	20	1246.674
6	0	0	0	0	714
6	0	20	20	5	1069.963
6	0	20	20	20	1518.186
7	0	4	8	70	1420
7	0	15	16	90	1480
7	0	120	16	205	1560
7	0	15	32	90	1600
7	0	120	32	205	1590
7	0	40	32	65	1610
7	0	15	16	21	1780
7	0	15	32	21	2170
7	0	4	16	7	2190
7	0	0	0	0	754.7952
8	0	4	20	4	1477.838
8	0	4	20	12	2147.24
8	0	8	20	8	1807.884
8	0	8	20	24	2008.544
8	0	40	20	40	1850.905
8	0	40	20	120	1286.488
8	0	80	20	80	1707.393
8	0	80	20	240	1114.402
8	0	0	0	0	1100
9	0	0.44	0.264	0.36	176.5022
9	0	0.44	0.396	0.36	194.8635
9	0	0.44	0.704	0.36	222.1063

9	0	0.44	1.408	0.36	236.4437
9	0	0	0	0	158.449
10	0	0	0	0	906.30453
10	0	40	20	40	1635.4
11	0	0	0	0	910.4
11	0	0.5	2	0.1	1145
11	0	0.36	2	0.25	1151
11	0	0.28	2	0.33	2143
12	0	0	0	0	1260.233
12	0	10	20	10	2408.851
12	0	15	20	15	2253.907
12	0	20	20	20	2294.452
13	0	0	0	0	1192
13	0	0.15	5	0.35	1706
13	0	5	3	5	2096
14	0	0	0	0	441
14	0	5	5	5	631.0782
14	0	10	5	10	615.367
14	0	20	5	20	533.1851
14	0	50	5	50	568.1325
14	0	50	50	50	581.5517
14	0	100	50	50	569.6814
15	0	0	0	0	842
15	0	40	20	40	1877
15	0	40	20	120	1013
15	0	80	20	80	1485
15	0	80	20	240	964

16	0	0	0	0	272
16	0	500	400	500	420
16	0	500	400	300	462
16	0	500	400	100	428
16	0	350	550	250	479
28	0	50	23.5	6	1563
28	0	0	0	0	1052

Tab. VI CHF Databank of Pool Boiling Enhanced by Square Pillar Surfaces

ID	Subcooled (K)	Width (um)	Height (um)	Spacing (um)	CHF (kW/m^2)
17	0	0	0	0	160.73
17	25	0	0	0	222.30
17	45	0	0	0	310.32
17	0	30	60	30	263.53
17	25	30	60	30	483.04
17	45	30	60	30	674.94
17	0	30	120	30	276.85
17	25	30	120	30	520.22
17	45	30	120	30	719.34
17	0	30	200	30	290.67
17	25	30	200	30	555.17
17	45	30	200	30	808.23
17	0	50	60	50	287.73
17	25	50	60	50	451.01
17	45	50	60	50	546.12
17	0	50	200	50	297.63
17	25	50	200	50	581.35
17	45	50	200	50	772.88

17	0	50	270	50	324.30
17	25	50	270	50	613.44
17	45	50	270	50	835.55
18	25	0	0	0	143.56
18	35	0	0	0	171.40
18	45	0	0	0	199.13
18	3	30	60	30	270.56
18	25	30	60	30	476.90
18	35	30	60	30	576.06
18	45	30	60	30	669.38
18	3	30	200	30	318.21
18	25	30	200	30	554.27
18	35	30	200	30	689.19
18	45	30	200	30	798.25
19	15	0	0	0	181.5
19	25	0	0	0	232
19	35	0	0	0	288
19	15	30	60	45	365.54
19	25	30	60	45	465
19	35	30	60	45	565
19	15	30	60	30	360
19	25	30	60	30	476.69
19	35	30	60	30	546
19	15	30	60	15	330.88
19	25	30	60	15	429
19	35	30	60	15	539.8
19	15	30	120	45	390

19	25	30	120	45	504
19	35	30	120	45	607.2
19	15	30	120	30	390.66
19	25	30	120	30	498.18
19	35	30	120	30	597.06
19	15	30	120	15	378
19	25	30	120	15	460.9
19	35	30	120	15	516.2
19	0	30	60	30	262
19	3	30	60	30	273
19	25	30	60	30	459.85
19	45	30	60	30	680
19	0	30	120	30	276
19	3	30	120	30	302
19	25	30	120	30	530
19	45	30	120	30	720
19	0	50	60	50	287
19	3	50	60	50	306
19	25	50	60	50	445
19	45	50	60	50	630
19	0	20	60	20	245
19	25	20	60	20	430
19	45	20	60	20	615
19	0	50	200	50	297
19	3	50	200	50	322
19	25	50	200	50	580
19	45	50	200	50	780

19	0	50	270	50	325
19	3	50	270	50	362
19	25	50	270	50	610
19	45	50	270	50	845
19	0	10	60	10	263
19	3	10	60	10	286
19	25	10	60	10	450
19	45	10	60	10	640
19	0	30	200	30	290
19	3	30	200	30	308
19	25	30	200	30	555
19	45	30	200	30	800
20	0	0	0	0	160.72
20	3	0	0	0	163.80
20	25	0	0	0	221.42
20	45	0	0	0	309.7
20	0	50	60	50	288.8
20	3	50	60	50	306.0
20	25	50	60	50	449.16
20	45	50	60	50	545.63
21	0	0	0	0	1257.8
21	0	1000	200	1000	1518.25
21	0	1000	500	1000	172.58
21	0	1000	700	1000	148.10
21	0	1000	1000	1000	128.62
21	0	1000	2000	1000	1054.25
21	0	1000	3000	1000	883.54

22	0	1000	1000	1000	361
22	0	1000	2000	1000	523
22	0	1000	4000	1000	814
22	0	1000	8000	1000	917
22	0	0	0	0	188
23	0	200	500	200	330
23	0	400	400	400	285
23	0	200	800	200	351
23	0	400	1600	400	499
23	0	0	0	0	154.80
24	0	0	0	0	181
24	0	1000	4000	2000	701
24	0	1000	2000	2000	445
24	0	1000	1000	2000	345
24	0	1000	500	2000	297
24	0	1000	4000	1000	803
24	0	1000	2000	1000	504
24	0	1000	1000	1000	378
24	0	1000	500	1000	301
24	0	1000	4000	500	983
24	0	1000	2000	500	693
24	0	1000	1000	500	489
24	0	1000	500	500	371
25	15	0	0	0	182.49
25	25	0	0	0	205.20
25	35	0	0	0	225.09
25	15	30	60	30	310.45

25	25	30	60	30	380.06
25	35	30	60	30	415.62
26	15	0	0	0	208.23
26	25	0	0	0	239.72
26	35	0	0	0	264.56
26	15	**30**	**60**	**45**	**380.11**
26	25	**30**	**60**	**45**	**462.95**
26	35	**30**	**60**	**45**	**553.13**

Note that the datasets marked in red and bold are the triangular distribution pattern of pillars.

REFERENCES

Abarzhi, S. I. (2010). Review of theoretical modelling approaches of Rayleigh-Taylor instabilities and turbulent mixing. *Philosophical Transactions of the Royal Society A: Mathematical, Physical and Engineering Sciences*, *368*(1916), 1809–1828. https://doi.org/10.1098/rsta.2010.0020

Abarzhi, S. I., & Rosner, R. (2010). A comparative study of approaches for modeling Rayleigh–Taylor turbulent mixing. *Physica Scripta*, *2010*(T142), 14012. Retrieved from http://stacks.iop.org/1402-4896/2010/i=T142/a=014012

Abdollahi, A., & Reza Salimpour, M. (2016). Experimental investigation on the boiling heat transfer of nanofluids on a flat plate in the presence of a magnetic field. *The European Physical Journal Plus*, *131*(11), 414. https://doi.org/10.1140/epjp/i2016-16414-x

Ahn, H. S., Sinha, N., Zhang, M., Banerjee, D., Fang, S., & Baughman, R. H. (2006). Pool Boiling Experiments on Multiwalled Carbon Nanotube (MWCNT) Forests. *Journal of Heat Transfer*, *128*(12), 1335. https://doi.org/10.1115/1.2349511

Alkhadra, M. A. (2017). Rayleigh-Taylor Instability. Retrieved from https://www.mohammadalkhadra.com/scientific-blog/copy-of-the-long-term-implications-of-crispr

Arik, M., & Bar-cohen, A. (2006). Effusivity-based correlation of surface property effects in pool boiling CHF of dielectric liquids. *International Journal of Heat and Mass Transfer*, *46*(2003), 3755–3764. https://doi.org/10.1016/S0017-9310(03)00215-1

Ayodeji, A., & Liu, Y. (2018). Support vector ensemble for incipient fault diagnosis in nuclear plant components. *Nuclear Engineering and Technology*. https://doi.org/https://doi.org/10.1016/j.net.2018.07.013

Bang, I. C., & Chang, S. H. (2005). Boiling heat transfer performance and phenomena of Al2O3–water nano-fluids from a plain surface in a pool. *International Journal of Heat and Mass Transfer*, *48*(12), 2407–2419. https://doi.org/https://doi.org/10.1016/j.ijheatmasstransfer.2004.12.047

Bar-Cohen, A., & McNeil, A. (1992). Parametric effects on pool boiling critical heat flux in dielectric liquids. In *Proceedings of the Engineering Foundation Conference on Pool and External Flow Boiling, ASME, Santa Barbara, CA* (Vol. 171175).

Baraldi, P., Razavi-Far, R., & Zio, E. (2011). Classifier-ensemble incremental-learning procedure for nuclear transient identification at different operational conditions. *Reliability Engineering & System Safety*, *96*(4), 480–488. https://doi.org/https://doi.org/10.1016/j.ress.2010.11.005

Barber, J.; Brutin, D.; Tadrist, L. (2011). A review on boiling heat transfer enhancement with nanofluids. *Nanoscale Research Letters*, *6*, 1–16. https://doi.org/https://doi.org/10.1186/1556-276X-6-280

Barisik, M., & Beskok, A. (2013). Wetting characterisation of silicon (1,0,0) surface. *Molecular Simulation*, *39*(9), 700–709. https://doi.org/10.1080/08927022.2012.758854

Bendu, H., Deepak, B. B. V. L., & Murugan, S. (2016). Application of GRNN for the prediction of performance and exhaust emissions in HCCI engine using ethanol. *Energy Conversion and Management*, *122*, 165–173.

https://doi.org/https://doi.org/10.1016/j.enconman.2016.05.061
Bergles, A. E., & Chyu, M. C. (1982). Characteristics of Nucleate Pool Boiling From Porous Metallic Coatings. *Journal of Heat Transfer*, *104*(2), 279. https://doi.org/10.1115/1.3245084
Bernath, L. (1960). A theory of local-boiling burnout and its application to existing data. *Chem. Eng. Progr.*, *56*(30).
Bhushan, B., & Chae Jung, Y. (2007). Wetting study of patterned surfaces for superhydrophobicity. *Ultramicroscopy*, *107*(10–11), 1033–1041. https://doi.org/10.1016/j.ultramic.2007.05.002
Bigham, S., Fazeli, A., & Moghaddam, S. (2017). Physics of microstructures enhancement of thin film evaporation heat transfer in microchannels flow boiling. *Scientific Reports*, *7*(November 2016), 1–11. https://doi.org/10.1038/srep44745
Boziuk, T. R., Smith, M. K., & Glezer, A. (2017). Enhanced boiling heat transfer on plain and featured surfaces using acoustic actuation. *International Journal of Heat and Mass Transfer*, *108*, 181–190. https://doi.org/10.1016/j.ijheatmasstransfer.2016.11.071
Brown, N. R., Ludewig, H., Aronson, A., Raitses, G., & Todosow, M. (2013). Neutronic evaluation of a PWR with fully ceramic microencapsulated fuel. Part II: Nodal core calculations and preliminary study of thermal hydraulic feedback. *Annals of Nuclear Energy*, *62*, 548–557. https://doi.org/https://doi.org/10.1016/j.anucene.2013.05.027
Bruder, M., Bloch, G., & Sattelmayer, T. (2017). Critical Heat Flux in Flow Boiling—Review of the Current Understanding and Experimental Approaches. *Heat Transfer Engineering*, *38*(3), 347–360. https://doi.org/10.1080/01457632.2016.1189274
Cahill, D. G., Ford, W. K., Goodson, K. E., Mahan, G. D., Majumdar, A., Maris, H. J., … Phillpot, S. R. (2003). Nanoscale thermal transport. *Journal of Applied Physics*, *93*(2), 793–818. https://doi.org/10.1063/1.1524305
Cai, J. (2012a). Applying support vector machine to predict the critical heat flux in concentric-tube open thermosiphon. *Annals of Nuclear Energy*, *43*, 114–122. https://doi.org/https://doi.org/10.1016/j.anucene.2011.12.029
Cai, J. (2012b). Predicting the critical heat flux in concentric-tube open thermosiphon: a method based on support vector machine optimized by chaotic particle swarm optimization algorithm. *Heat and Mass Transfer*, *48*(8), 1425–1435. https://doi.org/10.1007/s00231-012-0991-0
Cai, J., Huai, X., Liang, S., & Li, X. (2010). Augmentation of natural convective heat transfer by acoustic cavitation. *Frontiers of Energy and Power Engineering in China*, *4*(3), 313–318. https://doi.org/10.1007/s11708-009-0064-3
Cao, Z., Liu, B., Preger, C., Wu, Z., Zhang, Y., Wang, X., … Sundén, B. (2018a). Pool boiling heat transfer of FC-72 on pin-fin silicon surfaces with nanoparticle deposition. *International Journal of Heat and Mass Transfer*, *126*, 1019–1033. https://doi.org/10.1016/j.ijheatmasstransfer.2018.05.033
Cao, Z., Liu, B., Preger, C., Wu, Z., Zhang, Y., Wang, X., … Sundén, B. (2018b). Pool boiling heat transfer of FC-72 on pin-fin silicon surfaces with nanoparticle deposition. *International Journal of Heat and Mass Transfer*, *126*, 1019–1033. https://doi.org/10.1016/j.ijheatmasstransfer.2018.05.033
Chang, J. Y., & You, S. M. (1996). Heater Orientation Effects on Pool Boiling of Micro-Porous-Enhanced Surfaces in Saturated FC-72. *Journal of Heat Transfer*, *118*(4),

937–943. Retrieved from http://dx.doi.org/10.1115/1.2822592
Chelgani, S. C., & Jorjani, E. (2011). Microwave irradiation pretreatment and peroxyacetic acid desulfurization of coal and application of GRNN simultaneous predictor. *Fuel*, *90*(11), 3156–3163. https://doi.org/https://doi.org/10.1016/j.fuel.2011.06.045
Chen, R., Lu, M., Srinivasan, V., Wang, Z., Cho, H. H., & Majumdar, A. (2009). Nanowires for Enhanced Boiling Heat Transfer 2009. *Nano Letters*, *9*(2), 548–553. https://doi.org/10.1021/nl8026857
Chen, Y., Mo, D., Zhao, H., Ding, N., & Lu, S. (2009). Pool boiling on the superhydrophilic surface with TiO2 nanotube arrays. *Science in China Series E: Technological Sciences*, *52*(6), 1596–1600. https://doi.org/10.1007/s11431-009-0195-0
Choi, J. Y., & No, H. C. (2015). Development of CHF Mapping Method for Fin Structured Surface, 113–126.
Choi, J. Y., & No, H. C. (2016). Development of a critical heat flux mapping method for fin-structured surfaces. *Journal of Nuclear Science and Technology*, *53*(9), 1321–1331. https://doi.org/10.1080/00223131.2015.1105165
Chu, K.-H., Enright, R., & Wang, E. (2011). Microstructured surfaces for enhanced pool boiling heat transfer. *Imeche 2011*, *100*(24), 241603.
Chu, K., Enright, R., Wang, E. N., Chu, K., Enright, R., & Wang, E. N. (2013). Structured surfaces for enhanced pool boiling heat transfer Structured surfaces for enhanced pool boiling heat transfer, *241603*(2012), 10–14. https://doi.org/10.1063/1.4724190
Chu, K. H., Joung, Y. S., Enright, R., Buie, C. R., & Wang, E. N. (2013). Hierarchically structured surfaces for boiling critical heat flux enhancement. *Applied Physics Letters*, *102*(15). https://doi.org/10.1063/1.4801811
Cole, R. (n.d.). Bubble frequencies and departure volumes at subatmospheric pressures. *AIChE Journal*, *13*(4), 779–783. https://doi.org/10.1002/aic.690130434
Cole, R., & Shulman, H. L. (1966). Critical heat flux values at sub-atmospheric pressures. *Chemical Engineering Science*, *21*(8), 723–724. https://doi.org/https://doi.org/10.1016/0009-2509(66)80027-1
Dasgupta, A., Chandraker, D. K., Nayak, A. K., & Vijayan, P. K. (2015). Prediction of Vapor Film Thickness Below a Leidenfrost Drop. *Journal of Heat Transfer*, *137*(12), 124501–124505. Retrieved from http://dx.doi.org/10.1115/1.4030909
de Gennes, P.-G., Francoise, Brochard-Wyart, & Quere, D. (2004). *Capillarity and Wetting Phenomena: Drops, Bubbles, Pearls, Waves*. (F. Bonamy, Ed.) (1st ed.). New York: Springer-Verlag New York. https://doi.org/10.1007/978-0-387-21656-0
Dong, L., Quan, X., & Cheng, P. (2014a). An experimental investigation of enhanced pool boiling heat transfer from surfaces with micro/nano-structures. *International Journal of Heat and Mass Transfer*, *71*, 189–196. https://doi.org/10.1016/j.ijheatmasstransfer.2013.11.068
Dong, L., Quan, X., & Cheng, P. (2014b). An experimental investigation of enhanced pool boiling heat transfer from surfaces with micro/nano-structures. *International Journal of Heat and Mass Transfer*, *71*, 189–196. https://doi.org/10.1016/j.ijheatmasstransfer.2013.11.068
Douglas, Z. W., Smith, M. K., & Glezer, A. (2007). Acoustically enhanced boiling heat

transfer. *Collection of Papers Presented at The 13th International Workshop on THERMal INvestigation of ICs and Systems, THERMINIC*, *052105*(2012), 145–149. https://doi.org/10.1109/THERMINIC.2007.4451767

El-Genk, M. S., & Ali, A. F. (2010). Enhanced nucleate boiling on copper micro-porous surfaces. *International Journal of Multiphase Flow*, *36*(10), 780–792. https://doi.org/https://doi.org/10.1016/j.ijmultiphaseflow.2010.06.003

Esfe, M. H., Rejvani, M., Karimpour, R., & Abbasian Arani, A. A. (2017). Estimation of thermal conductivity of ethylene glycol-based nanofluid with hybrid suspensions of SWCNT–Al2O3nanoparticles by correlation and ANN methods using experimental data. *Journal of Thermal Analysis and Calorimetry*, *128*(3), 1359–1371. https://doi.org/10.1007/s10973-016-6002-9

Extrand, C. W. (2016). Remodeling of Super-hydrophobic Surfaces. *Langmuir*, *32*(34), 8608–8612. https://doi.org/10.1021/acs.langmuir.6b02292

Ferjančič, K., & Golobič, I. (2002). Surface effects on pool boiling CHF. *Experimental Thermal and Fluid Science*, *25*(7), 565–571. https://doi.org/https://doi.org/10.1016/S0894-1777(01)00104-2

Giri Nandagopal, M. S., & Selvaraju, N. (2016). Prediction of Liquid–Liquid Flow Patterns in a Y-Junction Circular Microchannel Using Advanced Neural Network Techniques. *Industrial & Engineering Chemistry Research*, *55*(43), 11346–11362. https://doi.org/10.1021/acs.iecr.6b02438

Gogonin, I. I., & Kutateladze, S. S. (1977). Critical heat flux as a function of heater size for a liquid boiling in a large enclosure. *Journal of Engineering Physics*, *33*(5), 1286–1289. https://doi.org/10.1007/BF00860899

Golobič, I., & Bergles, A. E. (1997). Effects of heater-side factors on the saturated pool boiling critical heat flux. *Experimental Thermal and Fluid Science*, *15*(1), 43–51. https://doi.org/https://doi.org/10.1016/S0894-1777(96)00170-7

Golobič, I., & Ferjančič, K. (2000). Role of enhanced coated surface in pool boiling CHF in FC-72. *Heat and Mass Transfer/Waerme- Und Stoffuebertragung*. https://doi.org/10.1007/s002310000118

Goodfellow, I., McDaniel, P., & Papernot, N. (2018). Making machine learning robust against adversarial inputs. *Communications of the ACM*, *61*(7), 56–66. https://doi.org/10.1145/3134599

Groeneveld, D. C., Shan, J. Q., Vasić, A. Z., Leung, L. K. H., Durmayaz, A., Yang, J., … Tanase, A. (2007). The 2006 CHF look-up table. *Nuclear Engineering and Design*, *237*(15), 1909–1922. https://doi.org/https://doi.org/10.1016/j.nucengdes.2007.02.014

Guan, C. K., Bon, B., Klausner, J., & Mei, R. (2014). Comparison of CHF enhancement on microstructured surfaces with a predictive model. *Heat Transfer Engineering*, *35*(5), 452–460. https://doi.org/10.1080/01457632.2013.833043

Guan, C. K., Klausner, J. F., & Mei, R. (2011). A new mechanistic model for pool boiling CHF on horizontal surfaces. *International Journal of Heat and Mass Transfer*, *54*(17–18), 3960–3969. https://doi.org/10.1016/j.ijheatmasstransfer.2011.04.029

Guglielmini, G., & Nannei, E. (1976). On the effect of heating wall thickness on pool boiling burnout. *International Journal of Heat and Mass Transfer*, *19*(9), 1073–1075. https://doi.org/https://doi.org/10.1016/0017-9310(76)90191-5

Ha, M., & Graham, S. (2017). Pool boiling characteristics and critical heat flux mechanisms of microporous surfaces and enhancement through structural modification. *Applied Physics Letters*, *111*(9), 91601. https://doi.org/10.1063/1.4999158

Hale, R. S., Ranjan, R., & Hidrovo, C. H. (2014a). Capillary flow through rectangular micropillar arrays. *International Journal of Heat and Mass Transfer*, *75*, 710–717. https://doi.org/10.1016/j.ijheatmasstransfer.2014.04.016

Hale, R. S., Ranjan, R., & Hidrovo, C. H. (2014b). Capillary flow through rectangular micropillar arrays. *International Journal of Heat and Mass Transfer*, *75*, 710–717. https://doi.org/10.1016/j.ijheatmasstransfer.2014.04.016

Hanlon, M. A., & Ma, H. B. (2003). Evaporation Heat Transfer in Sintered Porous Media. *Journal of Heat Transfer*, *125*(4), 644. https://doi.org/10.1115/1.1560145

He, M., & Lee, Y. (2018). Application of machine learning for prediction of critical heat flux: Support vector machine for data-driven CHF look-up table construction based on sparingly distributed training data points. *Nuclear Engineering and Design*, *338*, 189–198. https://doi.org/https://doi.org/10.1016/j.nucengdes.2018.08.005

Henry, C. D., & Kim, J. (2005). Thermocapillary effects on low-g Pool Boiling from microheater arrays of various aspect ratio. *Microgravity - Science and Technology*, *16*(1), 170. https://doi.org/10.1007/BF02945970

Henry, C. D., Kim, J., Chamberlain, B., & Hartman, T. G. (2005). Heater size and heater aspect ratio effects on subcooled pool boiling heat transfer in low-g. *Experimental Thermal and Fluid Science*, *29*(7), 773–782. https://doi.org/https://doi.org/10.1016/j.expthermflusci.2005.03.003

Hinton, G. E., & Salakhutdinov, R. R. (2006). Reducing the dimensionality of data with neural networks. *Science*, *313*(5786), 504–507. https://doi.org/10.1126/science.1127647

Ho, J. Y., Wong, K. K., & Leong, K. C. (2016). Saturated pool boiling of FC-72 from enhanced surfaces produced by Selective Laser Melting. *International Journal of Heat and Mass Transfer*, *99*, 107–121. https://doi.org/10.1016/j.ijheatmasstransfer.2016.03.073

Honda, H., Takamastu, H., & Wei, J. J. (2002a). Enhanced Boiling of FC-72 on Silicon Chips With Micro-Pin-Fins and Submicron-Scale Roughness. *Journal of Heat Transfer*, *124*(2), 383. https://doi.org/10.1115/1.1447937

Honda, H., Takamastu, H., & Wei, J. J. (2002b). Enhanced Boiling of FC-72 on Silicon Chips With Micro-Pin-Fins and Submicron-Scale Roughness. *Journal of Heat Transfer*, *124*(2), 383. https://doi.org/10.1115/1.1447937

Howard, A. H., & Mudawar, I. (1999). Orientation effects on pool boiling critical heat flux (CHF) and modeling of CHF for near-vertical surfaces. *International Journal of Heat and Mass Transfer*, *42*(9), 1665–1688. https://doi.org/10.1016/S0017-9310(98)00233-6

Im, Y., Joshi, Y., Dietz, C., & Lee, S. S. (2010). Enhanced Boiling of a Dielectric Liquid on Copper Nanowire Surfaces. *International Journal of Micro-Nano Scale Transport*, *1*(1), 79–96. https://doi.org/10.1260/1759-3093.1.1.79

Jeong, J. H., & Kwon, Y. C. (2006). Effects of ultrasonic vibration on subcooled pool boiling critical heat flux. *Heat and Mass Transfer/Waerme- Und Stoffuebertragung*, *42*(12), 1155–1161. https://doi.org/10.1007/s00231-005-0079-1

Jiang, B. T., Ren, J. S., Hu, P., & Zhao, F. Y. (2013). Prediction of critical heat flux for water flow in vertical round tubes using support vector regression model. *Progress in Nuclear Energy*, *68*, 210–222. https://doi.org/10.1016/j.pnucene.2013.07.004

Jiang, B. T., & Zhao, F. Y. (2013a). Combination of support vector regression and artificial neural networks for prediction of critical heat flux. *International Journal of Heat and Mass Transfer*, *62*(1), 481–494. https://doi.org/10.1016/j.ijheatmasstransfer.2013.03.025

Jiang, B. T., & Zhao, F. Y. (2013b). Particle swarm optimization-based least squares support vector regression for critical heat flux prediction. *Annals of Nuclear Energy*, *53*, 69–81. https://doi.org/10.1016/j.anucene.2012.09.020

Kam, D. H., Choi, Y. J., & Jeong, Y. H. (2018). International Journal of Heat and Mass Transfer CHF experiment with downward-facing carbon and stainless steel plates under pressurized conditions. *International Journal of Heat and Mass Transfer*, *125*, 670–680. https://doi.org/10.1016/j.ijheatmasstransfer.2018.04.026

Kamel, M., & Lezsovits, F. (2017). Boiling heat transfer of nanofluids: A review of recent studies. *Thermal Science*, (00), 216–216. https://doi.org/10.2298/TSCI170419216K

Kamel, M. S., Lezsovits, F., Hussein, A. M., Mahian, O., & Wongwises, S. (2018). Latest developments in boiling critical heat flux using nanofluids: A concise review. *International Communications in Heat and Mass Transfer*, *98*, 59–66. https://doi.org/10.1016/j.icheatmasstransfer.2018.08.009

Kandlikar, S. G. (2001a). A Theoretical Model to Predict Pool Boiling CHF Incorporating Effects of Contact Angle and Orientation. *Journal of Heat Transfer*, *123*(6), 1071. https://doi.org/10.1115/1.1409265

Kandlikar, S. G. (2001b). A Theoretical Model to Predict Pool Boiling CHF Incorporating Effects of Contact Angle and Orientation. *Journal of Heat Transfer*, *123*(6), 1071. https://doi.org/10.1115/1.1409265

Kandlikar, S. G. (2002). Fundamental issues related to flow boiling in minichannels and microchannels. *Experimental Thermal and Fluid Science*, *26*(2), 389–407. https://doi.org/https://doi.org/10.1016/S0894-1777(02)00150-4

Kang, J., Kim, T. K., Lee, G. C., Kim, M. H., & Park, H. S. (2018). Quenching of candidate materials for accident tolerant fuel-cladding in LWRs. *Annals of Nuclear Energy*, *112*, 794–807. https://doi.org/https://doi.org/10.1016/j.anucene.2017.11.007

Kathiravan, R., Kumar, R., Gupta, A., Chandra, R., & Jain, P. K. (2011). Pool boiling characteristics of multiwalled carbon nanotube (CNT) based nanofluids over a flat plate heater. *International Journal of Heat and Mass Transfer*, *54*(5–6), 1289–1296. https://doi.org/10.1016/j.ijheatmasstransfer.2010.10.002

Khanikar, V., Mudawar, I., & Fisher, T. (2009). Effects of carbon nanotube coating on flow boiling in a micro-channel. *International Journal of Heat and Mass Transfer*, *52*(15–16), 3805–3817. https://doi.org/10.1016/j.ijheatmasstransfer.2009.02.007

Kim, B. J., Lee, J. H., & Kim, K. D. (2015). Rayleigh-Taylor instability for thin viscous gas films: Application to critical heat flux and minimum film boiling. *International Journal of Heat and Mass Transfer*, *80*, 150–158. https://doi.org/10.1016/j.ijheatmasstransfer.2014.08.084

Kim, B. J., Lee, J. H., & Kim, K. D. (2016). Improvements of critical heat flux models for pool boiling on horizontal surfaces using interfacial instabilities of viscous

potential flows. *International Journal of Heat and Mass Transfer*, *93*, 200–206. https://doi.org/10.1016/j.ijheatmasstransfer.2015.10.012
Kim, B. S., Choi, G., Shin, S., Gemming, T., & Cho, H. H. (2016). Nano-inspired fluidic interactivity for boiling heat transfer: Impact and criteria. *Scientific Reports*, *6*, 1–11. https://doi.org/10.1038/srep34348
Kim, B. S., Lee, H., Shin, S., Choi, G., & Cho, H. H. (2014). Interfacial wicking dynamics and its impact on critical heat flux of boiling heat transfer. *Applied Physics Letters*, *105*(19). https://doi.org/10.1063/1.4901569
Kim, B. S., Shin, S., Lee, D., Choi, G., Lee, H., Kim, K. M., & Cho, H. H. (2014). Stable and uniform heat dissipation by nucleate-catalytic nanowires for boiling heat transfer. *International Journal of Heat and Mass Transfer*, *70*, 23–32. https://doi.org/10.1016/j.ijheatmasstransfer.2013.10.061
Kim, D. E., Yu, D. I., Park, S. C., Kwak, H. J., & Ahn, H. S. (2015). Critical heat flux triggering mechanism on micro-structured surfaces: Coalesced bubble departure frequency and liquid furnishing capability. *International Journal of Heat and Mass Transfer*, *91*, 1237–1247. https://doi.org/10.1016/j.ijheatmasstransfer.2015.08.065
Kim, E. S., Jung, J. Y., & Kang, Y. T. (2013). The effect of surface area on pool boiling heat transfer coefficient and CHF of Al2O3/water nanofluids. *Journal of Mechanical Science and Technology*, *27*(10), 3177–3182. https://doi.org/10.1007/s12206-013-0839-7
Kim, H. C., Baek, W.-P., & Chang, S. H. (2000). Critical heat flux of water in vertical round tubes at low pressure and low flow conditions. *Nuclear Engineering and Design*, *199*(1), 49–73. https://doi.org/https://doi.org/10.1016/S0029-5493(99)00074-6
Kim, H., & Kim, M. (2009). Experimental study of the characteristics and mechanism of pool boiling CHF enhancement using nanofluids. *Heat and Mass Transfer/Waerme-Und Stoffuebertragung*, *45*(7), 991–998. https://doi.org/10.1007/s00231-007-0318-8
Kim, J. M., Kong, B., Lee, H.-B.-R., Wongwises, S., & Ahn, H. S. (2018). Effect of h-BN coating on nucleate boiling heat transfer performance in pool boiling. *Experimental Thermal and Fluid Science*, *98*, 12–19. https://doi.org/https://doi.org/10.1016/j.expthermflusci.2018.05.010
Kim, J. M., Park, S. C., Kong, B. T., Lee, H. B. R., & Ahn, H. S. (2018a). Effect of porous graphene networks and micropillar arrays on boiling heat transfer performance. *Experimental Thermal and Fluid Science*, *93*, 153–164. https://doi.org/10.1016/j.expthermflusci.2017.12.029
Kim, J. M., Park, S. C., Kong, B. T., Lee, H. B. R., & Ahn, H. S. (2018b). Effect of porous graphene networks and micropillar arrays on boiling heat transfer performance. *Experimental Thermal and Fluid Science*, *93*, 153–164. https://doi.org/10.1016/j.expthermflusci.2017.12.029
Kim, S. B. J., Kim, Y. H., Noh, S. W., Suh, K. Y., Rempe, J. L., & Cheung, F. B. (2003). Experimental Study of Critical Heat Flux in Inclined Rectangular Gap. In *GENES4/ANP2003* (pp. 15–19). kyoto, Japan.
Kim, S. H., Kang, J. Y., Kiyofumi, M., Park, H. S., Hwan, M., & Lee, G. C. (2015). Roles of Boiling Surface Characterized by Micro-structures on Boiling Heat Transfer and Critical Heat Flux. *Nureth-16*, 4826–4837.
Kim, S. H., Lee, G. C., Kang, J. Y., Moriyama, K., Kim, M. H., & Park, H. S. (2015a).

Boiling heat transfer and critical heat flux evaluation of the pool boiling on micro structured surface. *International Journal of Heat and Mass Transfer*, *91*, 1140–1147. https://doi.org/10.1016/j.ijheatmasstransfer.2015.07.120

Kim, S. H., Lee, G. C., Kang, J. Y., Moriyama, K., Kim, M. H., & Park, H. S. (2015b). Boiling heat transfer and critical heat flux evaluation of the pool boiling on micro structured surface. *International Journal of Heat and Mass Transfer*, *91*, 1140–1147. https://doi.org/10.1016/j.ijheatmasstransfer.2015.07.120

Kim, S. H., Lee, G. C., Kang, J. Y., Moriyama, K., Park, H. S., & Kim, M. H. (2016a). Heat flux partitioning analysis of pool boiling on micro structured surface using infrared visualization. *International Journal of Heat and Mass Transfer*, *102*, 756–765. https://doi.org/10.1016/j.ijheatmasstransfer.2016.06.040

Kim, S. H., Lee, G. C., Kang, J. Y., Moriyama, K., Park, H. S., & Kim, M. H. (2016b). Heat flux partitioning analysis of pool boiling on micro structured surface using infrared visualization. *International Journal of Heat and Mass Transfer*, *102*, 756–765. https://doi.org/10.1016/j.ijheatmasstransfer.2016.06.040

Kim, S., Kim, H. D., Kim, H., Ahn, H. S., Jo, H., Kim, J., & Kim, M. H. (2010). Effects of nano-fluid and surfaces with nano structure on the increase of CHF. *Experimental Thermal and Fluid Science*, *34*(4), 487–495. https://doi.org/10.1016/j.expthermflusci.2009.05.006

Kong, X., Wei, J., Deng, Y., & Zhang, Y. (2017). A Study on Enhancement of Boiling Heat Transfer by Mixed-Wettability Surface A Study on Enhancement of Boiling Heat Transfer by Mixed-Wettability Surface, *7632*. https://doi.org/10.1080/01457632.2017.1369845

Kong, X., Zhang, Y., & Wei, J. (2018a). Experimental study of pool boiling heat transfer on novel bistructured surfaces based on micro-pin-finned structure. *Experimental Thermal and Fluid Science*, *91*(August 2017), 9–19. https://doi.org/10.1016/j.expthermflusci.2017.09.021

Kong, X., Zhang, Y., & Wei, J. (2018b). Experimental study of pool boiling heat transfer on novel bistructured surfaces based on micro-pin-finned structure. *Experimental Thermal and Fluid Science*, *91*(August 2017), 9–19. https://doi.org/10.1016/j.expthermflusci.2017.09.021

Krawczyk, B., Minku, L. L., Gama, J., Stefanowski, J., & Woźniak, M. (2017). Ensemble learning for data stream analysis: A survey. *Information Fusion*, *37*, 132–156. https://doi.org/https://doi.org/10.1016/j.inffus.2017.02.004

Kumar, N., Urkude, N., Sonawane, S. S., & Sonawane, S. H. (2018). Experimental study on pool boiling and Critical Heat Flux enhancement of metal oxides based nanofluid. *International Communications in Heat and Mass Transfer*, *96*(June), 37–42. https://doi.org/10.1016/j.icheatmasstransfer.2018.05.018

Kwark, S. M., Amaya, M., Kumar, R., Moreno, G., & You, S. M. (2010). Effects of pressure, orientation, and heater size on pool boiling of water with nanocoated heaters. *International Journal of Heat and Mass Transfer*, *53*(23), 5199–5208. https://doi.org/https://doi.org/10.1016/j.ijheatmasstransfer.2010.07.040

Lee, J., & Chang, S. H. (2012). An experimental study on CHF in pool boiling system with SA508 test heater under atmospheric pressure. *Nuclear Engineering and Design*, *250*, 720–724. https://doi.org/10.1016/j.nucengdes.2012.05.024

Lee, J., & Mudawar, I. (2009). Critical heat flux for subcooled flow boiling in micro-

channel heat sinks. *International Journal of Heat and Mass Transfer*, *52*(13), 3341–3352. https://doi.org/https://doi.org/10.1016/j.ijheatmasstransfer.2008.12.019
Lee, M. (2000). A critical heat flux approach for square rod bundles using the 1995 Groeneveld CHF table and bundle data of heat transfer research facility. *Nuclear Engineering and Design*, *197*(3), 357–374. https://doi.org/https://doi.org/10.1016/S0029-5493(99)00294-0
Lee, M. H., Heo, H., & Bang, I. C. (2018). Effect of thermal activity on critical heat flux enhancement in downward-hemispherical surface using graphene oxide coating. *International Journal of Heat and Mass Transfer*, *127*, 1102–1111. https://doi.org/https://doi.org/10.1016/j.ijheatmasstransfer.2018.07.151
Lee, S., & Chien, L. (2011a). Experimental Study of Pool Boiling on Pin-Finned and Straight-Finned Surfaces on an Inclined Plate in FC-72. *Journal of Enhanced Heat Transfer*, *18*(4), 311–324. https://doi.org/10.1615/JEnhHeatTransf.v18.i4.50
Lee, S., & Chien, L. (2011b). Experimental Study of Pool Boiling on Pin-Finned and Straight-Finned Surfaces on an Inclined Plate in FC-72. *Journal of Enhanced Heat Transfer*, *18*(4), 311–324. https://doi.org/10.1615/JEnhHeatTransf.v18.i4.50
Lee, Y., & Kazimi, M. S. (2015). A structural model for multi-layered ceramic cylinders and its application to silicon carbide cladding of light water reactor fuel. *Journal of Nuclear Materials*, *458*, 87–105. https://doi.org/https://doi.org/10.1016/j.jnucmat.2014.12.013
Lee, Y., McKrell, T. J., Yue, C., & Kazimi, M. S. (2013). Safety Assessment of SiC Cladding Oxidation under Loss-of-Coolant Accident Conditions in Light Water Reactors. *Nuclear Technology*, *183*(2), 210–227. https://doi.org/10.13182/NT12-122
Lee, Y., NO, H. C., & Lee, J. I. (2017). Design optimization of multi-layer Silicon Carbide cladding for light water reactors. *Nuclear Engineering and Design*, *311*, 213–223. https://doi.org/https://doi.org/10.1016/j.nucengdes.2016.11.016
Legay, M., Gondrexon, N., Le Person, S., Boldo, P., & Bontemps, A. (2011). Enhancement of heat transfer by ultrasound: Review and recent advances. *International Journal of Chemical Engineering*, *2011*. https://doi.org/10.1155/2011/670108
Leong, K. C., Ho, J. Y., & Wong, K. K. (2017). A critical review of pool and flow boiling heat transfer of dielectric fluids on enhanced surfaces. *Applied Thermal Engineering*, *112*, 999–1019. https://doi.org/10.1016/j.applthermaleng.2016.10.138
Li, F., Zhang, J., Shang, C., Huang, D., Oko, E., & Wang, M. (2018). Modelling of a post-combustion CO2capture process using deep belief network. *Applied Thermal Engineering*, *130*, 997–1003. https://doi.org/10.1016/j.applthermaleng.2017.11.078
Li, R., & Huang, Z. (2017). A new CHF model for enhanced pool boiling heat transfer on surfaces with micro-scale roughness. *International Journal of Heat and Mass Transfer*, *109*, 1084–1093. https://doi.org/10.1016/j.ijheatmasstransfer.2017.02.089
Liang, G., & Mudawar, I. (2018a). Pool boiling critical heat flux (CHF) – Part 1: Review of mechanisms, models, and correlations. *International Journal of Heat and Mass Transfer*, *117*, 1352–1367. https://doi.org/10.1016/j.ijheatmasstransfer.2017.09.134
Liang, G., & Mudawar, I. (2018b). Pool boiling critical heat flux (CHF) – Part 1: Review of mechanisms, models, and correlations. *International Journal of Heat and Mass Transfer*, *117*, 1352–1367. https://doi.org/10.1016/j.ijheatmasstransfer.2017.09.134
Lienhard, J., & Dhir, V. K. (1972). Hydrodynamic Prediction of Peak Pool-boiling Heat

Fluxes from Finite Bodies. *Journal of Heat Transfer, Transactions ASME*, *95*. https://doi.org/10.1115/1.3450013

Lienhard, J. H., & Dhir, V. K. (1973a). Hydrodynamic Prediction of Peak Pool-boiling Heat Fluxes from Finite Bodies. *Journal of Heat Transfer*, *95*(2), 152–158. Retrieved from http://dx.doi.org/10.1115/1.3450013

Lienhard, J. H., & Dhir, V. K. (1973b). Hydrodynamic Prediction of Peak Pool-boiling Heat Fluxes from Finite Bodies. *Journal of Heat Transfer*, *95*(2), 152–158.

Lu, M.-C., Chen, R., Srinivasan, V., Carey, V. P., & Majumdar, A. (2011). Critical heat flux of pool boiling on Si nanowire array-coated surfaces. *International Journal of Heat and Mass Transfer*, *54*(25), 5359–5367. https://doi.org/https://doi.org/10.1016/j.ijheatmasstransfer.2011.08.007

Lu, M. C., Huang, C. H., Huang, C. Te, & Chen, Y. C. (2015a). A modified hydrodynamic model for pool boiling CHF considering the effects of heater size and nucleation site density. *International Journal of Thermal Sciences*, *91*, 133–141. https://doi.org/10.1016/j.ijthermalsci.2015.01.011

Lu, M. C., Huang, C. H., Huang, C. Te, & Chen, Y. C. (2015b). A modified hydrodynamic model for pool boiling CHF considering the effects of heater size and nucleation site density. *International Journal of Thermal Sciences*, *91*, 133–141. https://doi.org/10.1016/j.ijthermalsci.2015.01.011

Magrini, U., & Nannei, E. (1975). On the Influence of the Thickness and Thermal Properties of Heating Walls on the Heat Transfer Coefficients in Nucleate Pool Boiling. *Journal of Heat Transfer*, *97*(2), 173–178. Retrieved from http://dx.doi.org/10.1115/1.3450337

Mai, T. T., Lai, C. Q., Zheng, H., Balasubramanian, K., Leong, K. C., Lee, P. S., … Choi, W. K. (2012). Dynamics of wicking in silicon nanopillars fabricated with interference lithography and metal-assisted chemical etching. *Langmuir*, *28*(31), 11465–11471. https://doi.org/10.1021/la302262g

McHale, J. P., Garimella, S. V., Fisher, T. S., & Powell, G. A. (2011). Pool boiling performance comparison of smooth and sintered copper surfaces with and without carbon nanotubes. *Nanoscale and Microscale Thermophysical Engineering*, *15*(3), 133–150. https://doi.org/10.1080/15567265.2011.575918

Mei, Y., Shao, Y., Gong, S., Zhu, Y., & Gu, H. (2018a). Effects of surface orientation and heater material on heat transfer coefficient and critical heat flux of nucleate boiling. *International Journal of Heat and Mass Transfer*, *121*, 632–640. https://doi.org/10.1016/j.ijheatmasstransfer.2018.01.020

Mei, Y., Shao, Y., Gong, S., Zhu, Y., & Gu, H. (2018b). Effects of surface orientation and heater material on heat transfer coefficient and critical heat flux of nucleate boiling. *International Journal of Heat and Mass Transfer*, *121*, 632–640. https://doi.org/10.1016/j.ijheatmasstransfer.2018.01.020

Misale, M., Guglielmini, G., & Priarone, A. (2009). HFE-7100 pool boiling heat transfer and critical heat flux in inclined narrow spaces. *International Journal of Refrigeration*, *32*(2), 235–245. https://doi.org/https://doi.org/10.1016/j.ijrefrig.2008.06.003

Moon, H. W., Yoon, Y. J., Park, J. H., Myung, B. S., & Kim, D. E. (2016). Dynamic wetting and boiling characteristics on micro-structured and micro/nano hierarchically structured surfaces. *Experimental Thermal and Fluid Science*, *74*, 19–

26. https://doi.org/10.1016/j.expthermflusci.2015.11.019
Mori, S., & Utaka, Y. (2017). Critical heat flux enhancement by surface modification in a saturated pool boiling: A review. *International Journal of Heat and Mass Transfer*, *108*, 2534–2557. https://doi.org/10.1016/j.ijheatmasstransfer.2017.01.090
Mukherjee, S., Datta, S., & Kumar Das, A. (2018). Molecular Dynamic Study of Boiling Heat Transfer Over Structured Surfaces. *Journal of Heat Transfer*, *140*(5), 54503–54505. Retrieved from http://dx.doi.org/10.1115/1.4038480
Ndao, S., Peles, Y., & Jensen, M. K. (2014). Effects of pin fin shape and configuration on the single-phase heat transfer characteristics of jet impingement on micro pin fins. *International Journal of Heat and Mass Transfer*, *70*, 856–863. https://doi.org/10.1016/j.ijheatmasstransfer.2013.11.062
Nguyen, T. B., Liu, D., Kayes, M. I., Wang, B., Rashin, N., Leu, P. W., & Tran, T. (2018). Critical heat flux enhancement in pool boiling through increased rewetting on nanopillar array surfaces. *Scientific Reports*, *8*(1), 1–9. https://doi.org/10.1038/s41598-018-22693-z
Ni, Y. Q., & Li, M. (2016). Wind pressure data reconstruction using neural network techniques: A comparison between BPNN and GRNN. *Measurement*, *88*, 468–476. https://doi.org/https://doi.org/10.1016/j.measurement.2016.04.049
Park, K.-A., & Bergles, A. E. (1988). Effects of Size of Simulated Microelectronic Chips on Boiling and Critical Heat Flux. *Journal of Heat Transfer*, *110*(3), 728–734. Retrieved from http://dx.doi.org/10.1115/1.3250552
Park, K. J., Jung, D., & Shim, S. E. (2009). Nucleate boiling heat transfer in aqueous solutions with carbon nanotubes up to critical heat fluxes. *International Journal of Multiphase Flow*, *35*(6), 525–532. https://doi.org/10.1016/j.ijmultiphaseflow.2009.02.015
Park, S. D., & Bang, I. C. (2014). Experimental study of a universal CHF enhancement mechanism in nanofluids using hydrodynamic instability. *International Journal of Heat and Mass Transfer*, *70*, 844–850. https://doi.org/10.1016/j.ijheatmasstransfer.2013.11.066
Park, Y., Kim, H., Kim, J., & Kim, H. (2016). Measurement of liquid-vapor phase distribution on nano- and microstructured boiling surfaces. *International Journal of Multiphase Flow*, *81*, 67–76. https://doi.org/10.1016/j.ijmultiphaseflow.2016.01.007
Quan, X., Dong, L., & Cheng, P. (2014). A CHF model for saturated pool boiling on a heated surface with micro/nano-scale structures. *International Journal of Heat and Mass Transfer*, *76*, 452–458. https://doi.org/10.1016/j.ijheatmasstransfer.2014.04.037
Raghupathi, P. A., & Kandlikar, S. G. (2018). Effect of Thermophysical Properties of the Heater Substrate on Critical Heat Flux in Pool Boiling, *139*(November 2017), 1–7. https://doi.org/10.1115/1.4036653
Rahman, M. M., Ölçeroglu, E., & McCarthy, M. (2014). Role of wickability on the critical heat flux of structured superhydrophilic surfaces. *Langmuir*, *30*(37), 11225–11234. https://doi.org/10.1021/la5030923
Rainey, K. N., & You, S. M. (2000a). Pool Boiling Heat Transfer From Plain and Microporous, Square Pin-Finned Surfaces in Saturated FC-72. *Journal of Heat Transfer*, *122*(3), 509. https://doi.org/10.1115/1.1288708
Rainey, K. N., & You, S. M. (2000b). Pool Boiling Heat Transfer From Plain and

Microporous, Square Pin-Finned Surfaces in Saturated FC-72. *Journal of Heat Transfer*, *122*(3), 509. https://doi.org/10.1115/1.1288708

Rainey, K. N., & You, S. M. (2001). Effects of heater size and orientation on pool boiling heat transfer from microporous coated surfaces. *International Journal of Heat and Mass Transfer*, *44*(14), 2589–2599. https://doi.org/10.1016/S0017-9310(00)00318-5

Rainey, K. N., You, S. M., & Lee, S. (2003). Effect of pressure, subcooling, and dissolved gas on pool boiling heat transfer from microporous, square pin-finned surfaces in FC-72. *International Journal of Heat and Mass Transfer*, *46*(1), 23–35. https://doi.org/10.1016/S0017-9310(02)00257-0

Rajvanshi, A. K., Saini, J. S., & Prakash, R. (1992). Investigation of macrolayer thickness in nucleate pool boiling at high heat flux. *International Journal of Heat and Mass Transfer*, *35*(2), 343–350. https://doi.org/https://doi.org/10.1016/0017-9310(92)90272-T

Rishi, A. M., Gupta, A., & Kandlikar, S. G. (2018). Improving aging performance of electrodeposited copper coatings during pool boiling. *Applied Thermal Engineering*, *140*(April), 406–414. https://doi.org/10.1016/j.applthermaleng.2018.05.061

Rooki, R. (2016). Application of general regression neural network (GRNN) for indirect measuring pressure loss of Herschel–Bulkley drilling fluids in oil drilling. *Measurement*, *85*, 184–191. https://doi.org/https://doi.org/10.1016/j.measurement.2016.02.037

Rostamian, F., & Etesami, N. (2018). Pool boiling characteristics of silica/water nanofluid and variation of heater surface roughness in domain of time. *International Communications in Heat and Mass Transfer*, *95*, 98–105. https://doi.org/https://doi.org/10.1016/j.icheatmasstransfer.2018.04.003

Rudi, A., Chiusano, G., & Verri, A. (2012). Adaptive Optimization for Cross Validation (pp. 435–440).

Salehi, H., Zeinali-Heris, S., Esfandyari, M., & Koolivand, M. (2013). Nero-fuzzy modeling of the convection heat transfer coefficient for the nanofluid. *Heat and Mass Transfer/Waerme- Und Stoffuebertragung*, *49*(4), 575–583. https://doi.org/10.1007/s00231-012-1104-9

Sarafraz, M. M., & Hormozi, F. (2016). Experimental investigation on the pool boiling heat transfer to aqueous multi-walled carbon nanotube nanofluids on the micro-finned surfaces. *International Journal of Thermal Sciences*, *100*, 255–266. https://doi.org/10.1016/j.ijthermalsci.2015.10.006

Sasaki, S., & Ashiwake, N. (2002). Enhancement of natural convection heat transfer from an inclined heated plate using rectangular grids. *Heat Transfer - Asian Research*, *31*(5), 408–419. https://doi.org/10.1002/htj.10043

Sathyamurthi, V., Ahn, H.-S., Banerjee, D., & Lau, S. C. (2009). Subcooled Pool Boiling Experiments on Horizontal Heaters Coated With Carbon Nanotubes. *Journal of Heat Transfer*, *131*(7), 071501. https://doi.org/10.1115/1.3000595

Saylor, J. R. (1989). *An experimental study of the size effect in pool boiling CHF on square surfaces*. University of Minnesota, Minneapolis.

Schenker, B., & Agarwal, M. (1996). Cross-validated structure selection for neural networks. *Computers & Chemical Engineering*, *20*(2), 175–186. https://doi.org/https://doi.org/10.1016/0098-1354(95)00013-R

Seo, G. H., Jeun, G., & Kim, S. J. (2015). Pool boiling heat transfer characteristics of

zircaloy and SiC claddings in deionized water at low pressure. *Experimental Thermal and Fluid Science*, *64*, 42–53. https://doi.org/https://doi.org/10.1016/j.expthermflusci.2015.01.017
Seo, G. H., Jeun, G., & Kim, S. J. (2016). Enhanced pool boiling critical heat flux with a FeCrAl layer fabricated by DC sputtering. *International Journal of Heat and Mass Transfer*, *102*, 1293–1307. https://doi.org/https://doi.org/10.1016/j.ijheatmasstransfer.2016.06.077
Seo, H., Chu, J. H., Kwon, S. Y., & Bang, I. C. (2015). Pool boiling CHF of reduced graphene oxide, graphene, and SiC-coated surfaces under highly wettable FC-72. *International Journal of Heat and Mass Transfer*, *82*, 490–502. https://doi.org/10.1016/j.ijheatmasstransfer.2014.11.019
Seo, H., Lim, Y., Shin, H., & Bang, I. C. (2018). Effects of hole patterns on surface temperature distributions in pool boiling. *International Journal of Heat and Mass Transfer*, *120*, 587–596. https://doi.org/10.1016/j.ijheatmasstransfer.2017.12.066
Shi, B., Wang, Y. B., & Chen, K. (2015). Pool boiling heat transfer enhancement with copper nanowire arrays. *Applied Thermal Engineering*, *75*, 115–121. https://doi.org/10.1016/j.applthermaleng.2014.09.040
Shojaeian, M., & Koşar, A. (2015). Pool boiling and flow boiling on micro- and nanostructured surfaces. *Experimental Thermal and Fluid Science*, *63*, 45–73. https://doi.org/10.1016/j.expthermflusci.2014.12.016
Song, J., Romero, C. E., Yao, Z., & He, B. (2016). Improved artificial bee colony-based optimization of boiler combustion considering NOX emissions, heat rate and fly ash recycling for on-line applications. *Fuel*, *172*, 20–28. https://doi.org/https://doi.org/10.1016/j.fuel.2015.12.065
Specht, D. F. (1991). A general regression neural network. *IEEE Transactions on Neural Networks*, *2*(6), 568–576. https://doi.org/10.1109/72.97934
Staszel, C., & Yarin, A. L. (2018). Exponential vaporization fronts and critical heat flux in pool boiling. *International Communications in Heat and Mass Transfer*, *98*, 171–176. https://doi.org/https://doi.org/10.1016/j.icheatmasstransfer.2018.08.019
Tachibana, F., Akiyama, M., & Kawamura, H. (1967). Non-Hydrodynamic Aspects of Pool Boiling Burnout. *Journal of Nuclear Science and Technology*, *4*(3), 121–130. https://doi.org/10.1080/18811248.1967.9732708
TACHIBANA, F., AKIYAMA, M., & KAWAMURA, H. (1967). Non-Hydrodynamic Aspects of Pool Boiling Burnout. *Journal of Nuclear Science and Technology*, *4*(3), 121–130. https://doi.org/10.1080/18811248.1967.9732708
Ujereh, S., Fisher, T., & Mudawar, I. (2007). Effects of carbon nanotube arrays on nucleate pool boiling. *International Journal of Heat and Mass Transfer*, *50*(19–20), 4023–4038. https://doi.org/10.1016/j.ijheatmasstransfer.2007.01.030
Vassallo, P., Kumar, R., & D'Amico, S. (2004). Pool boiling heat transfer experiments in silica–water nano-fluids. *International Journal of Heat and Mass Transfer*, *47*(2), 407–411. https://doi.org/https://doi.org/10.1016/S0017-9310(03)00361-2
Wang, K., Gong, S., Bai, B., & Ma, W. (2017). On the Relation between Nucleation Site Density and Critical Heat Flux of Pool Boiling. *Heat Transfer Engineering*, *0*(0), 1–9. https://doi.org/10.1080/01457632.2017.1369836
Wang, X. S., Wang, Z. B., & Chen, Q. Z. (2010). Research on Manufacturing Technology and Heat Transfer Characteristics of Sintered Porous Surface Tubes.

Advanced Materials Research, *97–101*, 1161–1165. https://doi.org/10.4028/www.scientific.net/AMR.97-101.1161

Watwe, A. A., Bar-Cohen, A., & McNeil, A. (1996). Combined pressure and subcooling effects on pool boiling from a PPGA chip package. In *InterSociety Conference on Thermal Phenomena in Electronic Systems, I-THERM V* (pp. 284–291). https://doi.org/10.1109/ITHERM.1996.534574

Wei, J. J., Guo, L. J., & Honda, H. (2005). Experimental study of boiling phenomena and heat transfer performances of FC-72 over micro-pin-finned silicon chips. *Heat and Mass Transfer/Waerme- Und Stoffuebertragung*, *41*(8), 744–755. https://doi.org/10.1007/s00231-005-0633-x

Wei, J. J., & Honda, H. (2003). Effects of fin geometry on boiling heat transfer from silicon chips with micro-pin-fins immersed in FC-72. *International Journal of Heat and Mass Transfer*, *46*(21), 4059–4070. https://doi.org/10.1016/S0017-9310(03)00226-6

Wei, J., & Xue, Y. (2011). Enhanced Boiling Heat Transfer from Micro-Pin-Finned Silicon Chips. In A. Belmiloudi (Ed.), *Heat Transfer*. Rijeka: InTech. https://doi.org/10.5772/14466

Xiao, Y., Wang, H., & Xu, W. (2015). Parameter Selection of Gaussian Kernel for One-Class SVM. *IEEE Transactions on Cybernetics*, *45*(5), 941–953. https://doi.org/10.1109/TCYB.2014.2340433

Xue, Y. F., Zhao, J. F., Wei, J. J., Zhang, Y. H., & Qi, B. J. (2013a). Experimental study of nucleate pool boiling of FC-72 on micro-pin-finned surface under microgravity. *International Journal of Heat and Mass Transfer*, *63*, 425–433. https://doi.org/10.1016/j.ijheatmasstransfer.2013.03.083

Xue, Y. F., Zhao, J. F., Wei, J. J., Zhang, Y. H., & Qi, B. J. (2013b). Experimental study of nucleate pool boiling of FC-72 on micro-pin-finned surface under microgravity. *International Journal of Heat and Mass Transfer*, *63*, 425–433. https://doi.org/10.1016/j.ijheatmasstransfer.2013.03.083

Yadav, A. K., Malik, H., & Chandel, S. S. (2014). Selection of most relevant input parameters using WEKA for artificial neural network based solar radiation prediction models. *Renewable and Sustainable Energy Reviews*, *31*, 509–519. https://doi.org/https://doi.org/10.1016/j.rser.2013.12.008

Yang, H., & Banerjee, D. (2016). Exploring the “nano-fin effect” in pool boiling enhancement using temperature nano-sensor arrays. In *First Thermal and Fluids Engineering Summer Conference* (pp. 1811–1821). https://doi.org/10.1615/TFESC1.mph.012953

Yang, S. H., Baek, W.-P., & Chang, S. H. (1997). Pool-boiling critical heat flux of water on small plates: Effects of surface orientation and size. *International Communications in Heat and Mass Transfer*, *24*(8), 1093–1102. https://doi.org/https://doi.org/10.1016/S0735-1933(97)00103-6

Yao, Z., Lu, Y. W., & Kandlikar, S. G. (2011). Effects of nanowire height on pool boiling performance of water on silicon chips. *International Journal of Thermal Sciences*, *50*(11), 2084–2090. https://doi.org/10.1016/j.ijthermalsci.2011.06.009

You, S. M., Kim, J. H., & Kim, K. H. (2003). Effect of nanoparticles on critical heat flux of water in pool boiling heat transfer. *Applied Physics Letters*, *83*(16), 3374–3376. https://doi.org/10.1063/1.1619206

Yu, C. K., & Lu, D. C. (2007). Pool boiling heat transfer on horizontal rectangular fin array in saturated FC-72. *International Journal of Heat and Mass Transfer*, *50*(17–18), 3624–3637. https://doi.org/10.1016/j.ijheatmasstransfer.2007.02.003

Yu, D. I., Kwak, H. J., Noh, H., Park, H. S., Fezzaa, K., & Kim, M. H. (2018). Synchrotron x-ray imaging visualization study of capillary-induced flow and critical heat flux on surfaces with engineered micropillars. *Science Advances*, *4*(2), 37–42. https://doi.org/10.1126/sciadv.1701571

Yu, X., Woodcock, C., Wang, Y., Plawsky, J., & Peles, Y. (2017). Enhanced Subcooled Flow Boiling Heat Transfer in Microchannel With Piranha Pin Fin. *Journal of Heat Transfer*, *139*(11), 112402. https://doi.org/10.1115/1.4036683

Yuan, J., Liu, X., Akbulut, O., Hu, J., Suib, S. L., Kong, J., & Stellacci, F. (2008). Superwetting nanowire membranes for selective absorption. *Nature Nanotechnology*, *3*(6), 332–336. https://doi.org/10.1038/nnano.2008.136

Yuan, M., Wei, J., Xue, Y., & Fang, J. (2009a). Subcooled flow boiling heat transfer of FC-72 from silicon chips fabricated with micro-pin-fins. *International Journal of Thermal Sciences*, *48*(7), 1416–1422. https://doi.org/10.1016/j.ijthermalsci.2008.11.018

Yuan, M., Wei, J., Xue, Y., & Fang, J. (2009b). Subcooled flow boiling heat transfer of FC-72 from silicon chips fabricated with micro-pin-fins. *International Journal of Thermal Sciences*, *48*(7), 1416–1422. https://doi.org/10.1016/j.ijthermalsci.2008.11.018

Zhang, Y., Zhou, J., Zhou, W., Qi, B., & Wei, J. (2018a). CHF correlation of boiling in FC-72 with micro-pin-fins for electronics cooling. *Applied Thermal Engineering*, *138*, 494–500. https://doi.org/10.1016/j.applthermaleng.2018.04.053

Zhang, Y., Zhou, J., Zhou, W., Qi, B., & Wei, J. (2018b). CHF correlation of boiling in FC-72 with micro-pin-fins for electronics cooling. *Applied Thermal Engineering*, *138*, 494–500. https://doi.org/10.1016/j.applthermaleng.2018.04.053

Zhao, J., Wang, T., Yatskar, M., Ordonez, V., & Chang, K.-W. (2017). Men Also Like Shopping: Reducing Gender Bias Amplification using Corpus-level Constraints. In *Proceedings of the 2017 Conference on Empirical Methods in Natural Language Processing* (pp. 2979–2989). https://doi.org/10.18653/v1/D17-1323

Zou, A., & Maroo, S. C. (2013). Critical height of micro/nano structures for pool boiling heat transfer enhancement. *Applied Physics Letters*, *103*(22). https://doi.org/10.1063/1.4833543

Zou, A., Singh, D. P., & Maroo, S. C. (2016). Early Evaporation of Microlayer for Boiling Heat Transfer Enhancement. *Langmuir*, *32*(42), 10808–10814. https://doi.org/10.1021/acs.langmuir.6b02642